# IR Near-field Nanoscopy and Spectroscopy of Cells and Soft Matter

**Dissertation**

zur Erlangung des Grades eines
Doktors der Naturwissenschaften (Dr. rer. nat.)

am Fachbereich Physik
der Freien Universität Berlin

vorgelegt von

Katerina Kanevche

Berlin, den 10. November 2021

**ERSTGUTACHTER**

Prof. Dr. Joachim HEBERLE

Freie Universität Berlin

Fachbereich Physik

Experimentelle Molekulare Biophysik

**ZWEITGUTACHTER**

Prof. Dr. Kiril BOLOTIN

Freie Universität Berlin

Fachbereich Physik

Nanoscale Transport and Optoelectronics

Tag der Disputation: 21.03.2022

# Publications related to the work presented in this thesis

Kopyshev, A., **Kanevche**, **K.**, Lomadze N., Pfitzner E., Loebner, S., Patil, R., Genzer, J., Heberle, J. and Santer, S. ”Light-Induced Structuring of Photosensitive Polymer Brushes” *ACS Applied Polymer Materials*, 1, 3017-3026, 2019.

**Kanevche**, **K.**, Burr, D., Hass, P., Nuernberg, D., Elsaesser, A. and Heberle, J. ”Infrared Nanoscopy and Tomography of Intracellular Structures” *Nature Communications Biology*, 2021, *accepted* (preprint available at Research Square DOI:10.21203/rs.3.rs-753486/v1).

# Manuscripts in preparation

Fernandes, R., Ernst, N., Saleh, N., **Kanevche, K.**, Berlepsch, H., Hosogi, N., Heberle, J., Weber, M., Böttcher, C., Koksch, B. ”Novel pH-triggered self-assembly of a dye-peptide conjugate”.

Burr, D., **Kanevche**, **K.**, Stryhanyuk, H., Adrian L., Kümmel, S., Musat, N., Heberle, J., Elsaesser, A., Perfumo, A. ”Quantification of single-cell translational activity and protein synthesis using stable isotope probing visualized with nanospectroscopy”.

# ABSTRACT

Probing the interaction of infrared (IR) light with matter is, in essence, probing molecular vibrations of chemical bonds. Almost all biologically relevant molecules respond to this range of electromagnetic radiation. Traditional IR microscopes and spectrometers operate in the optical far-field and are hence limited in resolution by diffraction. One approach to overcome this barrier is to capture light-matter interactions in the optical near field via raster scanning the sample with a sharp probe, which is the core idea of scattering-type scanning near-field optical microscopy (sSNOM).

In this work, sSNOM and nano Fourier transform IR (nanoFTIR) were applied to samples with increasing complexity, starting with cellular membranes, followed by stimuli responsive peptides and polymer brush surfaces, concluding with investigation of cells.

The morphology and secondary structure of large-scale aggregates, resulting from self-assembly of a well-defined peptide sequence were determined. Variation of the pH and the hydrophobicity by single amino acid residue exchanges influenced the aggregate's level of ordering while maintaining an $\alpha$-helical secondary structure. Another example of external stimuli inducing morphological changes is surface patterning of photosensitive polymer brushes formed upon UV interference. NanoFTIR was employed to infer that the pattern formation depends on the degree of disassociation of the polymer brushes in solution. Stable isotope probing in combination with nanoFTIR spectroscopy was applied to investigate the metabolic activity of bacteria. Introducing $^{13}$C-labeled glucose, it was possible to deduce the carbon consumption of single cells from the amide I and amide II band position. The measured IR response of whole cells is limited to approximately 100 nm below the surface. To investigate the cellular substructure, cross-sections of *E. coli* and *C. reinhardtii* using microtome sectioning were used. Additionally, sSNOM tomography is presented, where sequential *C. reinhardtii* cross-sections were used to reconstruct the three dimensional structure.

In conclusion, this work highlights the necessity to address morphology, molecular structure and chemical composition of soft matter and biomaterials on a nm-level and reflects on the power of IR nanoscopy and sSNOM to retrieve images under ambient conditions in the absence of any labeling.

# ZUSAMMENFASSUNG

Die Untersuchung der Wechselwirkung von Infrarotlicht (IR) mit Materie beschäftigt sich im Wesentlichen mit der Untersuchung von Molekülschwingungen chemischer Bindungen. Fast alle biologisch relevanten Moleküle reagieren auf elektromagnetische Strahlung im IR-Bereich. Traditionelle IR Mikroskope und Spektrometer arbeiten im optischen Fernfeld und sind daher in der Auflösung durch Beugung begrenzt. Ein Ansatz zur Überwindung dieser Barriere besteht darin, Licht-Materie Wechselwirkungen im optischen Nahfeld durch Abrastern der Probe mit einer scharfen Spitze zu erfassen, welches die Kernidee der streuungsbasierten optischen Rasternahfeld-Mikroskopie ist (sSNOM, engl. scattering-type scanning near-field optical microscopy). In dieser Arbeit wurden sSNOM und nano-Fourier Transform IR (nanoFTIR) Spektroskopie auf Proben mit zunehmender Komplexität angewendet, beginnend mit Zellmembranen, gefolgt von anregungsresponsiven Peptiden und Polymerbürstenoberflächen, bis hin zur Untersuchung von Zellen.

Die Morphologie und Sekundärstruktur von großflächigen Aggregaten, die durch Selbstorganisation von definierten Peptidsequenzen resultieren, wurden bestimmt. Die Variation des pH-Werts und der Hydrophobie durch den Austausch einzelner Aminosäurereste beeinflusste den Ordnungsgrad des Aggregats, wobei eine $\alpha$ helikale Sekundärstruktur beibehalten wurde. Ein weiteres Beispiel für eine externe Anregung, die Veränderungen in der Morphologie induziert, ist die Oberflächenstrukturierung von lichtempfindlichen Polymerbürsten, die unter UV-Interferenz gebildet werden. Mithilfe von nanoFTIR wurde festgestellt, dass die Musterbildung vom Dissoziationsgrad der Polymerbürsten in einer Lösung abhängt. Schließlich wurde Isotopenmarkierung in Kombination mit nanoFTIR-Spektroskopie verwendet, um die Stoffwechselaktivität von Bakterien zu untersuchen. Durch die Einführung von $^{13}$C-markierter Glucose war es möglich, den Kohlenstoffverbrauch einzelner Zellen aus der Position der Amid I- und Amid II-Bande abzuleiten. Die gemessenen IR-Spektren ganzer Zellen ergaben sich dabei aus einer Eindringtiefe von ca. 100 nm. Zur Untersuchung der zellulären Unterstruktur wurden Mikrotomquerschnitte von *E. coli* und *C. reinhardtii* verwendet. Darüber hinaus wird die sSNOM-Tomographie vorgestellt, bei der sequentielle *C. reinhardtii* Querschnitte verwendet wurden, um die dreidimensionale Struktur zu rekonstruieren.

Zusammenfassend unterstreicht diese Arbeit die Notwendigkeit, Morphologie, molekulare Struktur und chemische Zusammensetzung von Biomaterialien auf der nm-Ebene zu untersuchen und reflektiert die Leistungsfähigkeit von IR-Nanoskopie und sSNOM.

# Contents

# List of Figures

# List of Tables

# List of Abbreviations

| | |
|---|---|
| **AFM** | atomic force microscopy |
| **ATR** | attenuated total reflection |
| **Au** | gold (*Latin: aurum*) |
| **bR** | bacteriorhodopsin |
| **CARS** | coherent anti-Stokes Raman scattering |
| **cryo-EM** | cryogenic electron microscope |
| **Cy5** | cyanine dye |
| **DFG** | difference frequency generation |
| **DNA** | deoxyribonucleic acid |
| **E.coli** | Escherichia coli |
| **EM** | electron microscope |
| **Er** | erbium |
| **FDTD** | finite-difference time-domain |
| **FDM** | finite dipole model |
| **FT** | Fourier transform |
| **FFT** | fast Fourier transform |
| **FTIR** | Fourier-transform infrared |
| **GaSe** | Galium(II) selenide |
| **HeNe** | helium neon |
| **IR** | infrared |
| **LSP** | localized surface plasmon |
| **MCT** | mercury cadmium telluride |
| **nano-FTIR** | nano Fourier-transform infrared |

| | |
|---|---|
| **NSOM** | near-field scanning optical microscopy |
| **OPD** | optical path difference |
| **PC** | principle component |
| **PCA** | principle component analysis |
| **PE** | polyelectrolyte |
| **PI** | proportional-integral |
| **PM** | purple membrane |
| **PMAA** | poly(methacrylic acid) |
| **PS** | photosystem |
| **PSPMK** | poly(3-sulfopropyl methacrylate/potassium salt) |
| **PVD** | physical vapor deposition |
| **QCL** | quantum cascade laser |
| **Si** | silicon |
| **SIP** | stable isotope labeling |
| **SPM** | scanning probe microscopy |
| **SPP** | surface plasmon polaritons |
| **SNOM** | scanning optical microscopy |
| **sSNOM** | scattering-type scanning optical microscopy |
| **SRG** | surface relief grating |
| **SRS** | stimulated Raman scattering |
| **STAP** | stimuli-triggered aggregating peptide |
| **STED** | stimulated emission depletion |
| **STM** | scanning tunneling microscopy |
| **SVD** | single value decomposition |
| **TS Au** | template stripped Au |
| **TERS** | tip-enhanced Raman spectroscopy |
| **TIR** | total internal reflection |
| **TMAB** | trimethylammonium bromide |

| | |
|---|---|
| **TRIS** | 2-amino-2-hydroxymethyl-propane-1,3-diol |
| **ZnSe** | zinc selenide |

# Chapter 1

# Introduction

One of the first records showing that living organisms are made up of smaller units, invisible to the naked eye, is Robert Hooke's *Micrographia* [1], dating back to 1655. The cellular structure of various objects, cataloged in this work, was observed with the aid of an optical microscope, following the design of compound microscopes [2] first appearing in Europe in the 1620s. With improving lens manufacturing techniques and microscope design, images with increasing level of detail and resolution could be recorded, which ultimately lead to countless discoveries in natural sciences.

## 1.1 Beyond the diffraction limit

There is a fundamental limitation to the achievable resolution of an imaging system due to diffraction. The ability of an instrument to resolve small objects is closely related to the phenomenon of light diffraction and poses a fundamental limit to the spatial resolution given by Ernst Abbe's formulation [3]

$$d = \frac{\lambda}{2n\sin\theta}, \tag{1.1}$$

where $\lambda$ is the wavelength of the source light, n the refractive index of the imaging system (for eg. objective) and $\Theta$ is the half-angle spanned by an objective (Figure 1.1). Due to diffraction the imaging system can't focus the light to a single point but is rather distributed to an area, the Airy disc [4] with dimension d, which defines the smallest resolvable lateral distance.

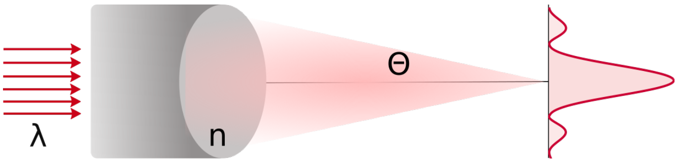

FIGURE 1.1: Diffraction limit sketched in one dimension of an imaging system (such as an objective) with reflective index n using a light source with wavelength $\lambda$. $\Theta$ denotes the half-angle spanned by the objective.

Perhaps the most obvious approach to record high resolution images is to use short-wavelength radiation as a light source. Indeed, this idea led to a great success with the development of the electron microscope (EM) [5], using accelerated electrons with a wavelength defined by the de Broglie Equation [6]. Meanwhile, protein structure could be resolved with atom-resolution using cryo-EM [7]. Despite the excellent resolving power, electron microscopy requires elaborate sample preparation and, due to the high source energies involved, it is a destructive technique.

Noteworthy efforts were put towards achieving resolution beyond the diffraction limitation in light microscopy as outlined in *"The 2015 super-resolution microscopy roadmap"* [8]. Super-resolution microscopy techniques operating in the optical far-field are usually utilizing fluorescent labels in order to visualize the targeted molecules. Stimulated emission depletion (STED) microscopy [9] provides resolution in the order of 30-80 nm [10], with a record resolution of 6 nm [11]. While STED and related techniques deliver chemical images of biological specimens with resolution beyond the diffraction limit, they rely on labeling to gain chemical contrast.

Vibrational techniques, such as IR and Raman spectroscopy, are sensitive to the specimen's chemical composition by directly probing molecular vibrations [12]. Advanced Raman microscopy techniques involving nonlinear optics effects such as coherent anti-Stokes Raman scattering (CARS) and stimulated Raman scattering (SRS) have been applied to spectroscopic imaging [13], thus overcoming the limitations due to weak scattering cross-section typical for Raman scattering [14]. Namely, lateral resolution beyond the diffraction limit, in the order of 100 nm, has been reported [15]. Spectroscopy and imaging in the mid-IR range covering the fingerprint and functional group region for multitude of molecules [16], thus of particular interest in biophysics, are severely limited in resolution by diffraction. IR microscopy and spectroscopy have experienced boost in lateral resolution, sensitivity and speed by implementing quantum cascade laser (QCL) [17] as a light source. Application to tissue imaging and diagnostics [18, 19] coupled with machine learning algorithms have been reported [20], however with spatial resolution still within the diffraction limitations.

Shifting from observing light-matter interaction in the far-field to the optical near-field lies at the heart of vibrational diffraction-unlimited techniques [21]. A common approach to generate and probe the near-field is using a sharp probe, typically used in scanning probe microscopy (SPM) [22]. This approach involves a light source focused on the sharp tip, which acts as a nanoantenna to confine and localize the incident radiation [23], or the probe is plasmonically excited [24]. By bringing a sample in the vicinity of the illuminated probe, tip-sample interaction in the optical near field takes place, manifested by processes such as inelastic and elastic light scattering or Raman scattering [25]. The back-scattered field contains information on the sample's optical and chemical properties. The lateral resolution depends primarily on the tip's size instead of the wavelength. In tip-enhanced Raman spectroscopy (TERS), incident light excites localized surface plasmons at the apex of a scanning tunneling microscope (STM) or metal-coated atomic force microscope (AFM) tip [26, 27, 28, 29]. To date, TERS achieved the highest spatial resolution in the field of vibrational nanoscopy of $< 2$ Å [30]. It has been proposed that the reason for the TERS resolution exceeding the tip's size is coupling between the excited plasmon on the tip's apex and the molecular vibrations [31]. Another major contributor to the high resolving power is operation in cryogenic conditions, which minimizes sample drift and maximizes stability of the specially designed probes. Considering biologically relevant samples at room temperature with the intention to probe proteins, lipids or DNA, which intrinsically have low scattering Raman cross section, TERS becomes less applicable [32]. A complementary technique, operating in the IR electromagnetic range, is scanning near-field optical microscopy (SNOM). The initial design utilizing a sub-wavelength aperture provided spatial resolution below the diffraction limit [33, 34], however with limited success in the IR region. Superior resolving power was achieved using aperture-less scattering-type scanning near field optical microscope (sSNOM) [35, 36]. Description of the nature of tip-sample interaction relates the sample's optical properties to the scattered near-field phase and amplitude [37, 38]. Typical spatial resolution of the near-field phase is in the order of 20-30 nm, down to 5 nm utilizing ultra-sharp tips [39]. This near-field technique has been expanded to performing nano-resolved Fourier-transform infrared spectroscopy (nano-FTIR) by implementing broadband lasers [40, 41] or by coupling synchrotron radiation [42, 43]. In the past two decades, this technique has experienced tremendous advance, spanning over multitude of fields such as biophysics, environmental science, 2D-materials and plasmonics [44].

## 1.2 Scope of the thesis

Throughout this work near-field microscopy and spectroscopy in the mid-IR will be applied on diverse systems that require morphological identification with chemical specificity. To establish and confirm various experimentation conditions of a custom-made sSNOM setup, the cell membrane of *Halobacterium* containing the protein *Bacteriorhodopsin* (bR) was used. In a step-wise manner, systems with increasing chemical and morphological complexity were investigated, as outlined in the PhD thesis map. Aggregation, self-assembly and secondary structure of artificially designed peptides triggered by external stimuli such as pH and temperature was simultaneously studied by AFM, sSNOM and nanoFTIR.

The formation of large scale surface patterns in light-sensitive polymer brushes under illumination with interference pattern were examined. Determination of the local chemical composition of the brush prior to and following the pattern formation was carried out using nanoFTIR spectroscopy.

Monitoring bio-chemical processes on the single level cell requires the spatial resolution and the sensitivity to molecular vibrations. NanoFTIR spectroscopy was further employed in investigating the metabolic activity of single bacterial cells by probing the cell's protein absorption features.

Due to the limited penetration depth of the near-field techniques used here, cellular sectioning was implemented to gain insights into the internal structure of cells. Thus, the full complexity of the sub-cellular features of bacterial and algal cells was studied using imaging and spectroscopy with high lateral resolution. Finally, an effort was put to resolve three-dimensional sub-cellular structure where the contrast originates from local IR absorption by performing sSNOM tomography.

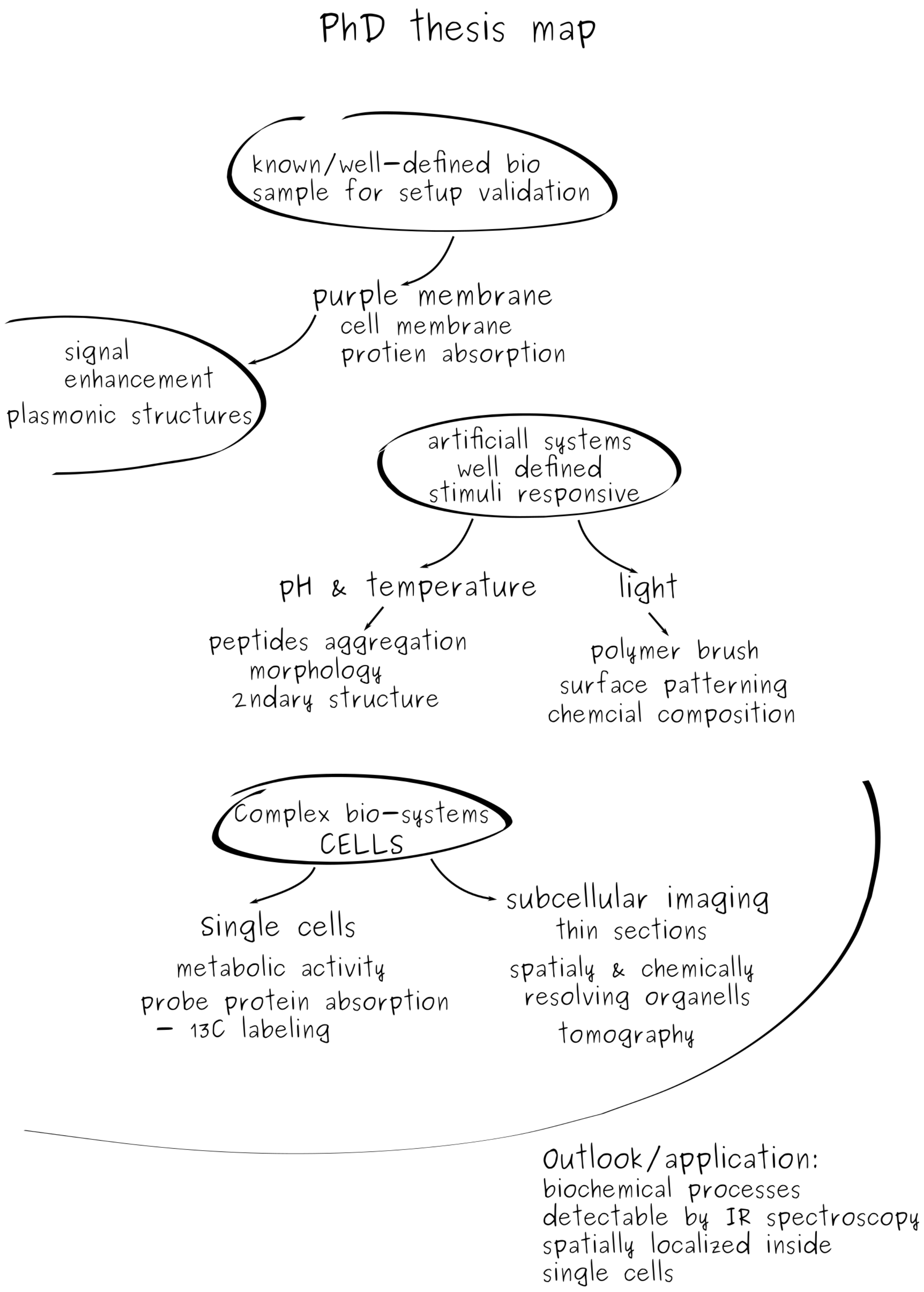
PhD thesis map
known/well-defined bio sample for setup validation
purple membrane
cell membrane
protien absorption
signal enhancement
plasmonic structures
artificiall systems
well defined
stimuli responsive
pH & temperature
peptides aggregation
morphology
2ndary structure
light
polymer brush
surface patterning
chemcial composition
Complex bio-systems
CELLS
Single cells
metabolic activity
probe protein absorption
– 13C labeling
subcellular imaging
thin sections
spatialy & chemically
resolving organells
tomography
Outlook/application:
biochemical processes
detectable by IR spectroscopy
spatially localized inside
single cells

# Chapter 2

# Theory and Techniques

## 2.1 Atomic Force Microscopy

Atomic force microscopy (AFM) belongs to the family of scanning probe techniques, pioneered by G. Binning and H. Rohrer with the development of scanning tunneling microscopy (STM) [45] which was awarded with the Nobel prize in Physics in 1986. This technology based on a probe that scans the surface, rather than on a conventional optical microscope, is able to achieve atomistic spatial resolution [46], thus far below the diffraction limit. The AFM, based on atomic interactions between a sharp tip and the surface, was developed soon after [47, 48], with atomic lateral resolution [49]. In contrast to STM, an AFM does not require conductive surfaces which extended its applicability to biological samples, thus becoming an established method used in a plethora of research in biophysics [50].

### 2.1.1 Working Principle

Essentially, a sharp tip positioned on an elastic cantilever is scanned across the surface. As the cantilever is approached to the surface, forces between the tip and the surface cause mechanical deformation of the cantilever, such as lateral and vertical deflection (Figure 2.1) [51]. The interaction between the probe and the sample can be modeled by the Lennard-Jones potential [52], describing the interaction of two neutral atoms

$$V_{Lennard-Jones}(r) = 4\epsilon\left[\left(\frac{\sigma}{r}\right)^{12} - \left(\frac{\sigma}{r}\right)^{6}\right], \qquad (2.1)$$

where $\epsilon$ denotes depth of the potential well, $r$ the distance between the two atoms and $\sigma$ is the equilibrium distance. The term $\propto r^{-12}$ describes short-range repulsive interactions due to Pauli exclusion principle, while the term $\propto r^{-6}$ describes long-range attractive van der Waals interactions [53]. Additionally, depending on factors such as the tip material and shape, sample surface properties or imaging medium, the nature of the forces between the atoms of the probe and the sample can be electrostatic repulsive and attractive [54], covalent [55], magnetic [56] or solvation forces [57].

The deflection experienced by the cantilever is traced with a laser. Initially, the laser is guided to a position on the cantilever with highest reflection and the back-reflection is centered on a photodiode.

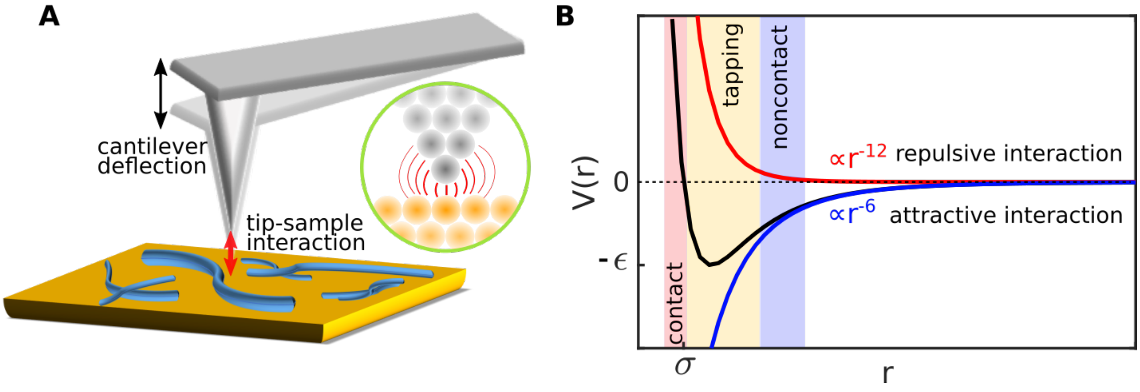

Figure 2.1: AFM working principle
**A** Schematic of atomic interaction between an AFM probe and sample resulting in cantilever deflection. **B** Lennard-Jones potential, given by Equation 2.1, models the interaction between two neutral atoms. In non-contact imaging mode, attractive long-range van der Waals interaction between the tip and the sample is dominant. In contact mode there is repulsive short range interaction between the tip and the surface. In tapping mode (also known as intermittent contact mode) the tip oscillates between non-contact and contact mode. Non-contact mode operates in the attractive interaction regime.

Any change of the position of the cantilever results in shifts of the reflected laser beam and the spot where the back-reflected light hits the photodiode. Piezo xyz-stage moves the sample or the cantilever with picometer precision. Factors limiting the spatial resolution of this technique include the size of the tip's apex, the precision of piezo elements, mechanical stability of sample stage and cantilever holder and thermal fluctuations of the sample and the cantilever [58]. There are several approaches to image recording, with the most commonly used imaging modes being contact mode, intermittent contact mode, also known as tapping mode, and non-contact mode [59].

**Contact mode** In contact mode the AFM tip is in constant contact with the surface and the cantilever deflects in response to repulsive forces dominating the tip-sample interaction (Figure 2.1 b). Image formation can be carried out by cantilever deflection detection while the cantilever height is kept constant. Another approach is employing dynamic cantilever height adjustment while scanning, i.e following the surface topography while keeping the cantilever deflection constant. In this scenario the applied constant force, translating to constant deflection, is the value defined as setpoint in a proportional-integral (PI) feedback loop. Any difference between the setpoint and the actual measured value is compensated according to the two parameters of the PI loop and thus move the cantilever height in response to the surface topography.

**Tapping mode** In tapping mode [60] the AFM tip oscillates close to the surface and establishes contact only in the regime of repulsive force, at the lowest oscillation position, with frequency close to the resonant frequency of the cantilever-tip system. Typical frequency used for imaging in air is in the order of few hundred kHz and can be estimated from the cantilever's spring constant and mass. Image formation relies on a PI feedback loop with the oscillation amplitude defined as a setpoint, instead the cantilever deflection as used in contact mode. In addition to the topography, tapping mode imaging provides amplitude and phase images. The amplitude image is formed by recording the cantilever deflection, thus contains similar information to the topography. The phase image originates from the phase shift between the phase with which the cantilever is driven to oscillate and the phase that is measured while the cantilever while scanning the surface. The contrast of the phase image can be attributed to material properties of the surface such as elasticity and stiffness.

**Non-contact mode** In this mode the cantilever is driven to oscillate close to the surface with amplitudes in the range of few nanometers to picometes, in the attractive interaction regime (Figure 2.1 b) [61]. In contrast to tapping mode, in non-contact mode the tip does not get in contact to the surface. The surface topography is obtained by either monitoring the changes in the oscillation amplitude or the frequency resulting from tip-sample interaction.

### 2.1.2 Beyond topography imaging

Since the invention of the AFM many further developments have been reported, such as extending the imaging medium to liquid [62], thus enabling imaging of biological systems in their native environment, increasing its imaging speed to monitor molecular dynamics [63, 64], elasticity and adhesion imaging via force mapping [65], to mention just a few. One step further is coupling the AFM technology with super resolution fluorescence techniques to access further aspects of the nano-realm. Using stimulated emission depletion STED-AFM configurations, fluorescence images with resolution below 100 nm [66] have been reported. However, the contrast and the chemical specificity in this approach relies on using labels and fluorescent dyes. In the following, scanning near-field optical microscopy, a technique exploiting the high spatial resolution of AFM coupled with the chemical sensitivity of IR microscopy, will be elaborated.

## 2.2 Scanning Near-Field Optical Microscope

E.H.Synge in his article from 1928 in the London, Edinburgh, and Dublin philosophical magazine and journal of science [67] proposed an approach to overcome the diffraction limit in optical microscopy by introducing a micrometer sized aperture at a submicron distance from a flat specimen. Experimental realization of subwavelength resolution using an aperture was reported in the microwave spectral region [68]. This conceptually novel imaging approach was implemented using visible radiation in the early 1980s thus marking the beginning of near-field optical microscopy. D. Pohl from the IBM research laboratory in Zurich [69, 33] and A. Lewis from Cornell University USA [34] developed this technique independent form each other, hence in literature both abbreviations SNOM standing for scanning near-field optical microscopy and NSOM for near-field scanning optical microscopy are present. Throughout this text, SNOM will be used. Today there are multitude of specialized SNOM systems [25], the core principle for all of them being operation in the optical near-field.

### 2.2.1 The optical near-field

According to Ernst Abbe, the diffraction limit defines the smallest resolvable structure to be dependent on the illumination wavelength and the numerical aperture of the imaging system given by Equation 1.1. Hence, the size of the smallest resolvable structure is limited by the incident wavelength which for infrared microscopy is in the order of micrometers. Rewriting the diffraction relation 1.1 in terms of the wave vector $k = \frac{2\pi}{\lambda}$ and the momentum $p = \frac{kh}{2\pi}$ it can be deduced that small resolving distance requires large wave vector and large momentum. Freely propagating electromagnetic field is given by the time-dependent wave equation derived form Maxwell's equations [70] as

$$\mathbf{E}(\mathbf{r}, t) = E_0 e^{-i(\mathbf{k}\cdot\mathbf{r})-\omega t} \quad \text{for} \quad \mathbf{k} = (k_x, k_y, k_z), \tag{2.2}$$

where $\mathbf{k}$ denotes the field's wave vector with components $k_x$, $k_y$ and $k_z$, $\omega$ is the angular frequency, $t$ denotes the time and $\mathbf{r} = (x, y, z)$ represents the spatial coordinates. Considering $k_x, k_y, k_x \in \mathbb{R}$ the following relations hold for $\mathbf{k}$

$$\mathbf{k^2} = k_x^2 + k_y^2 + k_z^2 \quad \text{and} \quad |k_x|, |k_y|, |k_z| < |\mathbf{k}|. \tag{2.3}$$

This implies that the propagating far-field has real wave vector and real momentum components in all directions. Following the concept of exploiting components of the electromagnetic radiation with large momentum and large wave vector for the light's spatial confinement smaller than $\lambda/2$, at least one of $k_x$, $k_y$ or $k_z$ has to become complex. This can be expressed as [71]

$$\mathbf{E}(\mathbf{r}, t) = E_0 e^{-i(k_x x + k_y y + k_z z - \omega t)} = E_0 e^{-i(k_x x + k_y y - \omega t)} e^{-\frac{z}{d}}, \tag{2.4}$$

for decay length $d = -\frac{i}{k_z}$. The term $E_0 e^{-\frac{z}{d}}$ can be interpreted as part of the field that decays exponentially away form the source in z-direction. Moreover, the imaginary nature of the term further implies that even tough existent, this part of the field is not propagating and is confined to sub-wavelength distance from the source, i.e in its near-field. Utilizing this range of the field to gain diffraction-unlimited resolution demands a way to generate the near-field and a method to detect it. The familiar architecture of optical or IR microscopes is not suitable for that task since the observation and detection is performed in the radiating far field. The initial proposal of E. H. Synge predicted the near-field formation at an aperture with dimension smaller than the incident wavelength (Figure 2.2 a). Meanwhile, a variety of approaches have been introduced [71] including, but not limited to, evanescent field generation at an interface due to total internal reflection (TIR) (Figure 2.2 b) [72], fiber probe with subwavelength aperture (Figure 2.2 c) [33, 34], an aperture-less probe with subwavelength tip diameter (Figure 2.2 d) [73] or gratings with subwavelength periodicity (Figure 2.2 e) [74].

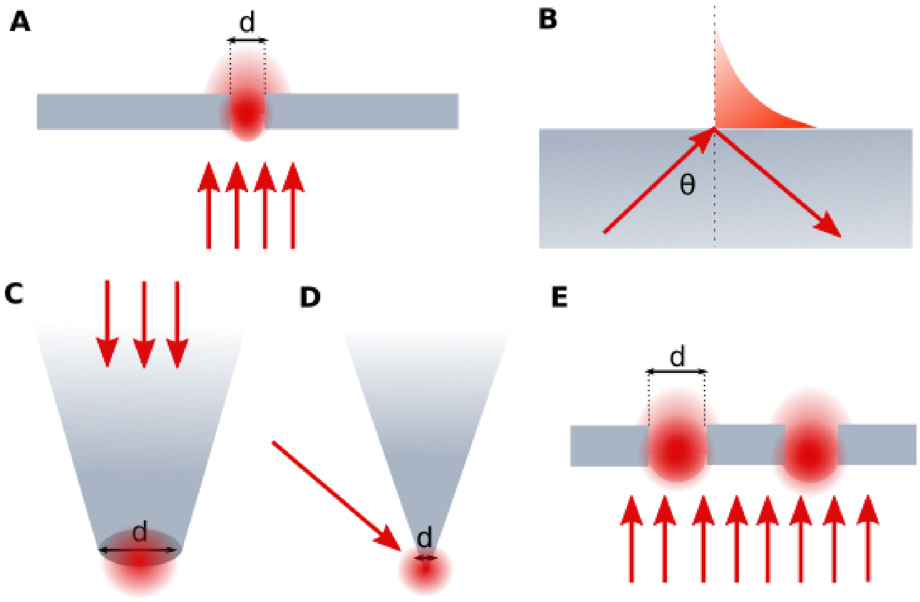

FIGURE 2.2: Near-field generation
**A** Incident light on an aperture with $d < \lambda$ yields near-field decaying with distance from the aperture. **B** Evanescent field generation at an interface upon total internal reflection. **C** Fiber probe with an aperture through which incident light is focused, such that $d < \lambda$ - design implemented in aperture-SNOM. **D** Incident light focused on an aperture-less probe with size $d < \lambda$ yielding near-field at the tip's apex, typical for scattering-type SNOM design. **E** Near-field generated at gratings with sub-wavelength periodicity.

### 2.2.2 Aperture SNOM

Perhaps the most intuitive way to grasp the concept of near-field imaging is thinking of a stethoscope and how it is possible to measure the heart beat with frequency of few Hz, typical for acoustic waves, while being able to localize the heart's position within some centimeters. Two aspects of this example are key for measuring beyond the diffraction limitation, namely the small aperture of the stethoscope and its vicinity to the sample. This flow of thought was presented as introduction in the very first report demonstrating the feasibility of aperture - SNOM [33]. Initially, the apertures were manufactured using sharp quartz tips with metallic coating to achieve opaqueness of the whole construct and an aperture was created as a result of plastic deformation by pressing against a hard surface [75]. Next generation SNOM probes, based on tapered optical fiber were introduced [76, 77], opened the gates to new aperture SNOM geometries. Typical setup design includes a sub-wavelength aperture, placed only a few nanometers form the surface, a mechanism to precisely approach and maintain such small distances, a light source illuminating the surface from the far-field or coupled to an optical fiber and a suitable detection scheme [78]. The far field illumination is necessary when the aperture is used for detection. Near-field illumination can be achieved when the light source is coupled to an optical fiber and at its aperture a near field is created. The interaction between the near-field and the sample is detected in the far-filed. Alternatively, an optical fiber can be used for both illumination and detection. The lateral resolution is given by the size of the aperture, however decreasing its diameter, manufacturing challenges aside, comes at the expense of the detectable signal. A model describing the transmission of electromagnetic waves through subwavelength aperture was developed by H. A Bethe in [79]. Namely, for an aperture the effective transmission cross-section is given by [25]

$$\sigma_{eff} = \frac{64}{27\pi}\left(\frac{2\pi r}{\lambda}\right)^4 r^2, \tag{2.5}$$

where $r$ is the aperture radius and $\lambda$ the wavelength of incident light. The transmitted power, in terms of the transmission coefficient and the energy of the incident radiation $\mathbf{E_i}$ is expressed as follows:

$$P(\sigma_{eff}, \mathbf{E}_i) = \sigma_{eff} \cdot \frac{1}{2} c\epsilon_0 \mathbf{E}_i^2. \tag{2.6}$$

From this description of the transmitted power, two drawbacks become evident. Firstly, gaining lateral resolution by using smaller aperture size is hindered by the drop of sixth order in transmitted power with decreasing the aperture radius $r$. The typical lateral resolution in aperture-SNOM experiments is 50-100 nm. A second challenge arises when applying SNOM in the infrared radiation range with wavelengths in the order of micrometers. $P(\sigma_{eff}, \mathbf{E}_i)$ is proportional to the inverse fourth power of the wavelength $\lambda$, thus limiting its applicability to IR and THz microscopy.

Additionally, challenges related to manufacturing small aperture SNOM probes with metallic coatings have been reported [35, 80]. These shortcomings can be circumvented by employing an apertureless probe, a technique known as scattering-type scanning near-field optical microscope (sSNOM).

### 2.2.3 Scattering SNOM

One of the first reports of aperture-less SNOM [81] demonstrates the possibility to perform microscopy with resolution comparable to AFM. Based on this patent [35], near-field images at wavelength $\lambda$=633 nm of a microscope cover slip surface features with size within 3 nm were shown. Already at this early stage the challenge of separating the rather weak scattering signal from the tip from the background scattering was recognized and tackled by jittering the tip and demodulating the signal at the oscillating frequency. In the work of S. Kawata and Y. Inouye [82], a metallic STM probe was placed in the evanescence field generated by total internal reflection at a prism, therefore measuring the surface profile by conventional STM and extracting the surface optical properties from the scattered near-field. Since then, there has been a tremendous development

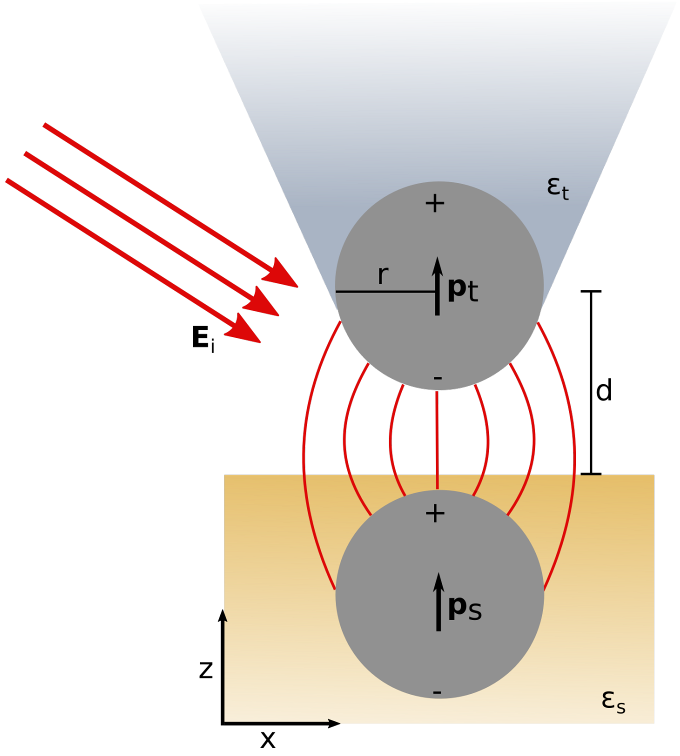

FIGURE 2.3: Point dipole model
Incident radiation on a metallic tip with radius $r$ and dielectric permittivity $\epsilon_t$ induces dipole moment $\mathbf{p}_t$. Mirror dipole is generated in the sample with permittivity $\epsilon_s$ at a distance $d$ from the tip's apex.

in this field yielding various sSNOM setup designs according to the nature of tip-sample interaction and detection schemes. Throughout this work, sSNOM system based on elastic scattering was used. Upon incident light on a non-resonant AFM tip, a localized electromagnetic near-field is generated at the tip's apex.

#### 2.2.3.1 Scattered near-field generation and the coupled dipole model

Bringing a sample in the tip's proximity results in tip-sample interaction which can be described by the coupled point dipole model [37, 83, 21]. The tip's apex is approximated to a polarizable sphere with radius $r_t$ and dielectric permittivity $\epsilon_t$ (Figure 2.3). The incident field $\mathbf{E_i}$ induces a dipole moment $\mathbf{p_t}$ which can be expressed through the tip's polarizability $\alpha$ [84]

$$\mathbf{p_t} = \alpha \mathbf{E_i} \quad \text{where} \quad \alpha = 4\pi r_t^3 \frac{\epsilon_t - 1}{\epsilon_t + 2}. \tag{2.7}$$

The dipole moment generated at the tip, induces a mirror-dipole in the sample with matching direction and an amplitude scaled by the reflection coefficient $\beta$ of the sample, approximated to point dipole at distance $-d$. In terms of the sample's permittivity $\epsilon_s$, the mirror dipole is given by

$$\mathbf{p_s} = \beta \mathbf{E_i} \quad \text{where} \quad \beta = \frac{\epsilon_s - 1}{\epsilon_s + 2}. \tag{2.8}$$

The coupling of the tip and sample dipole gives rise to a modified polarizability, termed effective polarizability $\alpha_{eff}$ expressed as

$$\alpha_{eff} = \frac{\alpha(1+\beta)}{1 - \frac{\alpha\beta}{16\pi(r_t+d)^3}}. \tag{2.9}$$

Accordingly, the net induced dipole moment is given by

$$\mathbf{p} = \mathbf{p}_t + \mathbf{p}_s = \alpha_{eff} \mathbf{E}_i. \tag{2.10}$$

Equations 2.9 and 2.10 imply that the incident field on a tip being close to a sample induces a dipole resulting from the tip-sample dipole coupling and is defined by the permittivity of the tip and the sample, the distance between them and the tip apex size. The incident field is then scattered from the thusly induced coupled dipole according to

$$\mathbf{E_s} \propto \alpha_{eff}\mathbf{E_i} \propto se^{i\varphi}\mathbf{E_i} \quad \text{for} \quad \alpha_{eff} \in \mathbb{C}. \tag{2.11}$$

The scattered field is thus proportional to an amplitude $s$ of the $E_i$ and phase shifted by $\varphi$. The near-field response can be represented by the scattering coefficient $\sigma(\omega) = \mathbf{E}_s/\mathbf{E}_i$ and is directly related to the optical properties of the sample [85, 86]. Namely, the scattered amplitude is proportional to the real part of the sample's dielectric constant $Re(\sigma(\omega)) \propto Re(\epsilon(\omega))$ and the imaginary part is proportional to the complex dielectric constant $Im(\sigma(\omega)) \propto Im(\epsilon(\omega))$ [38, 87]. In turn, the complex dielectric constant can be expressed in terms of the index of refraction $n$ and absorption $\kappa$ [88, 25] as

$$Re(\epsilon) = n^2 - \kappa^2 \quad \text{and} \quad Im(\epsilon) = 2n\kappa. \tag{2.12}$$

Usually the recorded signal on a given sample $\sigma$ is referenced against the signal $\sigma_{ref}$ on the substrate to cancel the contributions related to the response of the setup. This yields the near-field contrast defined by $\eta = \sigma/\sigma_{ref}$ [89].

**Refined coupled dipole model** To obtain a more accurate description of the interaction between the tip and the surface and a better agreement with experimental data, the finite-dipole model (FDM) was introduced [90]. The concept of FDM is based on the point-dipole model where the tip is approximated to a spheroid instead polarizable sphere (Figure 2.4). Implementing this geometry the effective polarizability becomes

$$\alpha_{eff} = R^2L\frac{\frac{2L}{R} + ln\frac{R}{4eL}}{ln\frac{4L}{e^2}}\left(2 + \frac{\beta(g - \frac{R+H}{L})ln\frac{4L}{4H+3R}}{ln\frac{4L}{R} - \beta(g - \frac{3R+4H}{4L})ln\frac{2L}{2H+R}}\right), \tag{2.13}$$

where $R$ is the spheroid's curvature radius, $2L$ its length and $H$ the distance between the spheroid and the sample.

In sSNOM the AFM is typically operated in tapping mode, which can be implemented in the FDM [91] by substituting $H$ with

$$H(t) = H_0 + A(1 + \cos \Omega t). \tag{2.14}$$

The strong dependence of the near-field on the tip-sample distance is exploited for background suppression, elaborated in more detail in Chapter 2.2.3.2. Upon incident light, a dipole is induced with associated point charges $\pm Q_0$ located at each of the ends of the spheroid that subsequently generate mirror charges $\pm Q_i$ in the sample as a result of the near-field interaction between the tip and the sample. In addition to the direct illumination of the tip by the incident light, part of the light that reflects from the surface illuminates the tip [92, 93]. Including contributions due to reflection, the scattered field is given by

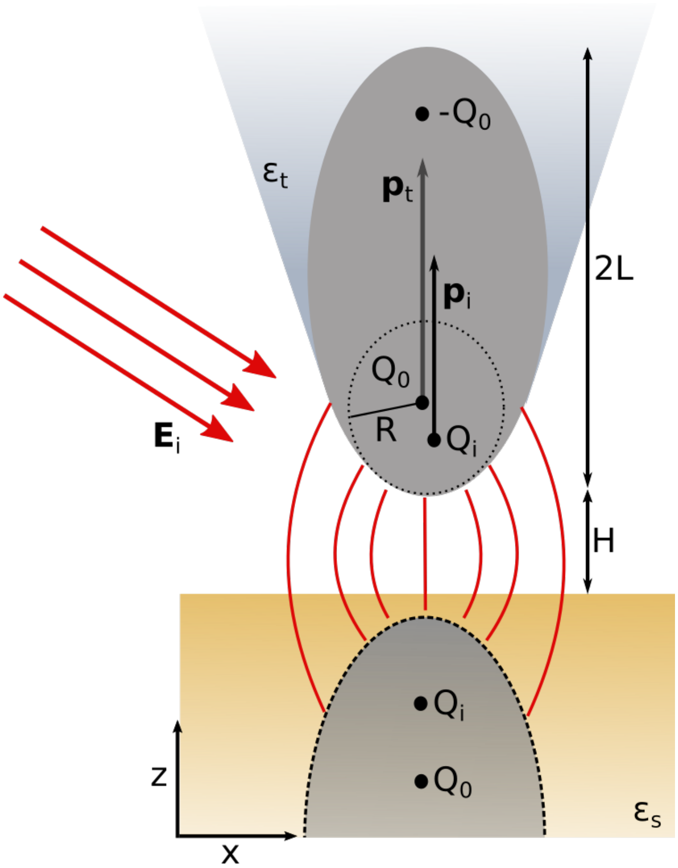

FIGURE 2.4: Finite-dipole model
An AFM probe is approximated to a spheroid with length 2L and radius R. Incident light $E_i$ induces dipole moment $p_t$ corresponding to point charge $Q_0$. Upon tip-sample interaction, mirror charge $Q_i$ is induced in the sample which in turn induces dipole $p_i$ in the tip.

$$\mathbf{E}_s = (1 + r)^2 \alpha_{eff} \mathbf{E}_i, \tag{2.15}$$

where the term $(1+r)^2$ accounts for Fresnel reflection of incident light on flat surface.

**Multilayered samples** Up to now the analytical models considered a semi-infinite sample with reflection coefficient $\beta$. Multilayered samples described by their thickness $t_i$ and the single-interface reflection coefficients $\beta_{ij}$ can be implemented in the FDM by substituting for $\beta$ in the Equation 2.13. The momentum dependent reflection coefficient $\beta(q)$ is given by [94, 91]

$$\beta(q) = \frac{\beta_{01} + \beta_{12}e^{-2qt_1}}{1 + \beta_{01}\beta_{12}e^{-2qt_1}}. \tag{2.16}$$

Each of the single-interface reflections are given by $\beta_{ij} = (\epsilon_j - \epsilon_i)/(\epsilon_j + \epsilon_i)$. This extended model matches the experimental data obtained for films with varying thickness [95] and can be employed in identification of subsurface layers [96].

#### 2.2.3.2 Scattered near-field detection

Typically, the scattered field from the tip overlaps with scattering from the tip shaft, the cantilever or stray scattering from the sample. Only the tip-scattered light carries information on the optical properties of the sample in a spatially confined volume. Therefore, extracting precisely this contribution from the detected signal is essential for high resolution imaging not limited by diffraction. For that purpose, the non-linear dependence of the near-field scattering on the tip-sample distance $d$, evident from Equation 2.9, is exploited. By periodically changing the tip-sample distance at frequency $\Omega$ or at higher harmonics $n\Omega$ with an amplitude $A$ according to Equation 2.14, the near-field magnitude and phase are also modulated, sharply increasing with decreasing distance [97, 98]. This behavior is unique to the tip-scattered light and therefore demodulating the detected signal at the tip's oscillating frequency yields the near-field scattering contribution. The scattered near-field at harmonics $n$ can be expressed in terms of the series

$$\mathbf{E}_s(t) = \sum_{n=-\infty}^{\infty} \varepsilon_n e^{in\Omega t}. \tag{2.17}$$

Demodulating at higher harmonics ($n = 2, 3...$) of the tip's tapping frequency $\Omega$ results in separating the near-field contribution to the detected signal and therefore more effective background scattering suppression [83].

To obtain a reliable sSNOM contrast that represents the optical properties of the sample, separate detection of the scattering amplitude and phase is necessary. This is achieved by employing an interferometric detection scheme. Moreover, via this approach the contributions from the remaining background scattering that interfere with the near-field signal (self-homodyne interference) become negligible. Throughout this work a Michelson interferometer with pseudo-heterodyne scheme [99] has been used. Other schemes include Michelson interferometer with homodyne [100] and Mach-Zehnder interferometer with heterodyne detection [38]. In the pseudo-heterodyne approach the phase reference arm of the interferometer is sinusoidally modulated with frequency $M$ and amplitude $\gamma$. The modulated reference field reads

$$\mathbf{E}_r(t) = \mathbf{E}_r e^{i\gamma\cos(mMt)} e^{i(\omega t - \varphi_r)} = \left(\sum_{m=-\infty}^{\infty} \varepsilon_{r,m} e^{imMt}\right) e^{i(\omega t - \varphi_r)}, \tag{2.18}$$

where $m = 1, 2, 3...$ denotes the harmonic of $M$ and $\epsilon_{r,m} = \varepsilon_r J_m(\gamma) e^{im\pi/2}$ for the Bessel function of first kind $J_m(\gamma)$. Interference of the scattered and reference field at the detector yields

$$I = |\mathbf{E}_s + \mathbf{E}_r|^2 = \left|\left(\sum_{n=-\infty}^{\infty} \varepsilon_s e^{in\Omega t}\right) e^{i(\omega t - \varphi_s)} + \left(\sum_{m=-\infty}^{\infty} \varepsilon_r e^{imMt}\right) e^{i(\omega t - \varphi_r)}\right|^2 . \tag{2.19}$$

In frequency domain, the double-modulated signal occurs at discrete frequencies $n\Omega$ and sidebands at $n\Omega \pm mM$, as depicted in Figure 2.5. The intensity at a given sideband can be expressed as

$$I_{n\Omega,mM} = C\left(2(\varepsilon_r\varepsilon_s) J_m(\gamma) \cos\left(\varphi_s + \varphi_r - \frac{m\pi}{2}\right)\right), \tag{2.20}$$

where the constant $C$ comprises the device-dependent contributions. The scattered near-field can be retrieved from the modulus of $I(n\Omega, mM)$ or the real part $\Re(I(n\Omega, mM))$ [101].

The sSNOM contrast is usually represented by the amplitude $s_n$ and the phase $\varphi_n$ of the complex scattering given by $\sigma_n = s_n e^{i\varphi_n}$. Consequently, sSNOM probes the local reflection and absorption of the sample at spatial resolution defined by the tip's size regardless of the wavelength of the incident light. Exceptionally valuable is the application of sSNOM to long-wavelentgh radiation such as the midIR spectral region where multitude of molecules show strong absorption features yielding images with contrast intrinsic to vibrations of chemical bonds. Widely used IR light sources are quantum cascade lasers (QCLs) [17] offering high output power. Additionally, the presented near-field methodology has been applied to imaging with THz radiation [102, 103] well beyond the diffraction limit [104]. The sSNOM principle has been extended to spectroscopy by utilizing broadband radiation. Much like in a conventional Fourier-transformed infrared (FTIR) spectroscopy [105], the interference between the interferometer arms is converted to spectrum. In the following chapter, the fundamentals of FTIR spectroscopy will be discussed, followed by description of near-field FTIR spectroscopy based on sSNOM technology.

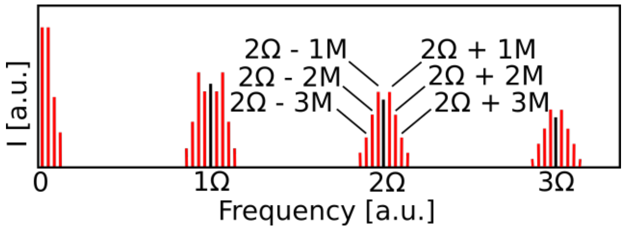

FIGURE 2.5: Double demodulation in pseudo-heterodyne sSNOM Demodulation of the scattered signal at higher orders $n$ of the tip's resonant frequency $\Omega$ and at $m$ of the reference mirror oscillating frequrncy $M$ resulting in sidebands $n\Omega \pm mM$. Figure adapted from [100].

## 2.3 Vibrational Spectroscopy

Vibrational spectroscopy probes the light-matter interaction in the infrared electromagnetic range. Absorption of IR radiation results in transition between the molecular vibrational states. The energy of a vibration of chemical bond between molecules can be approximated to the potential energy of a spring behaving like a harmonic oscillator [106]. In addition to vibrations due to displacement of atoms, the molecules experience various forms of interactions such as translation and rotation of the whole molecule, electronic resulting from the motion of electrons or nuclear originating from the electron and nuclear spin. In the following description of molecular vibrations, the molecules remain in the electronic ground state and the electronic contributions to the molecular energy will be neglected, an approximation known as the Born-Oppenheimer approximation [107].

Considering a diatomic molecule where the masses of the atoms $m_1$ and $m_2$ are bonded by a spring with constant $\kappa$, Hooke's law describes the restoring force resulting from displacement $\Delta x$ from the equilibrium position according to the relation $F = -\kappa \Delta x$ [108]. The potential energy stored in the spring is given by

$$V = -\int F dx = \int \kappa \Delta x \quad dx = \frac{1}{2}\kappa \Delta x^2. \tag{2.21}$$

The equivalent kinetic energy of the oscillating motion reads

$$E_k = M \left(\frac{d\Delta x}{dt}\right)^2 \qquad \text{for} \qquad M = \frac{m_1 m_2}{m_1 + m_2}, \tag{2.22}$$

where $M$ denotes the reduced mass. Energy conservation requires the sum $E_k + V$ to be constant and $dE_k/dt + dV/dt$ to be zero:

$$\frac{dE_k}{dt} + \frac{dV}{dt} = \frac{d^2\Delta x}{dt^2} + \frac{\kappa}{M}\Delta x = 0. \tag{2.23}$$

The solution to Equation 2.23 reads $\Delta x = a\cos(\omega t + \varphi)$, where $a$ denotes the amplitude, $\omega$ angular frequency and $\varphi$ phase. The frequency of the harmonic motion reads

$$\nu = \left(\frac{1}{2\pi}\right)\sqrt{\frac{\kappa}{M}}. \tag{2.24}$$

The total energy of this system can be expressed in terms of the spring constant and the displacement as $E = \frac{\kappa \Delta x}{2}$. In this classical description the energy can take any value and thus fails to describe discrete vibrational levels. Quantum mechanical formulation of the harmonic oscillator system remedies the shortcomings of the classical approach applied to molecular vibrations [109]. The total energy is described by the Hamiltonian $\hat{H}$ and the time-independent Schrödinger equation [110]

$$\hat{H}\Psi = E\Psi \qquad \text{for} \qquad \hat{H} = \frac{\hat{p}^2}{2m} + \frac{\kappa \hat{x}^2}{2}. \tag{2.25}$$

Substituting for the momentum operator $\hat{p} = -i\hbar d/dx$, the angular frequency $\omega = \sqrt{\kappa/M}$ in terms of the reduced mass $M$ and for the position operator $\hat{x}$, the displacement from equilibrium position $\Delta x$, the Schödinger equation reads:

$$E\Psi = \frac{\hbar^2}{2M}\frac{d^2\Psi}{dx^2} + \frac{1}{2}M\omega^2\Delta x^2\Psi. \tag{2.26}$$

The energy eigenvalues are given by

$$E_n = \hbar\omega\left(n + \frac{1}{2}\right). \tag{2.27}$$

The quantized energy values $E_n$ imply that the oscillation energies have discrete values where $n$ is the vibrational quantum number and the energy levels are equidistant. According to Equation 2.27 the lowest energy of the system is at $n = 0$ and it has a non-zero value of $\hbar\omega/2$, defined as the zero-point energy of a ground state. While the harmonic oscillator model describes accurately the energy and the oscillating frequencies of a diatomic molecule, it fails to address the effects from large displacements leading to dissociation and existence of unbound states. A more accurate version of Equation 2.27 is obtained by adding the Morse potential $V_{Morse}(x) = V_0(1 - e^{-a(x-x_0)})^2$, resulting in an anharmonic oscillator described by [111]

$$E = \hbar\omega \left(n + \frac{1}{2}\right) - \hbar\omega\chi \left(n + \frac{1}{2}\right)^2 , \tag{2.28}$$

where $\chi$ is an anharmonicity constant. The vibrational energy levels in Equation 2.28 are no longer equidistant. Instead, the distance decreases with increasing $n$. The change in electric dipole moment due to vibrations with small amplitudes can be expressed using Taylor series in terms of the molecular permanent dipole $\mu_0$ and sum of changes of the dipole upon displacement form the equilibrium position x as follows:

$$\mu = \mu_0 + \frac{d\mu}{dx}x + \frac{1}{2}\frac{d^2\mu}{dx^2}x^2 + ... \quad . \tag{2.29}$$

Until now only the inter-molecular interactions of diatomic molecules were considered. The vibrational energy in Equation 2.27 and 2.28 can be expanded to molecules with N number of atoms. In Cartesian coordinate system the molecule can move in 3N ways, i.e has 3N degrees of freedom. Neglecting translation and rotation motions, a polyatomic molecule has 3N-6 vibrational degrees of freedom. In the case of linear molecules, the number of vibrations is 3N-5. The total vibrational energy is then the sum of all energies given by

$$E_{tot} = \sum_{i}^{3N-6} \hbar\omega_i \left(n_i + \frac{1}{2}\right) , \tag{2.30}$$

for a harmonic oscillator approximation and by

$$E_{tot} = \sum_{i}^{3N-6} \hbar\omega_i \left(n_i + \frac{1}{2}\right) + \sum_{i \geq k} \sum_{k}^{3N-6} \hbar\omega_k\chi_{ki} \left(n_k + \frac{1}{2}\right) \left(n_i + \frac{1}{2}\right) , \tag{2.31}$$

for an anharmonic oscillator approximation.

Substituting $3N-6$ with $3N-5$ yields the total vibrational energy for linear molecule. Polyatomic molecules experience various forms of vibrational motions. Stretching vibration ($\nu$) typically results in increasing the bond length. For cyclic molecules that experience symmetrical increment of the bonds length, the vibrations are often refered to as ring breathing modes. Additionally, vibrations can manifest in several forms of deformation modes such as: i) angle deformation or bending ($\delta$) resulting in change of the angle between bonds, ii) rocking (r or $\rho$) when a moiety is displaced with respect to the rest of the molecule, iii) wagging ($\omega$) caused by change of the angle between bond and plane or change of the plane of atoms with respect to the plane of the molecule, iv) out of plane bending ($\pi$) resulting from motion of atoms out of the molecular plane, v) twisting ($\tau$) representing change of the dihedral angle between two planes defined by two groups of atoms [112].

### 2.3.1 Fourier Transform Infrared Spectroscopy

The interaction of IR light with matter can be represented in an IR spectrum, a plot showing the IR intensity with respect to the light frequency or wavelength. Measuring spectra was initially carried out using dispersive spectrometers, consisting of light source dispersed by prism or diffraction grating [113]. This design limits recording spectra to narrow spectral range and high signal-to-noise ratio demands lengthy acquisition times and powerful sources which was particularly disadvantageous in the IR spectral range where strong light sources were not available. Interferometric spectrometers on the other hand utilize broadband illumination to record spectra over a broad spectral range. A Fourier transform infrared (FTIR) spectrometer is usually based on a Michelson interferometer [114]. Incident light is guided to a beamsplitter which splits the beam in two arms, one containing a fixed mirror and the second a movable mirror thus resulting in an optical path difference (OPD) or retardation $\delta$ between the two arms. Recording the interference of both arms with respect to the OPD yields an interferogram.

The intensity as a function of the retardation that reaches the detector at a frequency $\nu_0$ is given by [115]

$$I_{det}(\delta) = 0.5I(\nu_0)(1 + \cos 2\pi\nu_0\delta). \tag{2.32}$$

The constant, or the dc, term $0.5I(\nu_0)$ does not change with the OPD. The interferogram is defined by the modulated, or the ac, term as

$$I(\delta) = 0.5I(\nu_0) \cos 2\pi\nu_0\delta. \tag{2.33}$$

For broadband radiation comprising of many frequencies, the interferogram can be expressed by integrating the intensities over the full frequency range $I(\nu)$

$$I(\delta) = 0.5 \int_{-\infty}^{\infty} I(\nu) \cos(2\pi\nu\delta) d\nu. \tag{2.34}$$

Fourier transformation of the interferogram $I(\delta)$ to $I(\nu)$ in frequency space yields a FTIR spectrum

$$I(\nu) = \int_{-\infty}^{\infty} I(\delta) cos(2\pi\nu\delta) d\delta. \tag{2.35}$$

The integral spans values from $-\infty$ to $\infty$ for the retardation $\delta$, however the translation of the movable mirror is in reality limited. This can be addressed by multiplying the Equation 2.35 by a function with zero values beyond the maximum displacement $\Delta$. A function that fulfills this criteria, known as Boxcar function, can be defined as follows

$$D(\delta) = \begin{cases} 1 \quad \text{if} \quad -\Delta \leq \delta \leq \Delta \\ 0 \quad \text{if} \quad \Delta > |\Delta| \end{cases}. \tag{2.36}$$

The modified Equation 2.35 then reads

$$I(\nu) = \int_{-\infty}^{\infty} I(\delta) D(\delta) cos(2\pi\nu\delta) d\delta. \tag{2.37}$$

This truncation results in sidelobes around the center burst of the interferogram originating from the FT of the Boxcar function which can be remedied by applying apodization functions such as triangular, Gaussian, Blackmann-Harris, to name a few. The finite displacement of the movable mirror implies that the spectral resolution $\Delta\nu$ of the spectrometer is also finite and can be related to the maximum mirror translation distance $\Delta_{max}$ as $\Delta\nu = 1/\Delta_{max}$.

In most conventional spectrometers the sample is positioned outside the Michelson interferometer such that the two interfering beams pass through the specimen and reach the detector. This configuration is known as FTIR in transmission. The interferogram thus contains information of the interaction between the irradiation and the sample and can be expressed in terms of transmittance or absorbance [14]. The fraction of light that passes through the sample is the transmittance $T = I/I_0$ where $I_0$ is the light intensity without the sample and $I$ is the intensity reaching the detector after the sample. The absorbance is given by $A = \log_{10} 1/T$. The sample configuration in the spectrometer can be modified to exploit particular aspects of light-matter interaction. In the following attenuated total reflection ATR-FTIR based on total internal reflection at an interface and nano-FTIR operating in the near-field generated at a sharp metallic tip will be discussed.

## 2.3.2 Attenuated Total Reflection (ATR)

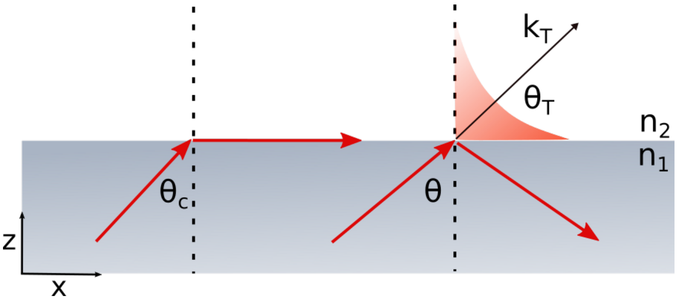

FIGURE 2.6: Attenuated total reflection Incident light at an interface between two media with refractive indices $n_1 > n_2$ under an angle $\Theta$ for $\Theta > \Theta_c$ results in an evanescent field decaying exponentially away from the surface, where $\Theta_c$ is the critical angle under which total internal reflection occurs.

In contrast to conventional transmission FTIR, in ATR-FTIR, incident IR radiation is guided to an ATR element, often crystal with high reflectivity in the IR, under an angle $\Theta$ such that at the crystal-medium interface internal total reflection occurs [116]. For materials with refractive index $n_1$ and surroundings with index $n_2$, such that $n_1 > n_2$, the critical angle, depicted in Figure 2.6, can be derived from Snell's law as $\Theta_c = sin^{-1}(n_2/n_1)$. At impinging angles larger than the critical angle, $\Theta > \Theta_c$, a wave with wave vector $\mathbf{k_T}$ is transmitted, given by

$$\mathbf{E_T}(\mathbf{r}, t) = E_0 e^{-i(\mathbf{k}_T \cdot \mathbf{r} - \omega t)}. \tag{2.38}$$

In the spatial coordinates x and z, the transmitted k-vector is given by

$$\mathbf{k}_T = k_T(\sin\Theta_T)\mathbf{x} + k_T(\cos\Theta_T)\mathbf{z}, \tag{2.39}$$

for $\sin\Theta_T = n_1/n_2 \sin\Theta$. In order to fulfill $n_1 > n_2$ and $\Theta > \Theta_c$, $\sin\Theta_T$ has to be larger than 1, which implies that $\cos\Theta_T$ has to be complex

$$\cos\Theta_T = i\sqrt{n_1^2 \sin^2\Theta - n_2^2}. \tag{2.40}$$

Substituting for $\mathbf{k}_T$ in equation 2.38 it follows [117]

$$\mathbf{E}(\mathbf{r},\mathbf{t}) = E_0 e^{-i\omega t} e^{i2\pi n_1 kx \sin\Theta} e^{-2\pi kz\sqrt{n_1^2 \sin^2\Theta - n_2^2}}. \tag{2.41}$$

The transmitted E-field is propagating in x-direction and is exponentially decaying in z-direction, also known as evanescent field, given by $E_z = E_0 e^{-z/d}$ for

$$d = \frac{\lambda}{2\pi n_1 \sqrt{\sin^2\Theta - \left(\frac{n_2}{n_1}\right)^2}}, \tag{2.42}$$

where d denotes the penetration depth into the medium $n_2$ in z-direction.

### 2.3.3 Nano-FTIR

Nano-FTIR spectroscopy is the symbiosis of sSNOM imaging, described in Chapter 2.2.3 yielding IR images with nm spatial resolution, and FTIR spectroscopy, described in Chapter 2.3.1 yielding IR spectra with high spectral resolution [40]. Thus, nanoFTIR is a technique characterized with high spectral and spatial resolution. The near-field generation principles are the same as for sSNOM and the point-dipole model gives accurate description of the detected scattered E-field in terms of the sample's optical properties, its reflectivity and absorption. The detection scheme is modified such that the sample and the tip are located in one of the Michelson interferometer arms. The movable mirror is placed in the second arm, called the reference arm. This kind of configuration when the sample is positioned in one of the interferometer arms is known as asymmetric Michelson interferometer. Tip modulation at higher harmonics is still necessary to suppress the contributions from background scattering. The recorded interferogram as a function of the mirror displacement and extracted at the tip's harmonics $n\Omega$ is subsequently Fourier transformed to yield spectrum, much like in a conventional FTIR spectrometer. The amplitude and phase of the spectrum relate to the near-field reflectivity and absorption of the sample. The nanoFTIR absorption is given by [118]

$$A_n = \frac{r_{n,s}}{r_{n,r}} \sin(\varphi_{n,s} - \varphi_{n,r}), \tag{2.43}$$

where $r_{n,s}$ and $r_{n,r}$ denote the real part of the complex field measured on the sample of interest and on the substrate or other chosen reference respectively and $\varphi_{n,s}$ and $\varphi_{n,r}$ the phase of the complex field on the sample and on the reference demodulated at harmonics order $n$ of the tip's resonance frequency.

### 2.3.4 Stable isotope labeling in vibrational spectroscopy

Isotope labeling involves substituting an atom with an isotope of the same element. Stable isotope labeling (SIP) refers to usage of non-radioactive isotopes. Vibrational spectroscopy probes the molecule's vibrational modes and is sensitive to the presence of such label. This strategy can be applied to FTIR spectroscopy on biological samples to overcome challenges such as strong water absorption as well as to selectively detect particular functional groups [119]. The frequency of oscillation for diatomic molecule depends on the mass of the atoms, as derived from the classical harmonic oscillator model (Equation 2.24). Exchanging the mass of one of the atoms $m_1$ with the mass of the isotope $m_1'$, the frequency of vibration can be expressed as

$$\nu' = \left(\frac{1}{2\pi}\right)\sqrt{\frac{\kappa}{M'}} \quad \text{for} \quad M' = \frac{m_1' m_2}{m_1' + m_2}. \tag{2.44}$$

The shift in the vibrational frequency from $\nu$ to $\nu'$ [120] due to the changed reduced mass can be detected by FTIR spectroscopy.

## 2.4 Localized surface plasmons (LSPs)

The sensitivity of sSNOM heavily relies on the effective light scattering from an AFM probe. In surface-enhanced techniques such as surface-enhanced IR absorption spectroscopy (SEIRAS) [121, 122] and surface-enhanced Raman spectroscopy (SERS) [123], an electric field enhancement is generated upon irradiation of metallic particles and exploiting their plasmonic properties.

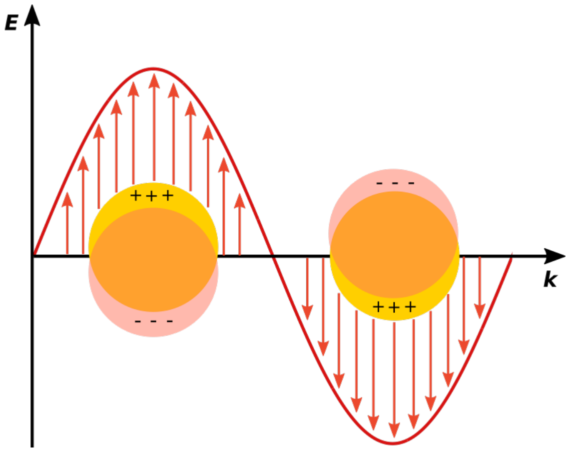

FIGURE 2.7: Localized surface plasmons Incident light **E** on subwavelength structures can induce oscillations of the conduction band electrons, called localized surface plasmons.

Irradiation of sub-wavelength metallic structures causes oscillation of the conduction band electrons (Figure 2.7). The displacement of the electron cloud upon interaction with the incident light, governed by coulombic force between the negatively charged electrons and the positively charged nuclei, results in restoring force. These electromagnetic oscillations occurring on a metal-dielectric interface are called surface plasmon polaritons SPPs [124]. Confinement of the plasmons to a subwavelength-sized structure results in non-propagating localized surface plasmons (LSP) [125]. One of the techniques used to excite and observe surface plasmons is via near-field microscopy [126]. Patterned surfaces, with plasmon resonances specifically tailored to match molecular vibrations have been shown to yield increased signal in SEIRAS [127]. Similar approach, utilizing resonant antenna substrates, can be used in combination with sSNOM to image the near-field of the structures [128, 129] and to potentially increase the sensitivity. The plasmon resonance frequency depends on the structure's material, dielectric properties, its size and shape [130]. Explicit theoretical description of spherical nanoparticles and their plasmonic effects upon light irradiation is part of Mie's theory [131]. More complex geometries usually rely on numerical methods such as finite-difference time-domain (FDTD) simulations [132]. Meanwhile, it has been shown that plethora of plasmonic structures are able to *squeeze* [133] incident radiation to the near-field, such as rods [134], bow-tie antenna [135, 136], nano-discs and nano-shells [137, 138], as well as plasmonic metamolecules [139, 140]. Furthermore, enhancing effects of resonant antenna have been exploited to improve the near-field signal in nanoFTIR and sSNOM [141, 142]. If the resonance of the plasmonic structures overlaps with a molecular vibration, coupling between the two oscillations can occur that result in increased electric field that the sample is exposed to and thus increase in the absorption [143]. The coupling of plasmonic oscillation with molecular oscillations can be modeled by coupling of two harmonic oscillators [144].

# Chapter 3

# Instrumentation and Materials

## 3.1 Atomic Force Microscopy

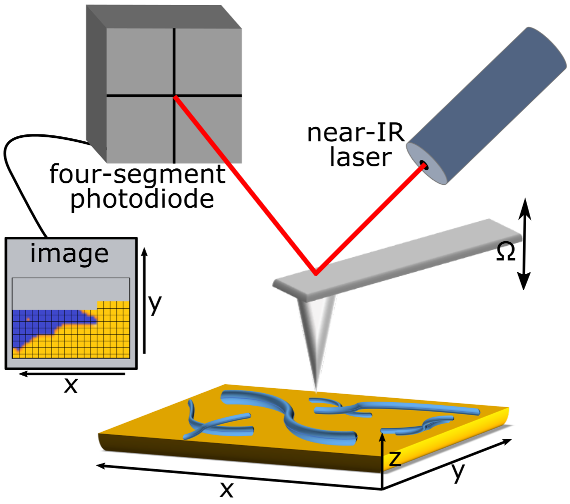

FIGURE 3.1: Atomic force microscope Tip-sample interaction causes tip deflection which is traced by a near-IR laser. The back-reflected light is guided to a four-segment photodiode. In tapping mode the tip is oscillating at its resonance frequency Ω. The image is formed by raster scanning the sample, where x is the slow and y the fast axis.

Throughout this work, the surface morphology of various samples was investigated with an atomic force microscope (Nanowizard II, JPK BioAFM, Bruker Nano GmbH, Germany). The microscope was operated in tapping mode in air. A near-IR laser (980 nm), reflected from the backside of the cantilever, is guided to the center of a four-segment photodiode, as schematically shown in Figure 3.1. Upon tip-surface interaction, the cantilever experiences bending which causes the reflected beam to hit the photodiode in a different region than the central position. Comparing the signal reaching each of the quadrants gives information on the vertical and lateral cantilever deformation. The AFM images were obtained by raster scanning the sample by moving the sample stage. Silicon (Si) tips suitable for tapping mode imaging in air, with resonance frequency in the range of 240-380 kHz, spring constant of 42 N/m and radius of less then 10 nm were used (Arrow-NC, NanoandMore GmbH, Germany). AFM images were visualized and evaluated using the free software Gwyddion v.2.51 [145].

## 3.2 sSNOM imaging

Near-field microscopy in the mid-IR spectral region was performed using a custom-made microscope developed in our research group as described in detail in Dr. Emanuel Pfitzner's doctoral thesis [146] and a commercial sSNOM spectrometer (NeaSNOM, NeaSpec GmbH, Germany). The sSNOM configuration, shown in Figure 3.2, is based on an asymmetric Michelson interferometer and utilizes the pseudo-heterodyne detection method [99], as described in Chapter 2.2.3.2.

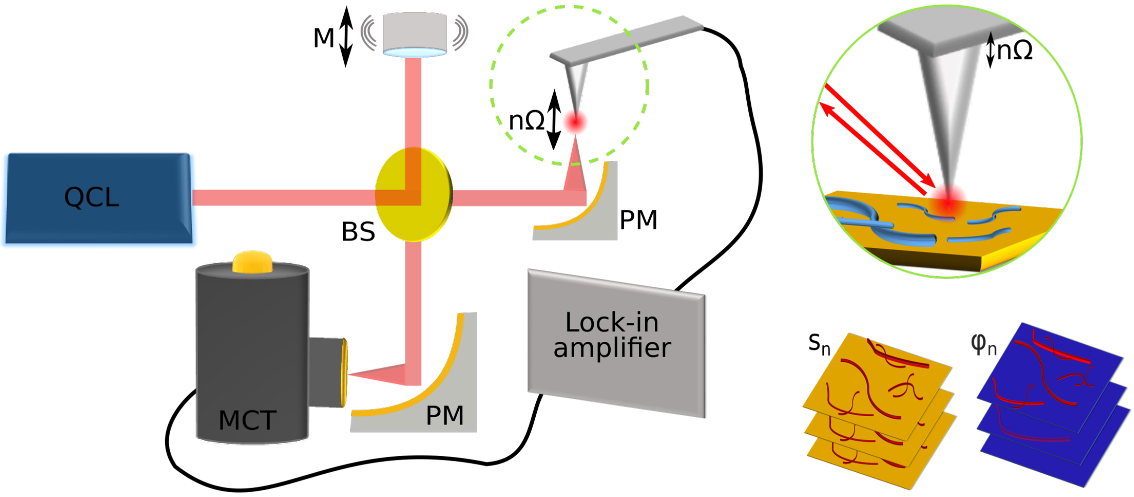

Figure 3.2: sSNOM setup in an asymmetric Michleson interferometer configuration equipped with a QCL beam focused, via parabolic mirror (PM), on an AFM tip oscillating at Ω. Half of the beam reflected at the ZnSe beam splitter (BS) hits a piezo-driven mirror. The light from both arms is recombined and focused on a MCT detector using PM. The detected signal is demodulated by a lock-in amplifier. sSNOM amplitude $s_n$ and phase $\varphi_n$ demodulated at higher harmonics of tip's resonance frequency $n$ are recorded.

The sample arm consists of an AFM (described in 3.1) operated in tapping mode using platinum-iridium ($PtIr_5$) coated tips (resonance frequency 240-380 kHz, spring constant 42 N/m, radius $<$ 25 nm) (Arrow-NCPt, NanoandMore GmbH, Germany). The metallic coating is necessary for effective IR light scattering [147]. Quantum cascade laser (QCL) (MG Optical Solutions GmbH, Germany) beam, passing a zinc selenide (ZnSe) beam splitter, is focused on the probe via gold-coated 0.5″ parabolic mirror (MPD00M9-M01, Thorlabs Inc., New Jersey, United States). In the reference arm, the IR beam reflected from the beam splitter, is guided to a vibrating mirror driven at around 300 Hz via a piezo actuator (P-843.10, Physik Instrumente (PI)GmbH & Co. KG, Germany). The back-scattered light from the tip and reference arm are re-combined at the beam splitter and guided to a 1″, gold-coated parabolic mirror (MPD129 M01, ThorlabsInc., New Jersey, United States) focusing the light on an IR sensitive mercury cadmium telluride (MCT) detector (KLD-0.01, Kolmar Technologies Inc., Massachusetts, United States). The detected signal is demodulated using a lock-in amplifier (HF2LI, Zurich Instruments AG, Switzerland) at the frequencies by $n\Omega + mM$, where $n$ denotes the harmonic order of the tip's resonance frequency $\Omega$ and $M$ the frequency of the piezo-driven mirror in the reference arm. This allows to extract the amplitude and phase of the scattered field. Simultaneously to AFM imaging, sSNOM amplitude and phase images are recorded at the wavelength of interest. Data acquisition was carried out via LabView v.15.0.0. Visualization and evaluation of sSNOM images was performed with Matlab v.R2017b.

**Commercial sSNOM system** The experiment described in Chapter 4.6.2 was carried out using a commercial sSNOM system (neaSNOM, neaSpec GmbH, Germany) equipped with four QCL chips covering the spectral range 900-1900 cm$^{-1}$ in side-illumination configuration. Pseudoheterodyne detection scheme was applied to extract the amplitude and phase of the complex scattered field. The region of interest is effectively located with an optical brightfield microscope, with spatial resolution of $<$ 0.8µm offering the possibility to gain an overview of the surface of interest and move the AFM tip to the selected area. This aided in performing sSNOM tomography presented in Chapter 4.6.2.1. Visualization and evaluation of sSNOM images was performed with the free software Gwyddion v.2.51 [145]. 3D reconstruction and visualization of sSNOM tomography images was done using Amira, Thermo Fisher Scientific, v.6.3.0.

## 3.3 NanoFTIR spectroscopy

The setup shown in Figure 3.2 was modified to perform Fourier transformed IR (FTIR) spectroscopy with nm-spatial resolution limited by the tip's radius (nanoFTIR) [40]. For this purpose, a femtosecond (fs) broadband IR laser source was used (FemtoFiber dichro midIR, neaSpec GmbH, Germany). The generated radiation output in the mid-IR spectral region covers the range 670-2000 cm$^{-1}$ with bandwidth of approximately 700 cm$^{-1}$. An Er fiber laser system produces a beam in the near-IR region and a broadened red-shifted beam. Both beams are recombined at a GaSe crystal where nonlinear frequency conversion takes place. Mid-ir continuum results from difference frequency generation (DFG) upon mixing of the 1.55 µm 100 fs pulses with the broadened beam pulses in the range 1.7 - 2.3 µm [148, 41].

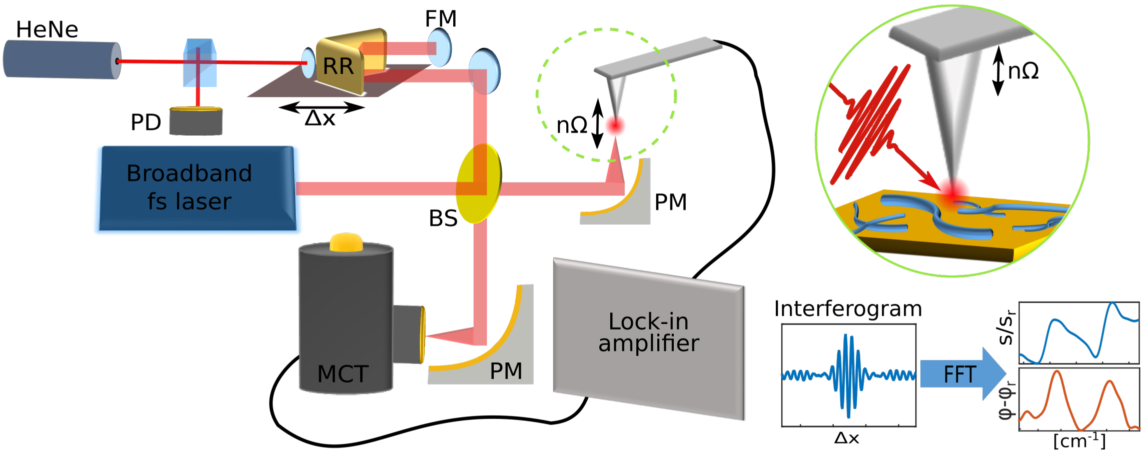

FIGURE 3.3: nanoFTIR setup in Michelson interferometer configuration. In the sample arm a broadband fs IR laser is focused on an AFM tip. The reference arm consists of a retroreflector (RR) mounted on a movable stage, translating the optical path by Δx, and folding mirror (FM). The beams re-combine at the ZnSe BS and the resulting IR light is focused on the MCT detector using PM. For the reference interferometer, a HeNe laser, cubic beamsplitter, silver mirror mounted on the movable stage and a photodiode (PD) are used.

The tip arm remains unchanged, whereas in the reference arm the beam is guided to a gold coated retroreflector (replicated hollow metal retroreflector 50326, Newport Spectra-Physics GmbH, Germany), a design that compensates tilt in the interferometer [115]. The retroreflector is mounted on a movable stage driven by a voice-coil (V-524, Physik Instrumente (PI), GmbH & Co. KG, Germany). It is thus possible to record the intensity of the two interfering arms as a function of the optical path difference yielding an interferogram [149]. To define the sampling of the IR interferogram, a second interferometer with a visible (632 nm) helium-neon (HeNe) laser is used. The movable mirror of this reference interferometer is mounted on the same stage as the retrorefelctor to obtain simultaneous displacement. Descrete sampling of the IR interferograms is achieved by data acquisition at the HeNe inteferogram zero-crossings. The detected IR signal is again demodulated at higher harmonics of the tip's resonance frequency via the lock-in amplifier. Fast Fourier transformation FFT is applied to the complex-valued interferograms leading to spectral information. The nanoFTIR absorption can be readily computed as previously described in equation 2.43 [118]. Data acquisition was carried out via LabView v.15.0.0. Visualization and evaluation of nanoFTIR spectra was performed with Matlab v.R2017b.

## 3.4 ATR-FTIR spectroscopy

Conventional FTIR spectroscopy was performed in an ATR configuration as shown in Figure 3.4. For that purpose, a spectrometer (Vertex 70, Bruker Optik GmbH, Germany) equipped with a two-reflection Si ATR cell (DuraSamplir II, Smiths Detection, United Kingdom) was used. Exploiting the evanescence field formed as a result of internal total reflection in the Si crystal, this geometry allows usage of relatively low amounts of sample. Typically, a sample volume of $2\mu l$ was deposited on the surface and dried with gentle air flow. FFT of the acquired interferograms was carried out by the software OPUS (Bruker Corporation, Massachusetts, United Sates). An absorption spectrum was obtained by recording a reference ($I_0$) and sample spectrum $I$, according to $-log(\frac{I}{I_0})$. The reference spectrum was recorded on a sample-free surface prior to sample deposition. Each measurement was performed in the spectral window of 4000 - 600 cm$^{-1}$.

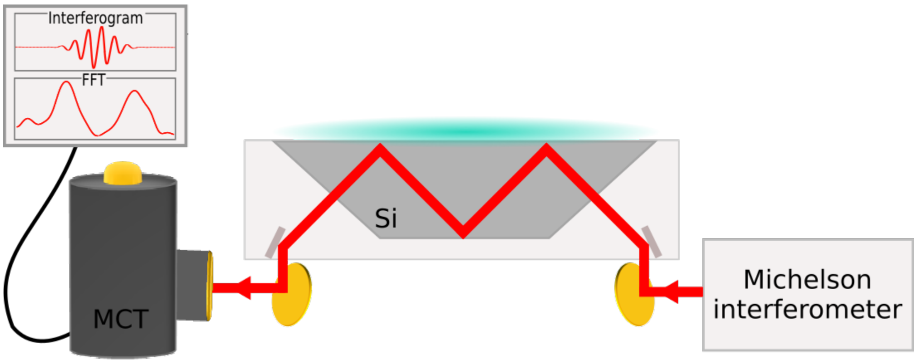

FIGURE 3.4: ATR-FTIR configuration
IR radiation is guided to a Si ATR element. The sample is applied on top of the Si crystal. The MCT detector records interferograms which, through fast Fourier transformation result in spectra.

## 3.5 Substrates

### 3.5.1 Template-stripped gold

AFM imaging requires topographically flat surfaces and near-field imaging and spectroscopy require surfaces with high and constant reflectivity and no absorption in the mid-IR region. For that purpose template-stripped gold Au (TS Au) surfaces [150] were manufactured using physical vapor deposition (PVD). Gold with purity 99,99% (Au, Kurt J. Lesker Company Ltd., Germany) was thermally evaporated on clean Si-wafer in an evaporation chamber (EcoVap3, MBraun GmbH, Germany) to obtain 100 nm thick Au films. Next, glass pieces with size of approximately 1cm x 1cm were cut off microscopy glass slides (Carl Roth GmbH + Co.KG, Germany) and glued on the Au film with an optically active adhesive [151] (NOA 81, Norland

Products Inc., New Jersey, United States). The adhesive was cured by illumination with UV lamp for approximately 2 minutes. The glass pieces were mechanically stripped off the wafer revealing fresh and flat Au-surfaces.

### 3.5.2 Disc antenna array

To investigate potential improvement of the near-field sensitivity effect of plasmonic structures, substrates patterned with gold discs were used. An approach based on nanostencil lithography [152], was utilized to manufacture Au disk antenna arrays. Au (99,99% Au, Kurt J. Lesker Company Ltd.) was thermally evaporated (EcoVap3, MBraun GmbH, Germany) on $CaF_2$ windows (Eksma Optics, Lithuania) using cryo-TEM grids (2/1 C-Flat, Protochips, N. Carolina, United States) as a mask. This yielded antenna arrays with diameter of 2 µm, periodicity of 3 µm in x and y direction and 50 nm thickness (Figure 3.5). The reported bandwidth covers the range 1200-2800 cm$^{-1}$, with a maximum peak at $\sim$ 1800 cm$^{-1}$ and a second peak $\sim$ 2200 cm$^{-1}$.

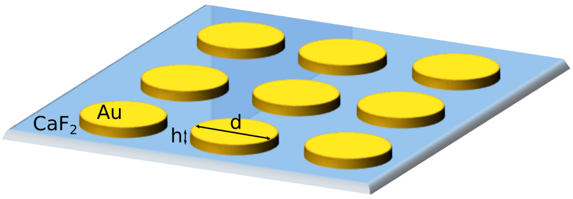

FIGURE 3.5: Disc antenna array
Gold disc antenna with diameter d = 2µm and height h = 50 nm evaporated on a CaF$_2$ window were used as a sSNOM substrate.

## 3.6 Purple Membrane

Purple membrane (PM) patches are naturally occurring in the cellular membrane of *Halobacteria* [153]. The main constituent of these patches is the transmembrane protein Bacteriorhodopsin (bR) [154]. It consists of seven $\alpha$-helices (Figure 3.6) and the chromophore molecule retinal embedded within [155]. The physiological role of bR is creating proton gradient across the membrane by acting as a light-driven proton pump [156]. The bR photocycle is initiated by light with $\lambda = 568$ nm [157]. The $\alpha$-helices are perpendicularly oriented with respect to the surrounding lipid bilayer and are grouped in trimers forming the regular trigonal PM lattice structure. PM from *Halobacterium salinarum* in this work were provided by AG Schlesinger (Genetic Biophysics, department of Physics at Free University Berlin).

The protocol for PM sample preparation suitable for AFM imaging was adapted from [158]. A droplet of 5.6 mg/ml purified PM with volume of 0.5 $\mu$l was mixed with buffer containging 10 mM 2-amino-2-hydroxymethyl-propane-1,3-diol (TRIS) and 300 mM KCl at pH 7.1 and deposited on freshly stripped Au substrate. After incubation time of 30 minutes, the surface was washed with Mili-Q water and dried under gentle air flow.

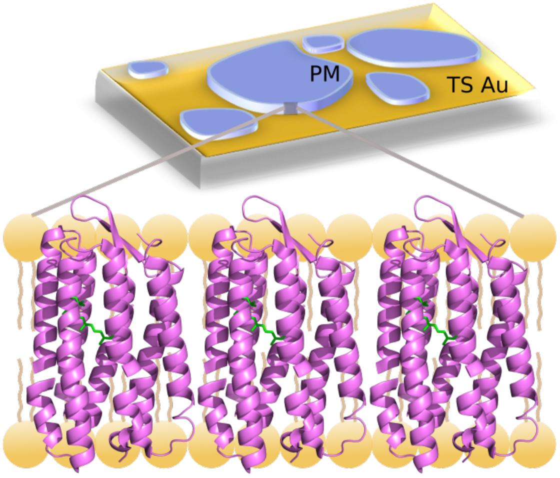

FIGURE 3.6: Purple membrane Patches are deposited on flat TS Au substrate. PM consists of densely packed seven-helical transmembrane protein Bacteriorhodopsin (bR).

## 3.7 Stimuli-triggered aggregating peptides

Peptides have the ability to undergo self-assembly into stable macroscopic structures when exposed to external stimuli [159]. The morphology and assembly mechanism of a synthetic $\alpha$-helical coiled coil peptide facilitated by pH and temperature were investigated. The stimuli-triggered aggregating peptides (STAP) were designed and synthesized by AG Koksch (Department of Chemistry and Biochemistry, Free University Berlin) based on their previous work [160], [161] and in-detail described in the work of Rita Fernandez [162]. The peptide consists of 29 amino acids and a cyanine dye (Cy5) attached to the N-terminus. The chemical properties of the amino acids and their distribution play an important role in ensuring formation of helical coiled coil. Four types of amino acids were arranged according to their hydrophobicity (h) and polarity (p) in hpphppp order. As hydrophobic residues leucine and glutamic acid were used, whereas lysine and serine as polar.

| | | | | | | |
|---|---|---|---|---|---|---|
| **STAP1** | Cy5 | LKSE | LKELKSE | LEKLKSE | LEKLKSE | LKEL |
| **STAP2** | Cy5 | LKSE | $F_3$VELKSE | $F_3$VKELKSE | $F_3$VKELKSE | LKEL |
| **STAP3** | Cy5 | LKSE | IKELKSE | IKELKSE | IKELKSE | IKEL |

Table 3.1: STAP sequences

| | | | |
|---|---|---|---|
| **L** | leucine | **K** | lysine |
| **S** | serine | **E** | glutamic acid |
| **$F_3$V** | trifluorovaline | **I** | isoleucine |

The sequence of the STAP1 peptide is shown in Table 3.1. Two mutations of STAP1 were introduced by substituting some of the amino acids to investigate the effects of hydrophobicity on the structures formation and stability. The first mutation (STAP2) included substitution of three leucines with the fluorinated residue trifluorovaline. In the second modified peptide (STAP3), four leucines were exchanged with isoleucine. The rest of the peptide sequence was left intact. Aggregation and formation of supramolecular structures was monitored in all three variants under acidic and neutral conditions. Peptides with concentration of 0.1 mM were buffered in 50 mM sodium citrate solution at pH 3.4 and 50 mM phosphate-buffered saline (PBS) solution at pH 7.4 for STAP1 and STAP2, and pH 7.1 for STAP3. In acidic conditions spontaneous formation of blue sediment in the eppi was visible. The peptides at neutral pH formed visible sediment only after thermal denaturation by heating to 95 °C and cooling down to 20 °C with rate of $3\frac{^\circ C}{min}$. For AFM imaging, near-field microscopy and spectroscopy, 5 $\mu$l of the peptides in buffer solution were spin coated (SCV-10, LOT-QuantumDesign GmbH, Germany) on TS Au substrates at 70 rps.

## 3.8 Patterned polymer brush surfaces

Polymer brushes are formed by densely attaching one end of polymer chains to a solid surface [163]. Polyelectrolyte (PE) brushes are formed from polymers carrying electrolyte groups [164]. A variety of external stimuli can be applied to such surfaces to induce large scale physical and chemical changes [165]. Here, the light-induced formation of surface relief gratings (SRGs) was investigated in two polymer brush complexes (Figure 3.7 a). For that purpose, poly(methacrylic acid) (PMAA) (Figure 3.7 b) and poly(3-sulfopropyl methacrylate/potassium salt) (PSPMK) (Figure 3.7 c) brushes were grown on Si wafers according to the procedure described in [166] and [167], respectively.

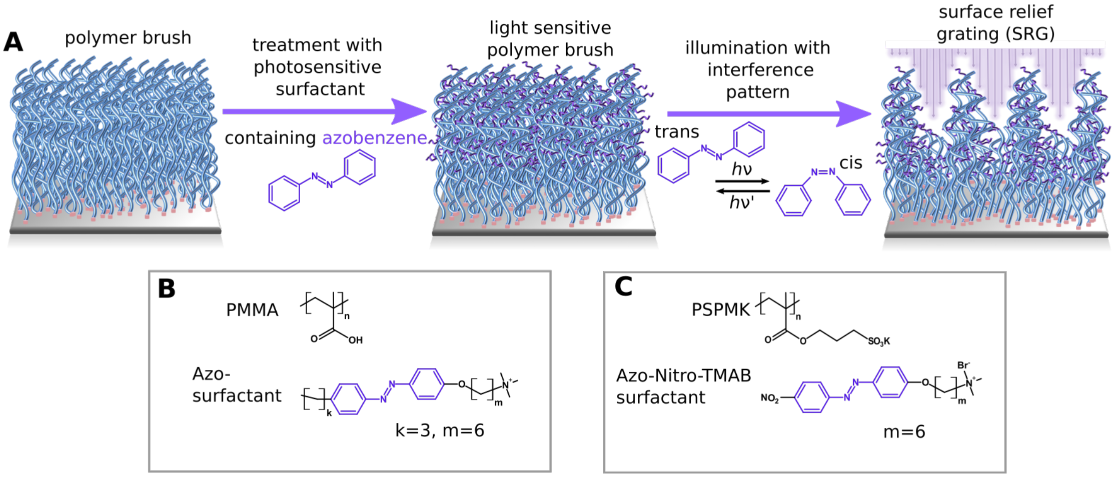

FIGURE 3.7: Surface relief gratings
**A** Polymer brushes are rendered photosensitive by attaching surfactant molecules containing azo-benzene. Upon illumination with UV light the azo-benzene moiety undergoes isomerisation which induces large-scale changes in the brushes. Surface patterning is achieved by illumination with interference pattern. **B** Chemical formulae of poly-methacrylic acid (PMMA) and azo-surfactant. **C** Chemical formulae of poly(3-sulfopropyl methacrylate/potassium salt) (PSPMK) which was treated with azobenzene containing trimethylammonium bromide (Azo-Nitro-TMAB) surfactant.

To render the brushes photo-sensitive, they were loaded with cationic surfactants containing azobenzene. PMAA was placed in an azo-surfactant solution for 16 h, followed by 15 min in water bath [168]. PSPMK was placed in an azobenzene containing trimethylammonium bromide (Azo-Nitro-TMAB) surfactant soultion for 0.5h, rinsed with water and dried under nitrogen flow [169]. The SRGs were formed under illumination with an interference pattern using a setup based on a Lloyd's mirror approach [170] at wavelength of 325 nm. The synthesis of the polymer-surfactant complexes, as well as the SRGs preparation was carried out by Nino Lomadze and Alexey Kopyshev from AG Santer (Institute of Physics and Astronomy, University of Potsdam).

## 3.9 Stable isotope labeling *E. coli*

Microbial metabolic activity at the single-cell level was investigated with the aid of stable isotope probing (SIP)combined with nanoFTIR spectroscopy. For that purpose, *E. coli* K12 (DSM 498) were grown in M9 medium (M9 Broth, 1.5 mM $MgSO_4$, 0.1 mM $CaCl_2$, Merek, Germany), supplemented with 4 g/L $^{13}C$ isotope labeled glucose ($^{13}C_6$ 99%, Cambridge Isotope Laboratories, USA) at different ratios. A total of eleven $^{12}C/^{13}C$ proportions were used, starting from 100 %/0% and increasing the $^{13}C$ content in steps of 10% until reaching 0%/100%. The cultures were fixed in 2.5% v/v glutaraldehyde fixative (Merck, Germany) after reaching a late exponential growth phase (37 °C, shaking at 120 rpm). To investigate the metabolic activity of single cells under carbon-limiting conditions, a second round of cultures were exposed to 100 % $^{13}C$ labeled glucose with concentration 0.04 g/L. The cells were collected during an early exponential growth phase, at 1.5 times the doubling time (dt=50 min). The cell growth, isotope labeling and fixation under the various conditions was carried out by David J. Burr (AG Elsaessar, Experimental Biophysics and Space Sciences, Department of Physics, Free University Berlin).

## 3.10 Cellular thin sections

Cellular thin sectioning offers the possibility to investigate the internal structure of cells and has been widely used in conventional optical as well as electron microscopy. In collaboration with AG Elsaessar (Experimental Biophysics and Space Sciences, Department of Physics, Free University Berlin), bacterial and algal thin sections sample preparation suitable for AFM, sSNOM and nanoFTIR experiments was established. *E. coli* and *C. reinhardtii* cultures were fixed in Cacodylate mixture fixative (0.1 M Cacodylate buffer, 2% formaldehyde, 2.5 % glutaraldehyde, 0.088 M sucrose, 0.001 M $CaCl_2.H_2O$, pH 7.4; Merck, Germany). The fixed cells were embedded in Agar Low Viscosity Resin (Agar Scientific, UK) prepared according to manufacturer's instructions. The resin block was cut using a microtome (Reichert ultracut S, Leica, Germany) equipped with diamond knife (DiATOME, Hatfield, PA, USA& Drukker, USA). Sections with thickness of 80-100 nm were carefully positioned on TS Au substrates. A series of consecutively sections sliced in trapezoidal form placed on the TS Au surface were used for sSNOM tomography. Fixation and embedding was performed by David J. Burr. *C. rheinhardtii* cultures were kindly provided by Dennis J. Nürnberg.

# Chapter 4

# Results and Discussion

## 4.1 Purple Membrane (PM): standard for setup validation

Several experiments were performed on PM of *Halobaterium salinarum* aimed to validate the home-build setup, described in Chapter 3.2. PM was selected for this task due to its high level of versatility and stability over time with a straightforward sample preparation. Additionally, PM's morphology and spectroscopic characteristics have been investigated with AFM, FTIR spectroscopy and near-field techniques which enables direct comparison of our findings with existing literature [171, 172]. Here, nanoFTIR and sSNOM are applied to investigate the near-field signal dependence on the sample's demodulating order and thickness.

### 4.1.1 nanoFTIR spectroscopy of PM

An exemplary far-field FTIR spectrum of PM in bulk was measured in an ATR mode. As shown in Figure 4.1 a, the spectrum is dominated by absorption at 1655 cm$^{-1}$ and at around 1540 cm$^{-1}$. The former band corresponds to the absorption of C=O stretching vibrations in peptide groups, termed as amide I, whereas the latter results from combination of N-H in-plane bending and C-N stretching vibrations, termed as amide II. Amide I and amide II are typical absorption bands in the mid-infrared spectrum of proteins [173].

AFM topography of PM dried on TS Au surface (Figure 4.1 b) reveals single layers with thickness of around 5 nm, matching with previous AFM imaging reports [174].

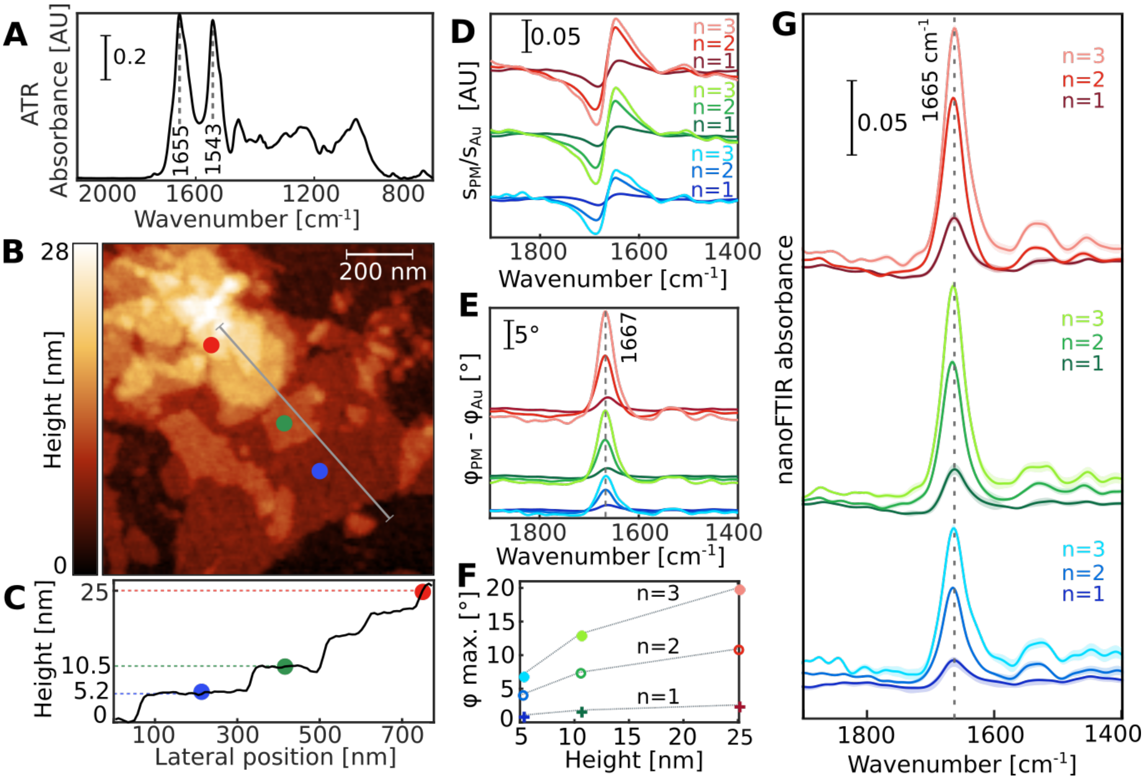

FIGURE 4.1: nanoFTIR spectroscopy on PM

**A** ATR-FTIR spectrum of PM. **B** AFM topography image of PM on TS Au. **C** Topography profile along the line shown in B (gray line). **D** Scattering amplitude spectra recorded at three locations equivalent to thickness of 5.2 nm (blue), 10.5 nm (green) and 25 nm (red) demodulated at the fundamental (n=1), second (n=2) and third (n=3) harmonic of the tip's resonance frequency. **E** Corresponding scattered phase spectra. **F** Phase contrast with respect to the sample thickness (PM height) for the fundamental, 1st and 2nd harmonic. **G** nanoFTIR spectra calculated according to equation 2.43 from the scattered amplitude and phase shown in (D) and (E).

Stacking of several membrane layers is also observed, which was well suited for the subsequent nanoFTIR spectroscopy measurements, performed on three spots corresponding to thicknesses of 5.2 nm, 10.5 and 25 nm (Figure 4.1 c). The near-field amplitude and phase spectra of PM referenced against the TSAu substrate demodulated at the tips resonance frequency (n=1) and at the higher, 2nd (n=2) and 3rd (n=3), harmonics are shown in Figure 4.1 d, e. The scattering amplitude, representing the real part of the scattered field, carries information on the reflectivity, while the phase of the scattered field is related to the local absorption of the sample with a maximum at 1665 cm$^{-1}$. The phase intensity depends on the demodulation order, as depicted in Figure 4.1 f. Higher demodulation order results in stronger near-field confinement, thus yields more effective extraction of the near-field contribution to the recorded signal and thus higher phase intensity [175, 176]. Comparing the absorption of a single membrane to that of multiple layers it becomes evident that increasing sample thickness results in stronger absorption. This is attributed to the larger number of molecular oscillators that contribute to the signal. NanoFTIR absorption was calculated from the amplitude and phase according to Equation 2.43. The near-field spectra of these protein-rich membranes are characterized by a strong absorption at $\sim$ 1665 cm$^{-1}$ assigned to amide I, however in the region around 1550 cm$^{-1}$, corresponding to amide II vibration, quite weak absorption is observed. Due to the high level of orientation of the $\alpha$ helices in PM, the C=O vibrations contributing to the amide I are perpendicular to the membrane plane and the molecular vibrations contributing to amide II are in plane [177]. The tip's dipole is directed along the z-direction, as discussed in Chapter 2.2.3 and Figure 2.3, and interacts with dipole changes originating from the sample along the same axis, while in-plane molecular dipole components are not detected, as previously reported in [171]. There is a discrepancy between the amide I peak position between the far-field ATR spectrum of PM in bulk and the near-field nanoFTIR spectra of thin PM layers. Namely, a shift towards higher wavenumbers, from 1655 cm$^{-1}$ to 1665 cm$^{-1}$, is observed in the nanoFTIR spectra. This blue shift is attributed to contribution from the highly-reflective Au surface. In addition to the near-field interaction between the tip and a thin sample layer, there is a near-field reflection from the substrate which resembles a reflection-absorption operation mode [95].

#### 4.1.1.1 nanoFTIR line scan

To measure the penetration depth of the near-field in nanoFTIR, a PM sample with gradually increasing thickness was used. The height profile across approximately 10 $\mu$m reveals maximum height of about 300 nm (Figure 4.2 a).

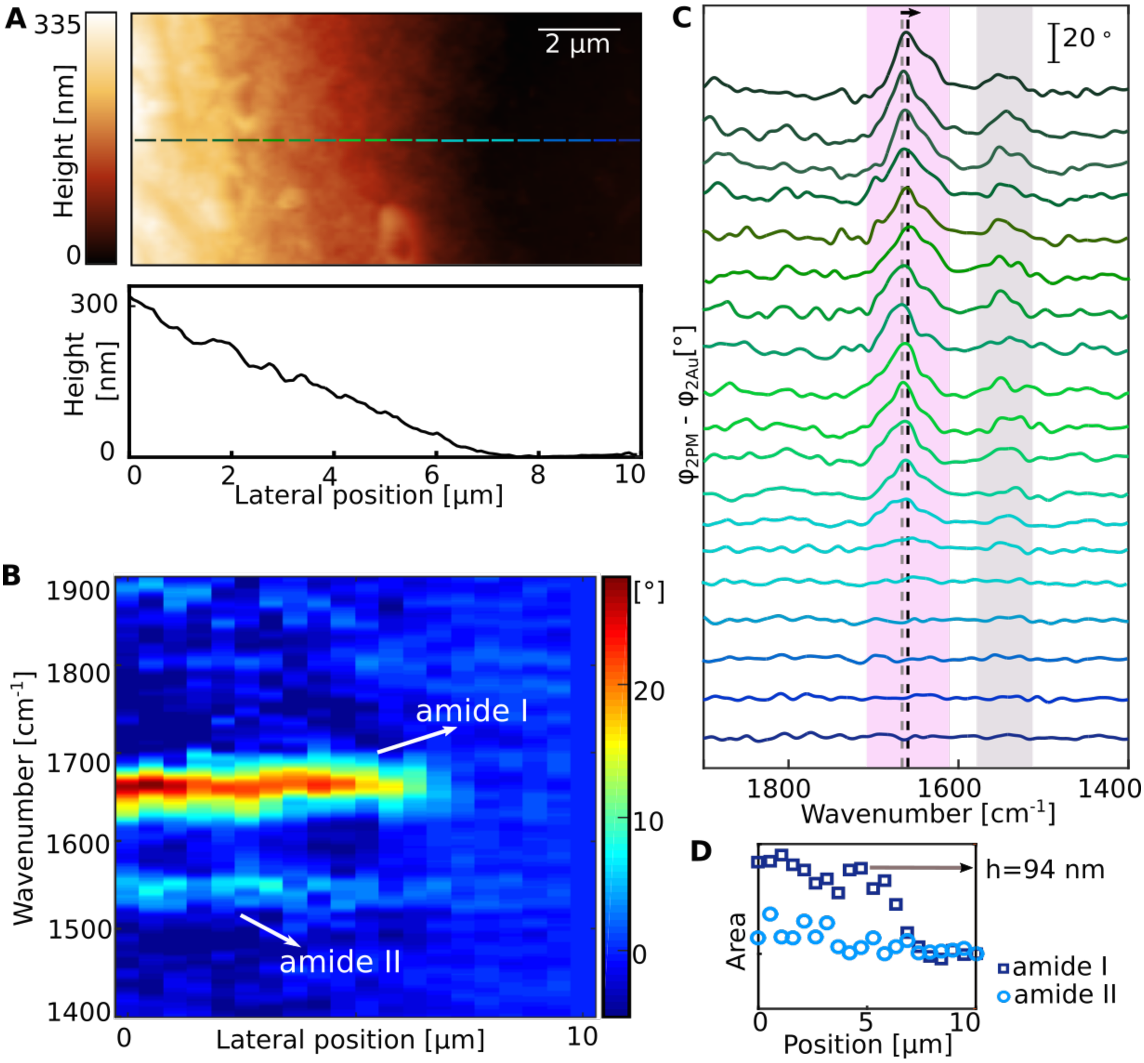

FIGURE 4.2: NanoFTIR line scan
**A** AFM topography image and height profile, corresponding to the dashed line in the image, of PM sample with gradually increasing thickness. **B** nanoFTIR phase measured along the dashed line in 20 steps. The map is referenced against the last spectrum measured on TS Au. **C** nanoFTIR phase spectra measured on each of the dashes in (A). **D** Integrated intensity over the area of the amide I and amide II peaks in (C) with respect to the lateral position. The marked position at which the amide I band saturates corresponds to thickness h.

Across this profile, 20 phase spectra were recorded, the last of which was used as a reference. The spectra at each of these points reveal strong absorption in the amide I region and weaker signature from amide II (Figure 4.2 b). The phase contrast increases with increasing thickness and the amide I peak position shifts from 1665 cm$^{-1}$ to 1660 cm$^{-1}$, as can be observed from the spectra shown in Figure 4.2 c. This red shift is due to decreasing contributions from the substrate and approaching bulk conditions [95, 96]. The increase in phase contrast is limited by the penetration depth of the near field. The area integrated under the amide I absorption peak (Figure 4.2 d) increases up to approximately 100 nm, after which the contrast doesn't significantly change [178, 179, 180]. In the amide II region the absorption intensity remains low throughout the measured lateral positions, which points at high ordering for even up to 60 PM layers.

### 4.1.2 sSNOM imaging

Complementary to nanoFTIR spectroscopy, sSNOM imaging was performed to investigate the absorption distribution at a wavenumber of interest across given area. The topography of the selected imaging area shows several PM patches with thickness below 5 nm (Figure 4.3 a, b). The areas covered with PM have overall low reflectivity compared to the Au surface (Figure 4.3 c), that decreases with the sample thickness, evident at areas where several layers are stacked. A line profile across the Au-PM interface shows lateral resolution for the sSNOM amplitude in the order of 30 nm. Phase image in the amide I region reveals contrast on a single PM layer of ~ 10 ° for n=3, with comparable lateral resolution of approximately 30 nm. The phase contrast and thus the absorption increases upon membrane stacking. A control measurement at 1691 cm$^{-1}$ showing no absorption confirms that indeed the observed contrast originates from near-field PM absorption. These findings are well in line with literature [171, 172] and the reported

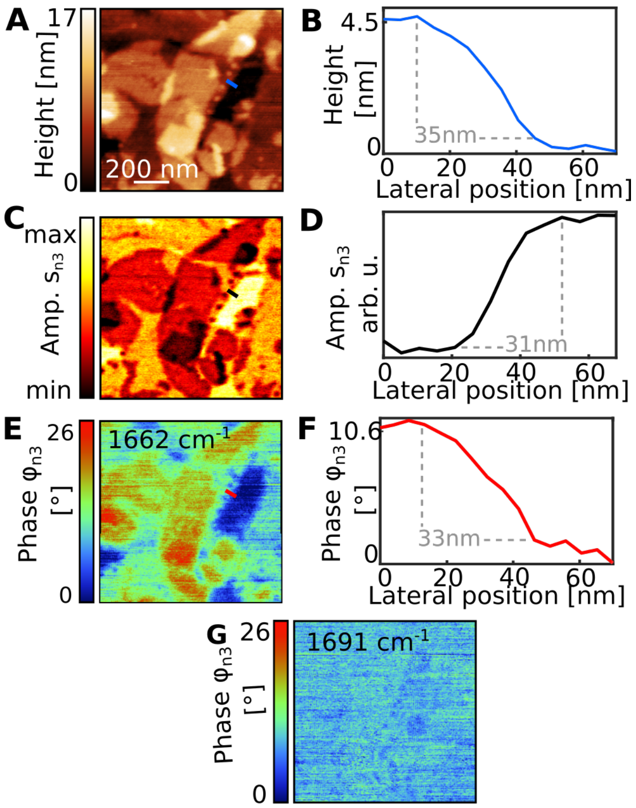

FIGURE 4.3: sSNOM imaging of PM
**A** AFM topography of PM patches on TS Au. **B** Height profile across the line marked with blue in (A). **C** sSNOM amplitude and **D** amplitude profile across the location marked in black. **E** sSNOM phase of the same area and corresponding phase profile **F**. Both were recorded at 1662 cm$^{-1}$ and demodulated at n=3. **G** Phase image recorded at 1691 cm$^{-1}$ and n=3.

measurements on this setup elaborated in Emanuel Pfitzner's work [146]. The sSNOM phase signal in dependence of the sample thickness was investigated using the stacked membranes with gradually increasing thickness (nanoFTIR spectra shown in Figure 4.3).

The AFM topography shows thickness equivalent to approximately 100 layers (Figure 4.4 a). Imaging at 1666 cm$^{-1}$ revealed strong absorption extending from the PM-Au border, however with increasing noise level (Figure 4.4 b). Smooth increase in the phase contrast is observed up to lateral position of 18.5 µm, or translated into height of 108 nm, marked in the phase profile , corresponding to line average of the shown image. Imaging beyond this region results in significant drop in the signal-to-noise ratio. The reported penetration depth for nanoFTIR and sSNOM is within the published values [181]. However, several imaging details, such as the AFM tapping amplitude, order of demodulation, the tip's radius to name a few, influence extent to which the near-field probes the sub-surface.

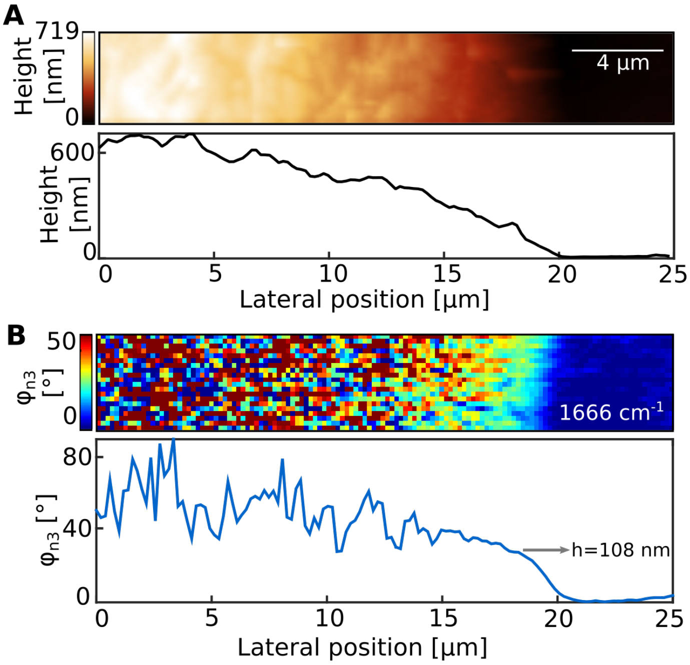

FIGURE 4.4: sSNOM imaging of stacked PM layers
**A** AFM topography of a PM sample with gradually increasing thickness and height profile across the image. **B** sSNOM phase image at 1666 cm$^{-1}$ and corresponding line profile. Both line profiles represent line-by-line average of the shown images.

## 4.2 Plasmonic structures

sSNOM imaging offers the possibility to map the near-field distribution across the surface of resonant structures and in-situ monitor the excitation of localized surface plasmons upon irradiation with IR electromagnetic-field [135]. Additionally, the near-field signal can be enhanced by using plasmonic structures with field that can couple to molecular vibrations [136, 142]. In the following, the local plasmonic field of Au disk antenna arrays, will be imaged using sSNOM. The bandwidth and enhancement properties of these structures was previously investigated using surface-enhanced IR absorption spectroscopy (SEIRAS) [152]. Subsequently, PM will be deposited on the antenna to investigate the possibility for enhancement of PM's near-field absorption.

### 4.2.1 sSNOM imaging of localized surface plasmons

AFM imaging of the Au structures showed thickness of 50 nm and diameter of 2 µm (Figure 4.5 a, b). Simultaneously to AFM imaging, single wavelength sSNOM amplitude and phase images were recorded in the spectral range from 1580 to 1720 $cm^{-1}$. In our sSNOM configuration, the disc antenna are excited using p-polarized incident IR light. The E-field component that excites electron oscillations coincides with the direction of the slow scanning axis, marked with red arrow in (a). Each structure in the array hosts a dipole mode, visible in the sSNOM amplitude image Figure 4.5 c. The bright regions stem from oscillation of the electron cloud along the incident field, whereas the dark regions from oscillations in the opposite direction. Near-field amplitude spectra were reconstructed from the recorded amplitude images, showing the reflectivity signature in the wavenumber region of interest. In Figure 4.5 d, spectra at three locations on the array referenced to a spot on the $CaF_2$ surface are shown. The spectra on the brightest region shows the highest amplitude (red curve). The amplitude decreases when moving away from this hot-spots towards the dark areas. On each of the shown locations, the reconstructed near-field amplitude spectra show no peaks.

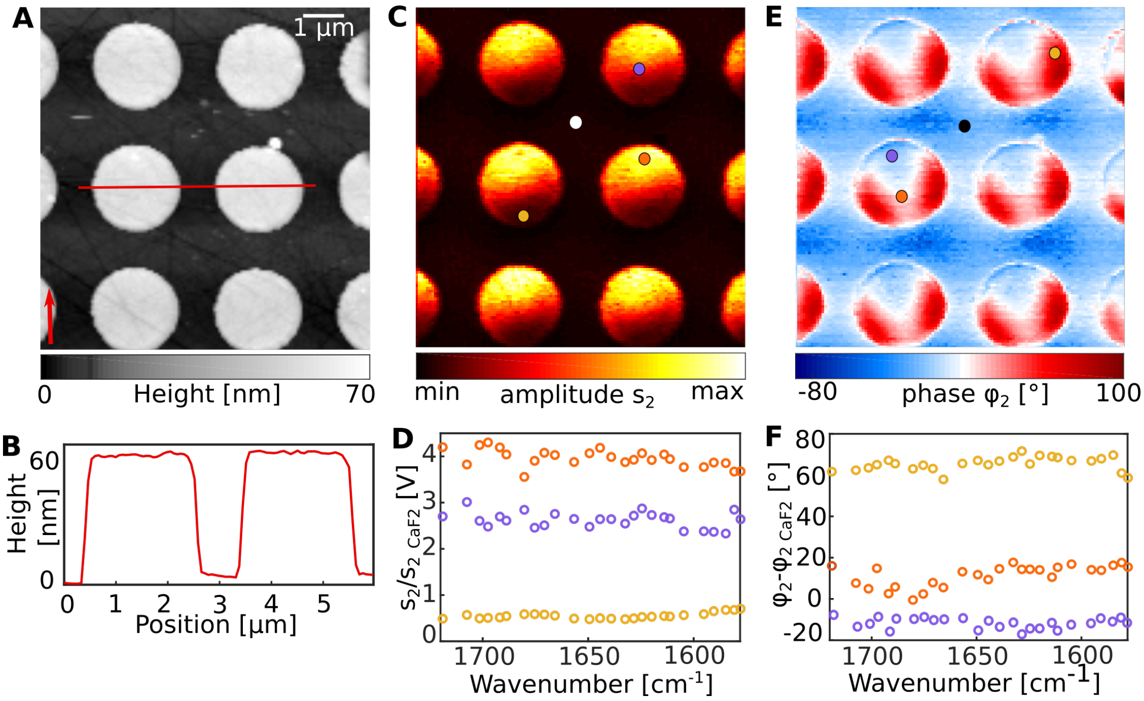

FIGURE 4.5: Near-field imaging of localized surface plasmons
**A** AFM topography and **B** height profile of Au disc antenna on $CaF_2$. The red arrow in A denotes the E-field component that excites outer electrons oscillation. **C** sSNOM amplitude at 1650 cm$^{-1}$. **D** sSNOM scattering amplitude spectra reconstructed from individual amplitude images at three locations shown in yellow, orange and blue. All three were referenced against the amplitude on $CaF_2$ (location used shown in blue circle). **E** sSNOM phase recorded at 1650 cm$^{-1}$. **F** Phase spectra reconstructed from phase images at three locations on the antenna surface (marked with purple, orange and yellow circles) referenced against the phase on $CaF_2$ (black circle).

The local phase images, corresponding to the phase of the generated E-field on the plasmonic structures in Figure 4.5 e, show areas with high (red) and low contrast (blue) with no phase difference to the $CaF_2$ substrate. In a similar fashion, a phase spectrum was reconstructed form the recorded phase image on spots with low, moderate and high contrast, referenced against the substrate Figure 4.5 f. In all cases there are no observable absorption peaks. Comparing to the far-field reflectance spectra of these structures reported in [152], the spectral window used here is within the broad resonance of the antenna. In both amplitude and phase however, no spectral signature was observed, possibly due to the narrow probing bandwidth which is limited by the emission of the used QCL. To fully access the near-field response of these structures, measurements covering the complete antenna resonance peak are necessary.

### 4.2.2 Plasmonic structures for sSNOM signal enhancement

PM patches were dried on the antenna surface following the protocol previously described in Chapter 3.6. Several membranes are visible on the AFM topography image (Figure 4.6 a). Five locations were selected to investigate the local absorption of PM (Figure 4.6 b). In all spectra the vibrational band at 1666 $cm^{-1}$ corresponding to amide I was observed. The locations coinciding with high reflectance in the amplitude image $s_2$ show the highest absorption (marked in red, yellow and purple). The spectra measured on rather high phase antenna contrast areas don't lead to increased peak intensity, but rather to an overall phase offset (marked in blue and green). The maximum absorption intensity is in the order of 20°. The elevated absorption observed on the hot-spots can be attributed to the enhancing effect of the

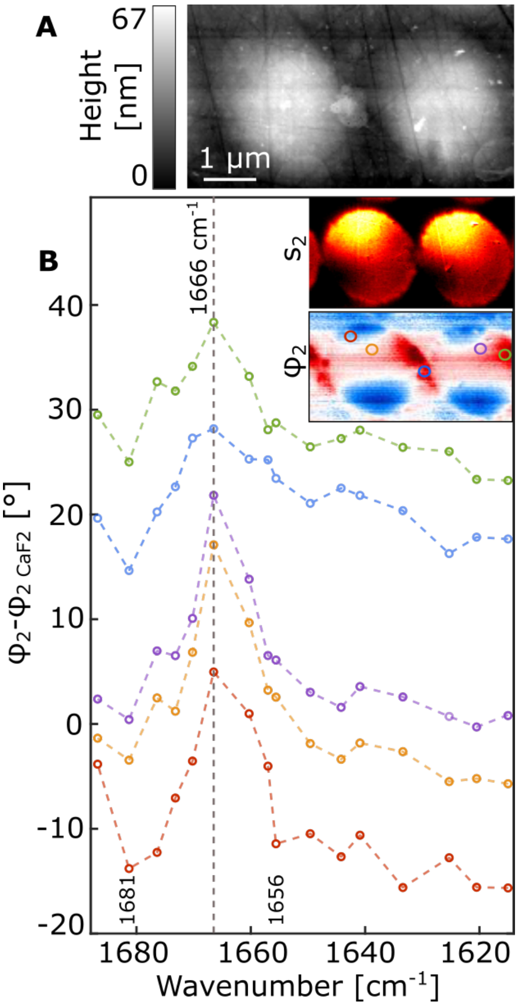

FIGURE 4.6: PM on resonant antenna **A** AFM topography of antenna covered with PM patches. **B** sSNOM phase spectra reconstructed from 16 images. Insert: amplitude and phase at 1657 $cm^{-1}$.

plasmonic field. However, in comparison with the sSNOM phase amplitude of PM on flat Au which resulted in absorption of $\sim 10^\circ$ for single layer and up to $\sim 25^\circ$ for thicknesses corresponding to three layers (Figure 4.3), the antenna-enhanced signal increased, at best, only by a factor of 2. This rather low enhancement can be attributed to the nature of coupling of plasmonic fields to molecular vibrations. The bandwidth of the amide I peak reconstructed phase spectrum in (b) spans 25 wavenumbers. Additionally, the antenna resonance as observed from the far-field reflectance spectrum, spans a broad range in the midIR. The interaction of the molecular and antenna resonance is characterized as weak coupling and therefore result in low enhancement. A previous study [142] reported weak coupling of protein vibrations with rod antenna due to the broad protein absorption band. Conversely, strong coupling can result in larger enhancement [182]. Implementing narrow bandwidth resonance structures could yield better enhancement and thus increase sSNOM sensitivity.

## 4.3 sSNOM imaging and nanoFTIR spectroscopy on stimuli-triggered aggregating peptides

Investigating the aggregation and formation of macroscopic structures from artificially designed peptides requires experiments probing their morphological properties as well as techniques able to resolve their secondary structure. Precisely the symbiosis of probe microscopy and IR spectroscopy comprised in the near-field technique used here offers the possibility to tackle this task. In addition to the sensitivity of IR spectroscopy to the secondary structure of proteins [183], sSNOM and nanoFTIR are sensitive to the orientation of the molecular vibrations. In the following a stimuli-triggered aggregating peptide (STAP1) and two mutations of the original sequence (STAP2 and STAP3) will be investigated in an attempt to elucidate the mechanism behind self-assembly and aggregation processes.

### 4.3.1 STAP1

The AFM topography of the STAP1 peptide after thermal denaturation revealed large scale fibrous structures with length in the order of micrometers and thickness of up to 100 nm (Figure 4.7 a,b). To investigate the local IR response of these structures in the amide I region, first sSNOM imaging was employed (Figure 4.7 c). The strongest absorption was observed at 1656 $cm^{-1}$ with rather homogeneous distribution across the fiber surface. An elevated absorption coincides with the thickest areas. At 1686 $cm^{-1}$ phase contrast is visible only along the outline of the structure while on the rest of the area no absorption is evident. Lower in intensity, but homogeneously distributed absorption is observed at 1650 $cm^{-1}$.

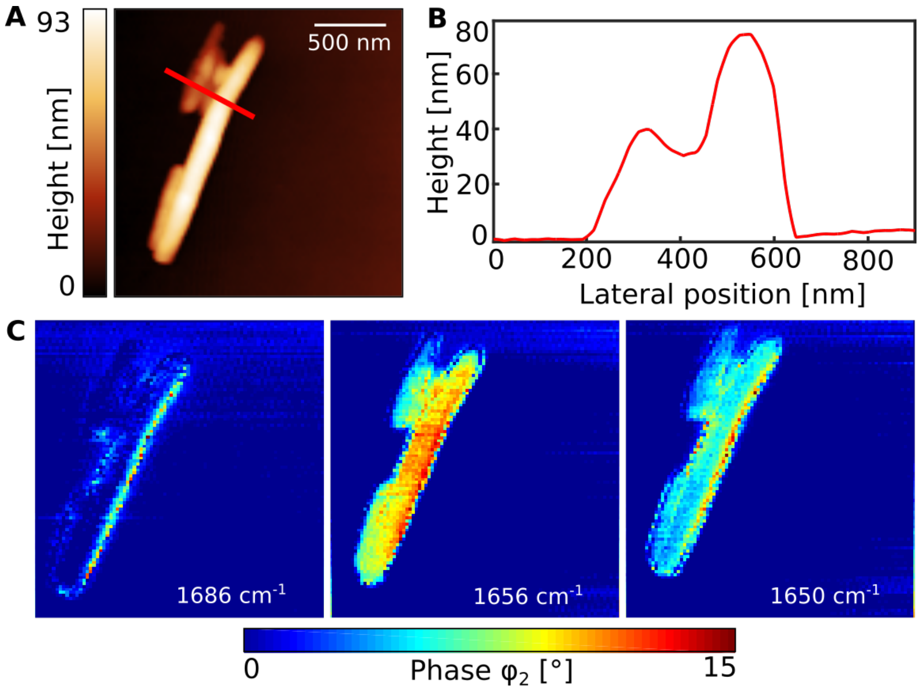

FIGURE 4.7: sSNOM imaging of STAP 1 at pH 7.4
**A**AFM topography of STAP 1. **B** Height profile across the line marked in (A). **C** sSNOM phase images at three wavenumbers covering the amide I region.

Next, nanoFTIR was employed to record spectra covering the range from 1900 to 1300 cm$^{-1}$. The AFM images on four different locations on the surface, shown in Figure 4.8 a - d, reveal macroscopic fiber structures with high aspect ratio. Their thickness is in the range of 70 to 100 nm (Figure 4.8 e) and length of several micrometers. NanoFTIR spectra was measured on each fiber (locations marked in Figure 4.8 f). Two absorption peaks with comparable intensity, assigned to amide I with maximum at 1659 cm$^{-1}$ and amide II at 1550 cm$^{-1}$, dominate all four spectra. Amide I peak position in the range 1650-1660 cm$^{-1}$ is typical for α-helical secondary structure [184, 185]. The high intensity of both amide I and amide II suggests that the helices have rather mixed orientation on the surface. The differences in the nanoFTIR absorption intensity among the four locations can be accounted for by the different thickness probed on each fiber.

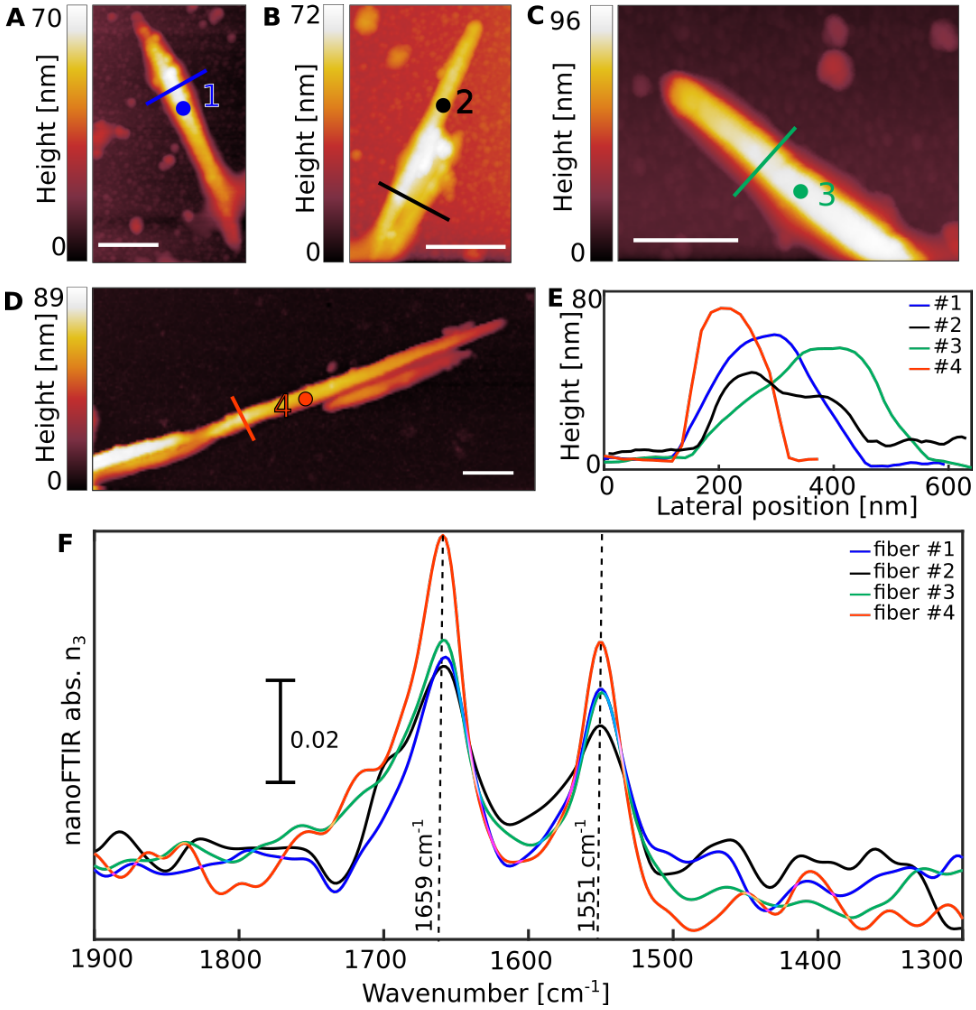

Figure 4.8: AFM imging and nanoFTIR spectroscopy of STAP1 at pH 7.4

**A-D** AFM topography images of various aggregated peptides at pH 7.4. **E** Height profiles measured across the lines marked in the AFM topographies. **F** nanoFTIR spectra of four fibrilar structures measured on the locations marked with circles in (A-D).

STAP1 peptide initially had α-helical secondary structure and formed amorphous structures, reported in [162]. The presented AFM and nanoFTIR data show that after thermal denaturation the peptides assembled into a highly ordered rod-like structures while preserving the α-helical secondary structure. A proposed explanation is that by heating the additionally supplied thermal energy is utilized to achieve high orientation [186].

Under acidic conditions (pH=3.4) spontaneous self-assembly into macroscopic structures was observed, however with flatter appearance compared to the rod-like shapes observed at neutral pH values. The AFM topography images show elongated morphology with varying thicknesses between 20 and 70 nm Figure 4.9 a-d. The edges of these structures are not sharp and widths spanning several hundred nm are evident from the topography line profiles (Figure 4.9 e).

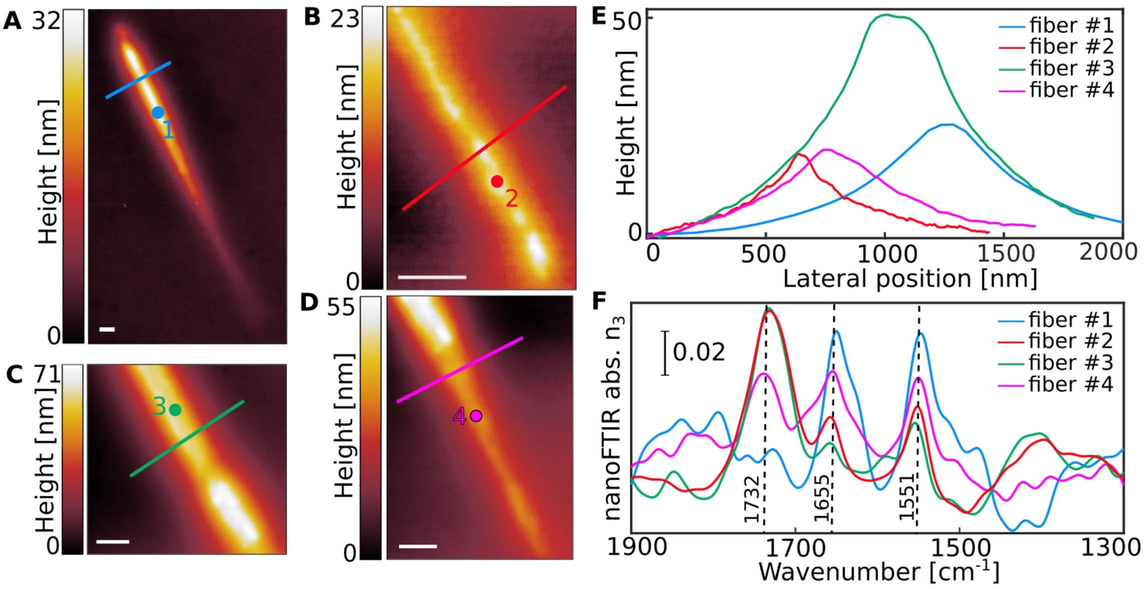

FIGURE 4.9: AFM imaging and nanoFTIR spectroscopy of STAP1 at pH 3.4 **A-D** AFM topography of STAP1 aggregates in acidic conditions. **E** Height profiles of the peptides along the marked lines in A-D. **F** nanoFTIR spectra of each peptide on the spot marked on A-D.

Near-field absorption spectra recorded on four different structures are shown in Figure 4.9 f. Fiber #1 shows amide I and amide II absorption at 1655 cm$^{-1}$ and 1551 cm$^{-1}$ respectively, which is well in line with the spectra observed on the structures at neutral pH. The amide I band position suggests α-helical structure. Strong amide II band implies that a component of the amide II vibration in the z-direction, perpendicular to the plane, was detected indicating that the helices have mixed orientation. In contrast, the rest of the probed structures showed an additional absorption with peak maximum at 1732 cm$^{-1}$, which originates from the sodium citrate solution used to buffer the peptides to acidic pH. This was confirmed by recording an ATR spectrum of the buffer (Supplementary Information A.1) revealing strong absorption at 1713 cm$^{-1}$ originating from C=O stretch of carbonyl groups.

The mechanism behind formation of STAP1 aggregates at acidic pH is not yet fully understood. Repulsive electrostatic interaction between lysine and glutamate is expected to result in low-ordered system and reduce aggregation. One proposal is that interaction between the Cy5 dye and the lysine side chains outweigh the repulsive interactions and thus allow for aggregates to form [162].

### 4.3.2 STAP2

Mutation of the original peptide was synthesized by exchanging three leucines with trifluorovaline (complete sequence shown in Table 3.1) to investigate how the increased hydrophobicity of fluorinated amino acids influence aggregation formation. In a similar fashion, STAP2 was first investigated at pH 7.4. The AFM topography (Figure 4.10 a) reveals structures formed after thermal denaturation, however with significantly different morphology than the high aspect ratio fibers reported for STAP1. Namely, large areas with thickness of 10-15 nm covered the surface. Near-field spectrum on a spot corresponding to 12 nm thickness shows absorption at 1661 cm$^{-1}$ and 1549 cm$^{-1}$ (Figure 4.10 b). From the spectral position of the amide I absorption, it can be concluded that the secondary structure is still predominantly $\alpha$-helical and from the comparable amide I to amide II ratio, that the helices do not have a preferred orientation on the surface.

The design of STAP2 was based on the premises that the hydrophobic effect increases order in self-assembly [187]. Stained transmission electron microscopy on this peptide revealed ordered striated rod structures [162], which is not consistent with the morphology observed in the AFM topography images. Possible reason for this discrepancy could be the different sample preparation approach and potential artifacts due to spin coating [188] or artifacts from the staining procedure, however additional measurements are necessary in order to elucidate this inconsistency.

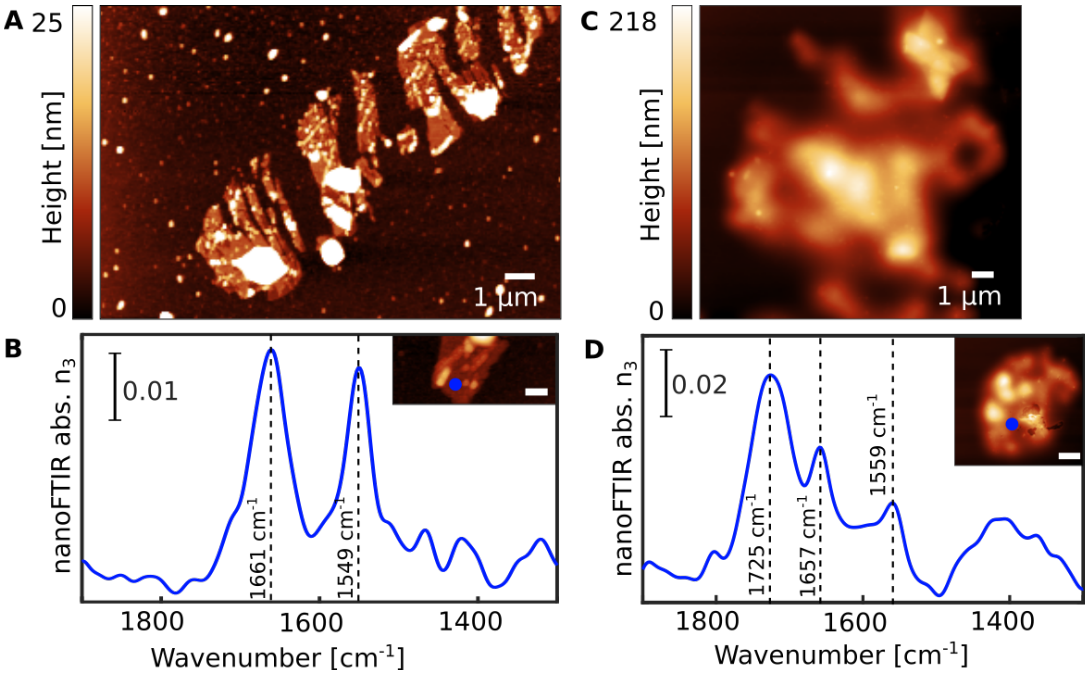

FIGURE 4.10: AFM imaging and nanoFTIR spectroscopy of STAP2 **A** AFM topography of STAP2 at pH 7.1. **B** nanoFTIR spectrum of STAP2 at pH 7.1 recorded on the marked position (blue circle) in the insert. **C** AFM topography of STAP2 aggregate formed at pH 3.4. **D** nanoFTIR spectrum of STAP2 in acidic conditions measured on the marked position in the insert. The bar scale of both inserts equals 500nm.

At pH 3.4, there were no well defined structures observable (Figure 4.10 c) but rather ill-formed aggregates with thickness of several hundred nm. The nano-FTIR spectrum is dominated by absorption at 1725 cm$^{-1}$ which likely originates from C=O stretching in carbonyl moieties in the citrate buffer, as previously discussed. The amide I and amide II bands observed at 1657 cm$^{-1}$ and 1559 cm$^{-1}$. Despite the different morphology, the IR response in this region is comparable to the peptide in neutral pH conditions and hints at α-helical secondary structure. The formation of aggregates showing low ordering is attributed to the acidic environment that prevents rod-like structures self assembly.

### 4.3.3 STAP3

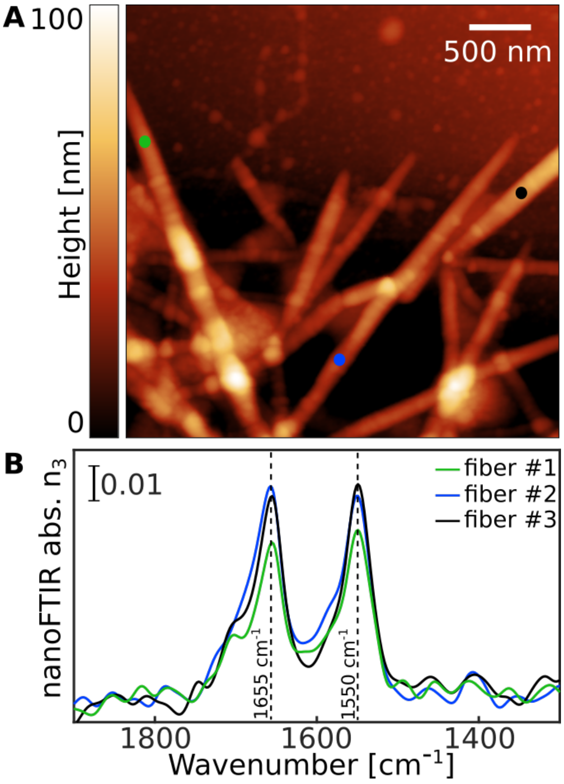

FIGURE 4.11: AFM imaging and nanoFTIR spectroscopy of STAP3 at pH 7.1
**A** AFM topography of fiber-like structures of STAP3. **B** nanoFTIR spectra measured on three different fibers marked in (A) with blue, black and green circles.

STAP3 is the second mutation where leucine was substituted with isoleucine on four locations (Table 3.1). The purpose of this exchange is to investigate the impact of a mutation with and without fluorine on aggregation behavior. Due to the similarity of isoleucine side chains with trifluorovaline, this experiment allows to single out the effects due to fluorine from potentially other mutation effects. At pH 7.1, after thermal denaturation the peptide self-assembled into fibrous structures, as shown in Figure 4.11 a. The fibers show thickness of up to 90-100 nm and length of several microns, thus highly resembling to the morphology of STAP1 aggregates at similar conditions. NanoFTIR spectroscopy was performed on three different fibers (Figure 4.11 b). Clearly distinguishable peaks stemming from peptide absorption at 1655 cm$^{-1}$ and 1550 cm$^{-1}$ correspond to the familiar amide I and amide II vibrations. In this case, the peptides have α-helical structure and no preferred orientation on the surface.

TEM imaging was performed on this peptide revealing ordred large-scale rods, which is well in line with the observation from AFM imaging. Comparison to STAP2 however proves to be difficult due to the discrepancy between the TEM and AFM images, as discussed in 4.3.2.

At pH 3.4, STAP3 failed to form high aspect ratio rod-like structures. AFM imaging (Figure 4.12 a,b) reveals that the spontaneously formed aggregates are large area, membrane-like structures with thickness of 6 to 8 nm were observed on the surface. As previously discussed, low pH environment acts rather unfavorably to large-scale ordering. Additionally, the recorded area does not have a homogeneous topography, but rather reveals various thicker areas, as well elongated fiber-like structure on one instance with thickness of ∼ 15 nm (line profile marked with red).

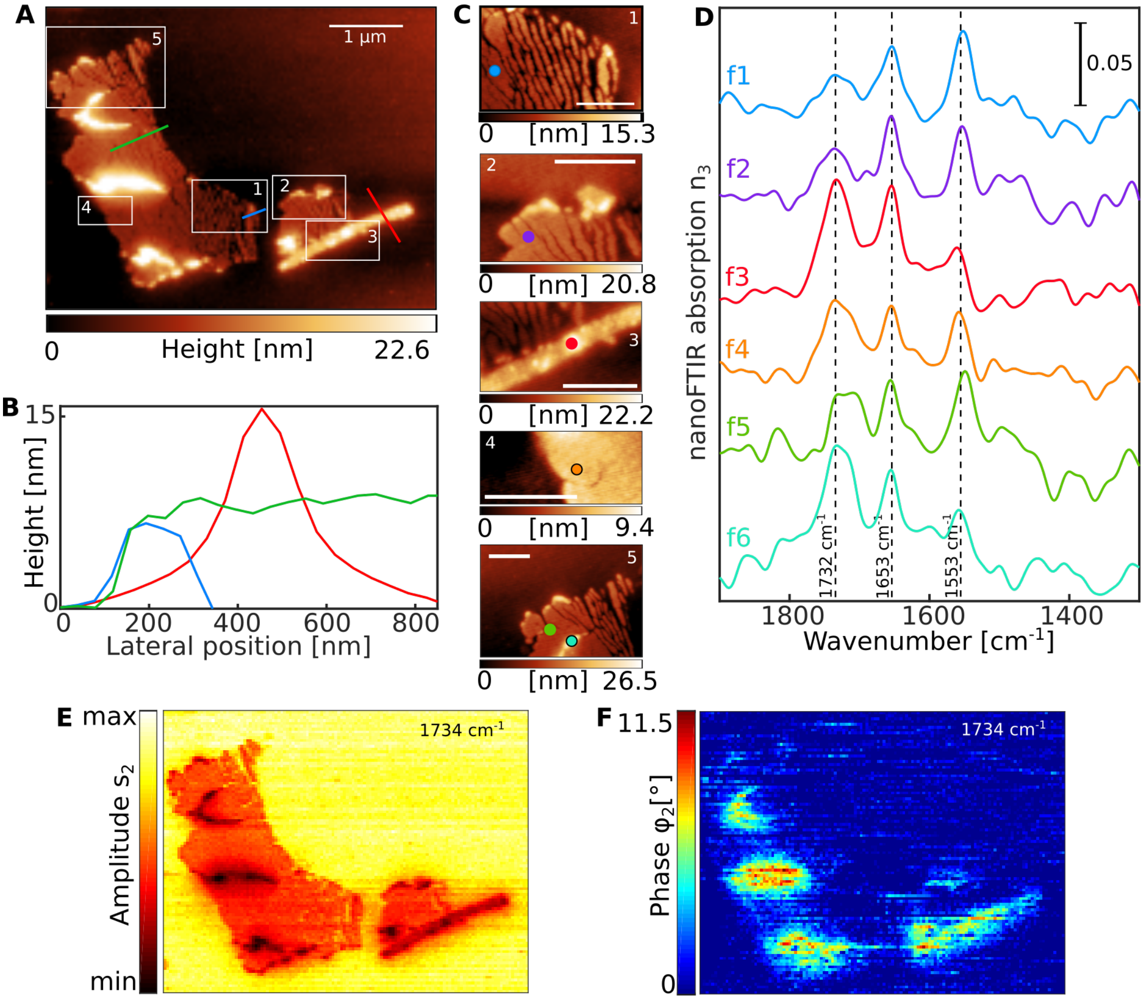

FIGURE 4.12: Imaging and spectroscopy of STAP3 at pH 3.4
**A** AFM topography of STAP3 structure formed under acidic conditions. **B** Height profiles along three lines drawn in (A), in green, blue and red. **C** Zoomed-in AFM topography images of five regions marked in (A) with white rectangles. Scale bars equal 500 nm **D** Six nanoFTIR spectra, each recorded on a single spot marked on the images in (C). **E** sSNOM amplitude and **F** sSNOM phase at 1734 cm$^{-1}$ of the structure shown in (A).

Several locations of interest, with topographies of the selected areas shown in Figure 4.12 c, were further investigated by recording nanoFTIR spectra (Figure 4.12 d). The spectrum f1, measured on a membrane-like area with thickness of ∼6 nm, shows a characteristic amide I and amide II absorption. From the spectrum it can be deduced that this thin membrane consits of peptides with α-helical structure which have mixed orientation on the surface. Additionally, a weaker in intensity peak can be observed at 1732 cm$^{-1}$. The second spectrum (f2) measured on a different membrane area but with comparable morphology, showed very similar features to f1. The spectrum on the elongated, fiber-like aggregate (f3) revealed a strong absorption at 1732 cm$^{-1}$, in addition to the protein vibrations. Interestingly, this peak was also observed in the spectra f4 and f5, measured on a membrane-like area, with intensity comparable to the amide I and amide II absorption. Moreover, in the spectrum f6, recorded on aggregate location with thickness of ∼ 20 nm, the peak at 1732 cm$^{-1}$ is even exceeding the intensity of the protein vibrations. Obviously, the absorption assigned to carbonyl C=O stretch varies across the area of this peptide structure. In order to spatially resolve this absorption, a sSNOM image was recorded at 1734 cm$^{-1}$. In the amplitude image (Figure 4.12 e), low contrast coincides with the areas covered by STAP3, with minimum reflectivity at the thickest locations. The phase image, representing the local absorption, reveals heterogeneous contrast. The areas with the highest phase contrast are indeed the locations at and around which the irregular structures were visible in the topography and match the observation from the near-field spectra. Reason for this isolated absorption features could therefore be elevated buffer concentrations in part of the aggregates.

| **Peptide** | **pH** | **Conditions** | **Morphology** | **Secondary structure** |
|---|---|---|---|---|
| STAP1 | 7.4 | upon thermal denaturation | rod-like | $\alpha$-helix, any orientation |
| STAP1 | 3.4 | spontaneous | flat elongated | $\alpha$-helix, any orientation |
| STAP2 | 7.1 | upon thermal denaturation | thin large-area | $\alpha$-helix, any orientation |
| STAP2 | 3.4 | spontaneous | ill-formed amorphous | $\alpha$-helix, any orientation |
| STAP3 | 7.1 | upon thermal denaturation | rod-like | $\alpha$-helix, any orientation |
| STAP3 | 3.4 | spontaneous | thin large-area | $\alpha$-helix, any orientation |

Table 4.1: Peptides aggregation summary

In table 4.1 a summary of the measured peptides, the structure formation conditions, the observed morphology via AFM imaging and the secondary structure deduced from nanoFTIR spectra is given. The general trend indicates that acidic conditions tend to prevent form large scale striated rods formation, with the exception of STAP2 (cell marked with red), where a rather thin and large-area structure was observed. As previously discussed in Chapter 4.3.2, additional measurements testing different sample preparation technique is necessary to elucidate the observed discrepancy.

## 4.4 Near-field spectroscopic characterization of surface relief gratings (SRGs)

Large variety of external stimuli can induce physical and chemical response in soft matter. To observe and characterize the manifestation of such responses, a technique able to resolve topography and chemical composition is necessary. In the following, light induced morphological changes and surface patterning of polymer brushes loaded with light sensitive surfactant will be investigated. The influence of the ionic strength of the surfactant on large scale physio-chemical response will be addressed by studying two polymer-surfactant complexes, namely PMAA-azo and PSPMK-azo-nitro complex.

Parts of this work have been published in: *Kopyshev, A.,* ***Kanevche, K.****, Lomadze, N., Pfitzner, E., Loebner, S., Patil, R. P., Genzer, J., Heberle, J., Santer, S., Light-induced structuring of photosensitive polymer brushes, ACS Applied Polymer Matterials (2019).* I performed the near-field spectroscopic experiments, contributed to the data interpretation and writing the manuscript.

### 4.4.1 PMMA-azo complex SRGs

The surface topography image of PMAA-azo surfactant complex prior to illumination with UV-interference pattern is shown in Figure 4.13 a and topography on an additional area in Figure A.2 with no evident pattern. The height difference between layers corresponds to the surface roughness. Three nanoFTIR spectra were recorded on the marked locations in Figure 4.13 a using spectrum on bare Si as a reference. All three measurements show very similar absorption features (Figure 4.13 b) indicating identical chemical composition. Several absorption bands are evident that stem either from the PMAA polymer brush or the azo-benzene surfactant. Absorption in the region 1732 - 1686 cm$^{-1}$ originates from C=O stretching vibrations in PMAA [189]. A high in intensity absorption at around 1600 cm$^{-1}$ is assigned to aromatic C=C stretch from the azo-benzene molecules in the surfactant [190].

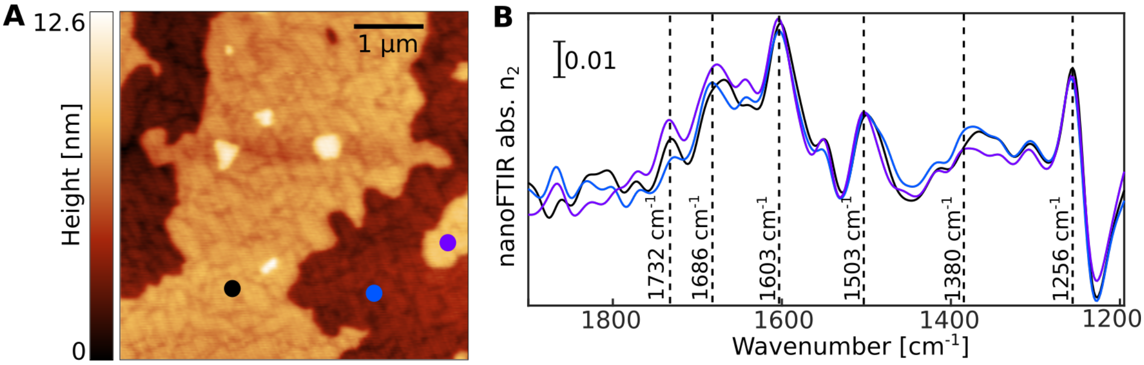

FIGURE 4.13: AFM imaging and nanoFTIR spectroscopy of photosensitive polymer brush PMAA
**A** AFM topography of PMAA treated with azo-benzene containing surfactant. **B** nanoFTIR spectra on three locations marked with black, blue and purple circles in (A). All three spectra were referenced against spectrum measured on bare Si.

The absorption at around 1500 cm$^{-1}$ originates from asymmetric $CH_3$ bending in PMAA. Absorption of the symmetric $CH_3$ bending is expected at 1390 cm$^{-1}$. On the other hand, N=N stretching absorbs at around 1380 cm$^{-1}$ and therefore the observed absorption in this wavenumber region results likely from an overlap of both vibrations originating from the brush and surfactant.

| **Wavenumber [cm$^{-1}$]** | **Vibration** | **Origin** |
|---|---|---|
| 1732 - 1686 | C=O stretching | PMAA |
| 1601 | C=C aromatic | azo surfactant |
| 1500 | $CH_3$ assym. bending | PMAA |
| 1440-1490 | CH2 scissoring | PMMA |
| 1395 - 1380 | N=N stretching | azo surfactant |
| | $CH_3$ sym. bending | PMAA |
| 1256 | C-C-O stretching | PMAA |

TABLE 4.2: Peak assignment of PMAA - Azo complex.

Absorption of C-C-O stretching in PMAA is observed at 1256 cm$^{-1}$. Peak assignment for this brush-surfactant blend is given in Table 4.1, supported by [189] and [191]. In addition, a negative feature is observed at around 1230 cm$^{-1}$, assigned to Si-O asymmetric stretch [192, 193]. This band appears negative in the spectra shown in Figure 4.13 b because Si was used as a reference.

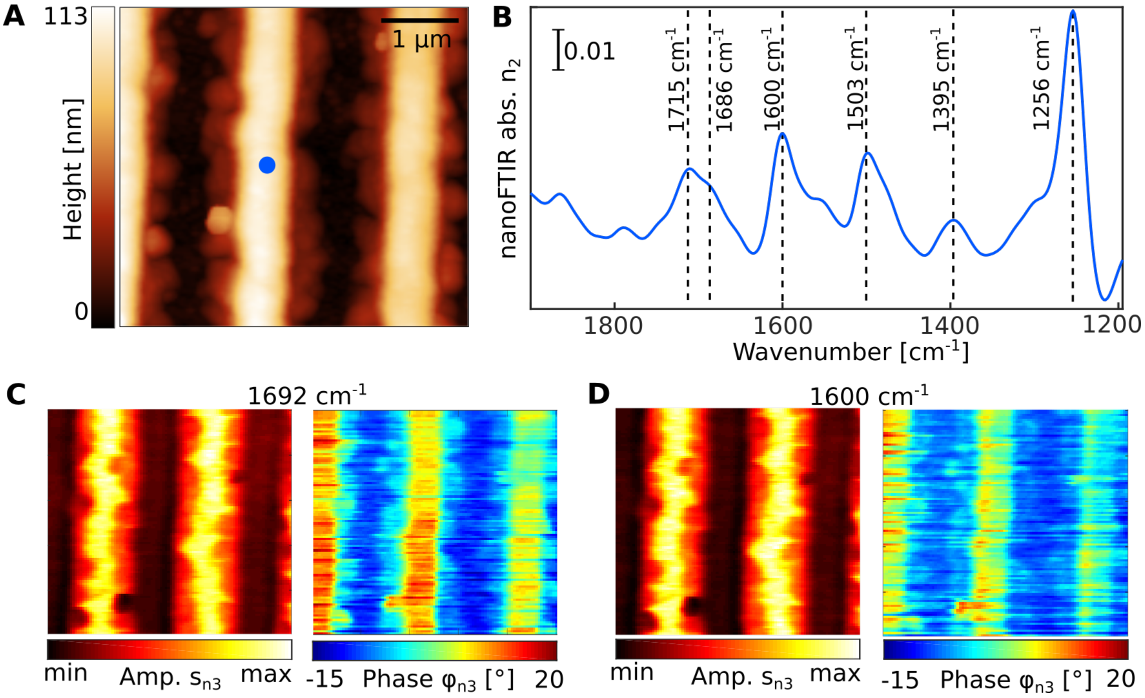

FIGURE 4.14: Imaging and spectroscopy of PMAA-azo surfactant SRGs
**A** AFM topography of PMAA-azo surfactant complex grating pattern formed upon illumination with interference pattern. **B** nanoFTIR spectrum on the position marked with blue circle in (A). **C** sSNOM amplitude and phase images recorded at 1692 cm$^{-1}$ and **D** at 1600 cm$^{-1}$. The near-field signal was demodulated at n=3.

After illumination with UV-interference pattern, thus sinusoidally varying the irradiation intensity, large scale morphology changes resulting in surface relief gratings (SRGs) are formed (Figure 4.14 a). SRG depth of $\sim$ 100 nm and height minima revealing the bare Si surface are observed, as previously reported in [168]. NanoFTIR spectrum on one of the height maxima (Figure 4.14 b) shows multitude of absorption peaks that are characteristic for the PMAA brush and the surfactant (Table 4.1). This implies that the chemical composition of the SRGs was not altered and the azo-containing surfactant is still present in the polymer brush film. sSNOM imaging at 1692 cm$^{-1}$ (Figure 4.14 c), probing the C=O stretch of esters in the PMAA brush, and 1600 cm$^{-1}$ (Figure 4.14 d) probing the aromatic C=C stretch in the azo-surfactant was performed.

The scattering amplitude giving information on the surface reflectivity, showed high contrast on the areas with low height, with a maximum on the bare Si substrate thus confirming that upon inducing large mechanical stress a polymer chain rupture and removal from the substrate is observed. Furthermore, this implies that the surfactant molecules penetrated the complete thickness of the PMAA brush. The phase contrast at both wavenumbers revealed absorption on the areas with elevated height, which is in agreement with the nanoFTIR spectroscopy outcome.

The mechanism behind the observed large-scale surface patterning is based on photo-isomerization of the azo-benzene moieties in the brush-surfactant complex [194]. Namely, upon illumination with UV radiation, azo-benzene undergoes isomerization from trans to cis configuration [195] resulting in small scale motion of the surfactant molecules. This process initiates collective alignment of the surfactant molecules perpendicular to the polarization of the incident radiation [196] and subsequently induce reorientation of the polymer brushes. Large opto-mechanical stress is formed in the polymer brushes which leads to macroscopic deformation [197] and even removing of the polymer chains from the substrate [198]. Such polymer chain scission was observed in the PMAA brush, a weak polyelectrolyte [199], due to the ability of the surfactant molecules to penetrate deep into the polymer layer .

### 4.4.2 PSPMK azo nitro complex

In contrast to the SRGs presented in Chapter 4.4.1 utilizing weak PE brush, here the strong PE brush PSPMK loaded with azo-nitro surfactant will be investigated. AFM topography shows the surface of the polymer brush (Figure 4.15 a) and the brush-complex (Figure 4.15 a) with comparable roughness. NanoFTIR spectroscopy was employed to characterize PSPMK and PSPMK-azo nitro complex (Figure 4.15 c). The polymer spectrum is dominated by two peaks at 1730 cm$^{-1}$, assigned to C=O stretch vibration, and at 1190 cm$^{-1}$ typical for $SO_3$ stretching, with a shoulder at 1246 cm$^{-1}$ assigned to C-O stretch in ester groups [200]. The spectrum after treatment with azo-nitro surfactant reveals several additional absorption bands. Aromatic C=C stretching in azo benzene absorbs at 1601 cm$^{-1}$ [190]. The asymmetric and symmetric NO stretch are observed at 1524 cm$^{-1}$ and 1346 cm$^{-1}$, respectively. The N=N stretch in azobenzene with typical absorption at around 1380 cm$^{-1}$ shows quite low intensity peak. The band at 1256 cm$^{-1}$ is assigned to C-O stretch. Assignment of the most prominent absorption bands is summarized in Table 4.2.

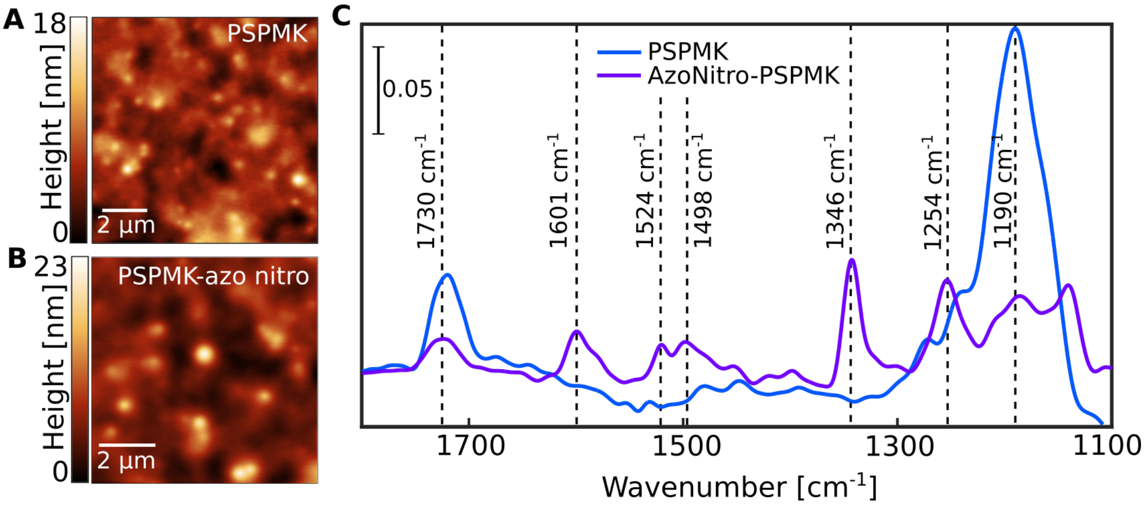

FIGURE 4.15: AFM and nanoFTIR spectroscopy of photosensitive polymer brush PSPMK

**A** AFM topography of PSPMK and **B** of PSPMK after treatment with azo-nitro surfactant. **C** nanoFTIR spectra measured on the polymer brush (blue curve) and of the polymer-surfactant complex (purple curve). Figure adapted from [169].

Negative features at around 1230 and 1120 cm$^{-1}$ are assigned to asymmetric and symmetric Si-O stretch, respectively [192, 193].

NanoFTIR spectroscopy can thus confirm that the polymer was rendered photosensitive after treatment with the surfactant. After illumination with interference pattern for 15 min (18 J/cm$^2$), 20 min (24 J/cm$^2$) and 30 min (36 J/cm$^2$) large scale SRGs with periodicity of 1.9 µm were formed (Figure 4.16 a). The depth of the gratings was found to be around 80 nm for 18 J/cm$^2$, and decreased with increasing irradiation time to 57 and 25 nm for 24 J/cm$^2$ and 36 J/cm$^2$ respectively. NanoFTIR spectra recorded on the grating with lowest exposure time reveals the absorption bands characteristic for the polymer brush and surfactant (Figure 4.16 b) indicating that this grating is still photo-active after the illumination. Moreover, spectrally there is no difference between the grating's minima and maxima (measured locations marked in Figure 4.16 c), besides higher intensity of several bands measured on a grating maximum (blue curve) due to larger thickness. The AFM topography of an area including a scratch on the surface shows that the polymer total height is $\sim$ 120 nm. This means that the polymer chains didn't rupture down to the bare Si surface, but instead there is a layer of approximately 40 nm that didn't respond to the applied illumination.

| **Wavenumber [cm$^{-1}$]** | **Vibration** | **Origin** |
|---|---|---|
| 1730 | C=O stretching | PSPMK |
| 1601 | C=C aromatic | azo-nitro surfactant |
| 1524 | NO assym. bending | azo-nitro surfactant |
| 1498 | $CH_2$ stretching | azo-nitro surfactant |
| 1346 | NO sym. stretching | azo-nitro surfactant |
| 1254 | C-O stretch | PSPMK & azo-nitro surfactant |
| 1190 | $SO_3$ stretching | PSPMK |

TABLE 4.3: Peak assignment of PSPMK brush and azo-nitro surfactant.

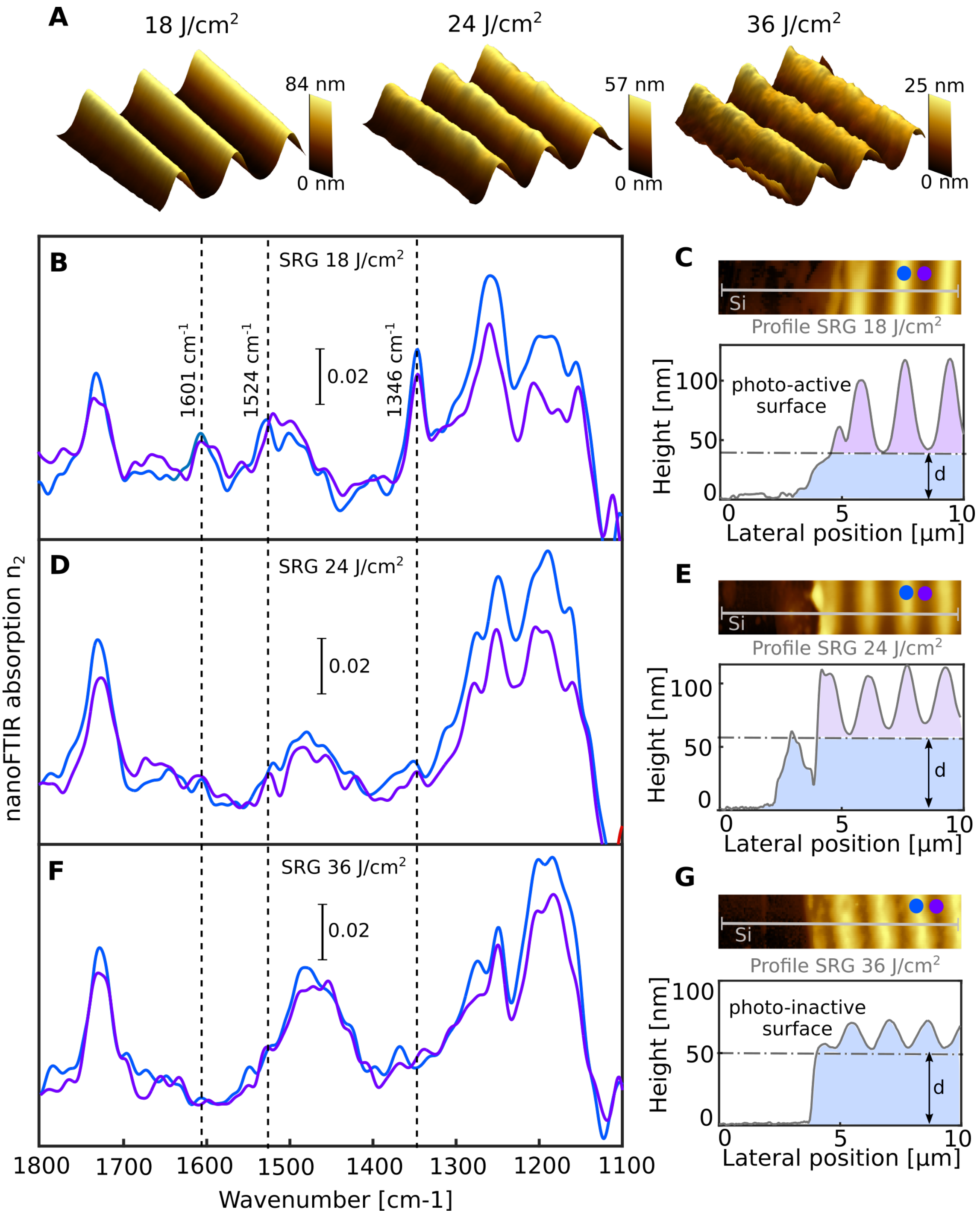

FIGURE 4.16: AFM imaging and nanoFTIR spectroscopy on surface patterned PSPMK-surfactant complex

**A** Three-dimensional representation of AFM topography of SRGs formed upon illumination with increasing power densities. **B** and **C** nanoFTIR spectra recorded on a minimum (purple curve) and maximum (blue curve) and AFM topography, respectively, of photosensitive PSPMK exposed to 18 J/cm$^2$ UV radiation. **D** nanoFTIR spectra of SRGs formed upon irradiation with power density of 24 J/cm$^2$ on a minimum and maximum position. **E** Corresponding AFM topography and line profile. **F** and **G** nanoFTIR spectra and AFM topography of the surface pattern formed after exposure at 36 J/cm$^2$, respectively.

Spectra measured on a minimum and maximum spot of the SRGs exposed to 24 J/cm$^2$ are shown in Figure 4.16 d. A significant decrease in the absorption intensity of the surfactant marker bands (1601 cm$^{-1}$, 1524 cm$^{-1}$ and 1346 cm$^{-1}$) is evident. The spectrum on a maximum of the SRG shows overall higher intensity due to the elevated thickness at this location. AFM topography and the corresponding height profile (Figure 4.16 e) show total thickness of $\sim$ 110 nm and a 60 nm layer underneath the grating. In a similar fashion, the SRG formed upon the longest exposure time was investigated (Figure 4.16 f, g). In this case, no absorption from the azo-nitro surfactant was observed, meaning that the surface is no longer photosensitive. The thickness of the layer was found to be $\sim$ 70 nm with an approximately 50 nm layer without evident morphological changes. In all three gratings however, the sinusoidal shape was induced only down to a limited thickness, thus leaving a layer that was not affected by the illumination. This likely occurs due to the limited penetration depth of the surfactant in the densely grafted polymer brush.

In order to further investigate the surface response mechanism, light sensitive PSPMK brush was illuminated in multiple steps. After a two-step illumination with interference pattern (the second being 90° tilted with respect to the first) a grating following the light intensity modulation is formed (Figure 4.17 a) with height difference between the minima and maxima of 50 nm. Near-field spectrum was recorded on both a maximum and minimum position (Figure 4.17 b). In both cases, absorption peaks assigned to the polymer PSPMK and the azo-nitro surfactant are observed, which supports the hypothesis that this particular surfactant does not penetrate the full depth of the brush surface. The spectra recorded on a maxima shows a overall higher intensity due to the larger thickness. Three-step irradiation, the third being at 45° with respect to the first, yields the surface pattern shown in Figure 4.17 c. The spectra on a minimum and maximum location of the pattern (Figure 4.17 d) are very comparable, thus the polymers do not rupture to the bare Si surface due to limited surfactant penetration.

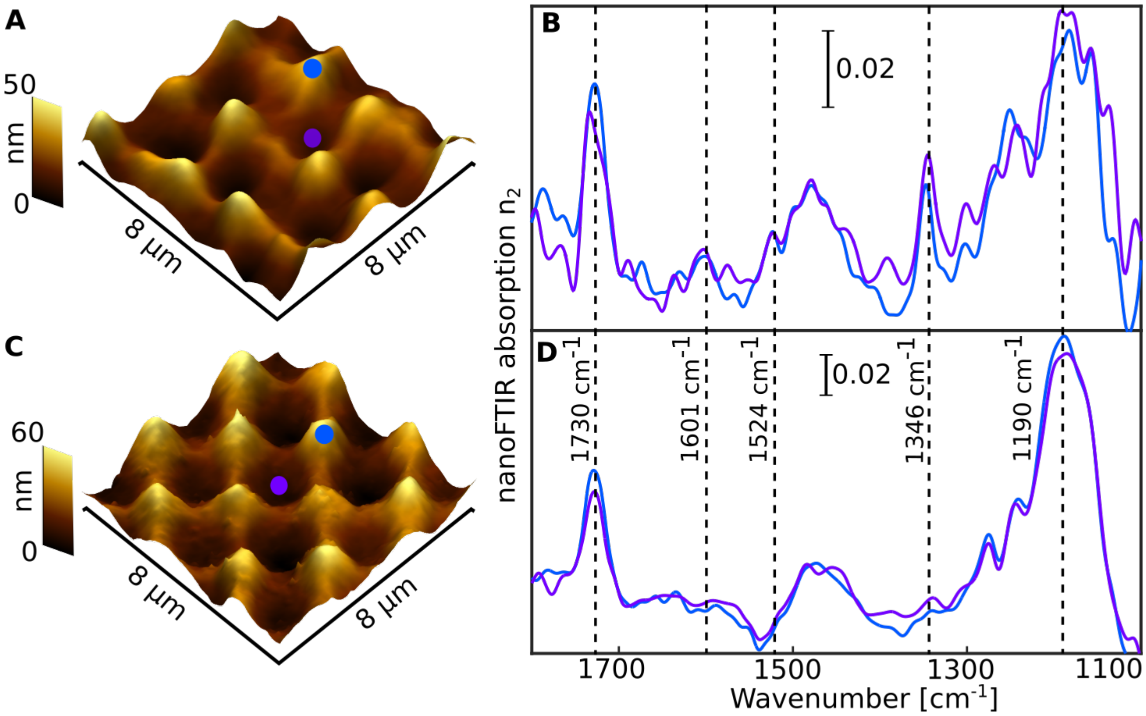

FIGURE 4.17: AFM imaging and nanoFTIR spectroscopy of SRGs after multiple illuminations

**A** Topography of a SRG formed after two-step illumination. **B** nanoFTIR spectra on a minima (purple) and maxima (blue) location marked in (A). **C** AFM topography of PSPMK SRG after three-step illumination and **D** corresponding nanoFTIR spectra measured on a minima (purple) and maxima (blue). Figure adapted from [169].

Interestingly, the spectra is dominated by absorption form PSPMK and shows no absorption from the surfactant - similar to the long-exposure SRG shown in Figure 4.16 f, g. The spectrum recorded on a minimum shows lower absorption intensity at 1730 cm$^{-1}$, 1346 cm$^{-1}$ and 1190 cm$^{-1}$ due to the lower number of probed molecules. The mechanism behind the observed surface patterning is based on light-induced isomerization of the azobenzene moiety in the azo-nitro surfactant. Large opto-mechanical stress is generated only in the light-active volume of the polymer brush, i.e the portion that contains surfactant molecules. Due to the ability of PSPMK to completely dissociate in solution, typical for strong polyelectrolytes [201], the surfactant molecules are hindered from penetrating the full length of the polymer chains which in turn prevents from polymer chain scission [169].

## 4.5 Stable Isotope Probing SIP-nanoFTIR

Stable isotope probing (SIP) in combination with spectroscopic techniques has been used to probe the metabolic activity of bulk microbial cultures [202], as well as on a single cell level using infrared photothermal spectroscopy [203]. In the following nanoFTIR spectroscopy is first applied on *E. coli* exposed to various proportions of $^{13}$C isotope labeled glucose to establish the red shift of the major protein vibrational bands, which serves as an indicator for metabolic activity. The heterogeneity in metabolic activity of single cells was investigated using a second set of cultures, exposed to limited amount of nutrients.

### 4.5.1 $^{13}$C glucose uptake in *E. coli*

Standard *E. coli* cells, grown in media free from isotopically labeled glucose, were examined as a reference, following fixation. The AFM topography (Figure 4.18 a, b) shows the typical rod-shaped bacteria with thickness of up to 500 nm and length of 1 µm to 2 µm.

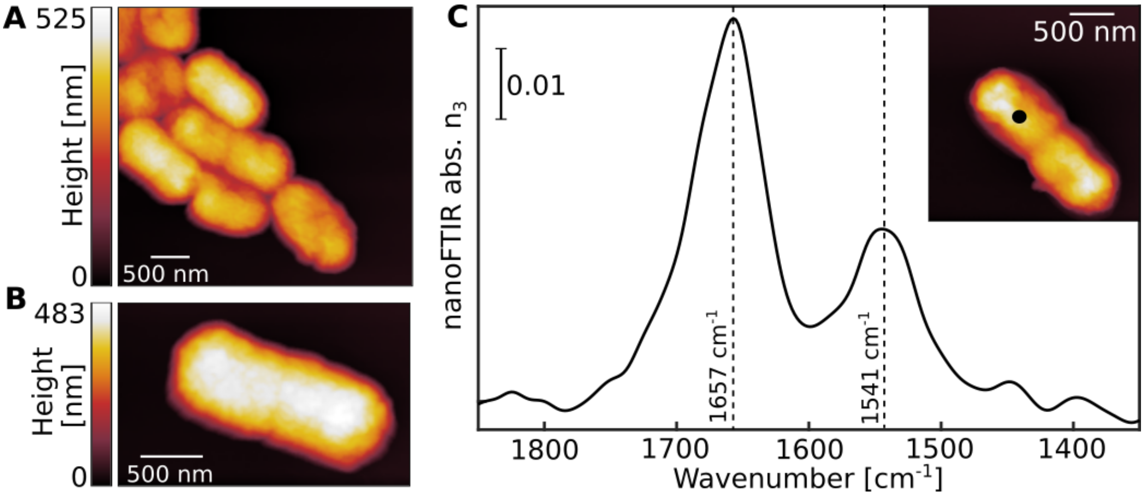

FIGURE 4.18: AFM imaging and nanoFTIR spectroscopy of *E.coli* cells
**A** and **B** AFM topography of E.coli cells. **C** nanoFTIR spectrum measured on the E. coli cell shown in the insert marked with black circle.

The nanoFTIR spectrum measured on one spot on the bacterium (Figure 4.18 c, insert) is dominated by absorption at 1657 cm$^{-1}$, due to amide I, followed by absorption at 1541 cm$^{-1}$, typical for amide II. Next, nanoFTIR spectra were recorded on single cells from each of the eleven $^{12}C/^{13}C$ proportions (Figure 4.19). Uptake of the isotope labeled glucose is manifested in shift of the protein absorption bands.

The spectra of cells grown in 0 % $^{13}C$ are highly comparable to the spectra of standard *E. coli* cells (Figure 4.18), with the amide I and amide II peaks observed at 1655 cm$^{-1}$ and 1541 cm$^{-1}$, respectively. Gradually increasing the content of $^{13}C$ glucose results in shifts to lower wavenumbers. For instance, the amide I absorption maximum for 100% $^{13}C$ glucose is positioned at 1613 cm$^{-1}$ and the amide II at 1532 cm$^{-1}$, matching with spectral shifts observed in bulk spectra [204], as well as in single cells investigated by IR photothermal spectroscopy [205]. Peak broadening of the amide I are observed for mixed proportions, evident in the spectra corresponding to 20%, 30% and 60-80% $^{13}C$, and even to double-peak features for 40% and 50% $^{13}C$.

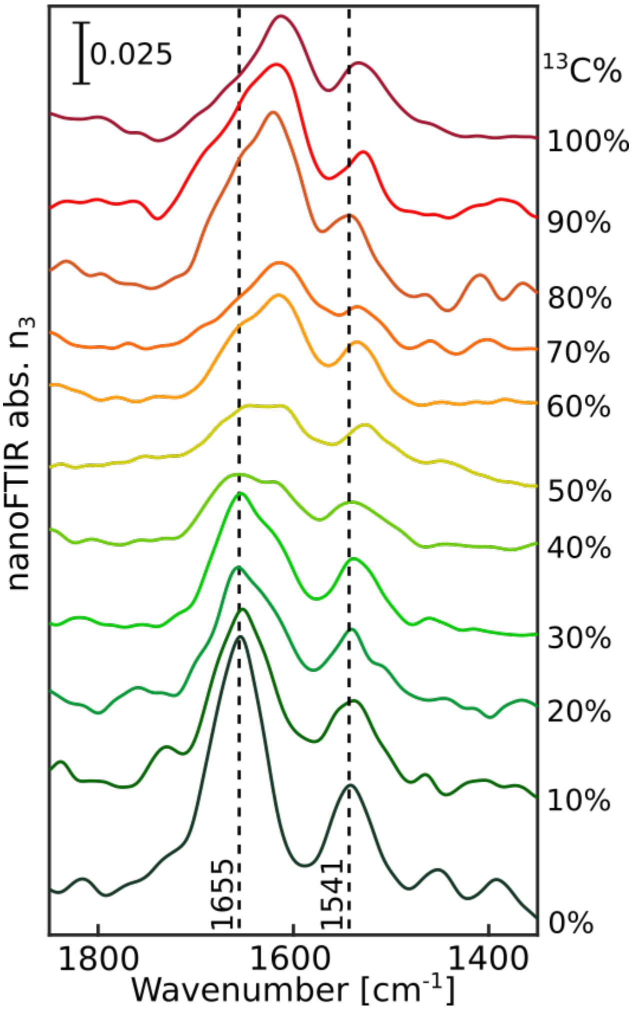

FIGURE 4.19: NanoFTIR spectra of isotope labeled *E. coli*
Each spectrum was measured on a single cell, starting with not-labeled cell and gradually increasing the content of $^{13}C$ in the glucose fed to the cells until reaching 100 % $^{13}C$.

The effect of introducing isotope labeled glucose was further investigated by applying principle component analysis (PCA) [206] on a larger data set. For that purpose, ten cells of each $^{13}$C glucose treatments were recorded, amounting to a total of 110 single-cell nanoFTIR spectra. The spectral region 1713 - 1501 cm$^{-1}$, covering the amide I and amide II bands, was considered for the analysis.

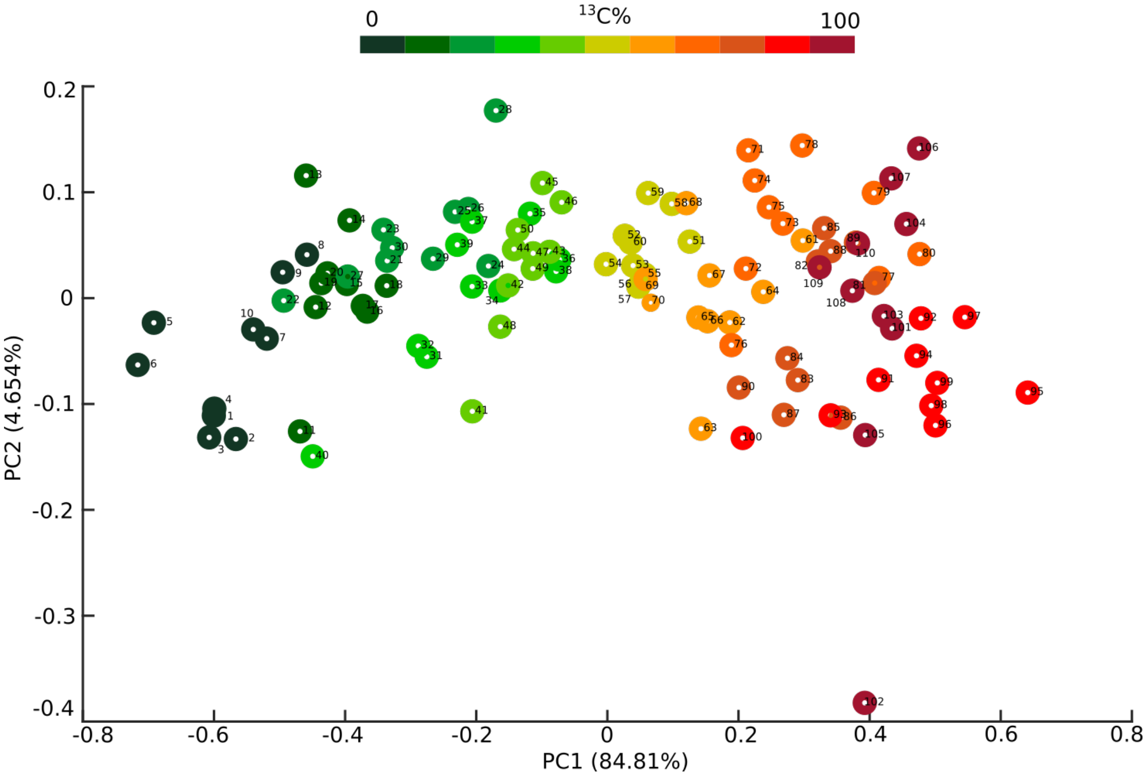

FIGURE 4.20: PCA analysis of single cell spectra
Scatter plot showing the similarity of 110 single cell spectra along the first (PC1) and second (PC2) principal component with contributions to the variation in the data set of 84.81 % and 4.654 %, respectively. Ten cells from each $^{13}$C/$^{12}$C ratios, amounting to a total of 110 single cell spectra, were used for the analysis. All individual spectra are shown in the Appendix A.3.1. Matlab PCA routine implementing single value decomposition algorithm (SVG) was used.

A score plot of the first and second principal component (Figure 4.20) reveal the largest variation along the PC1 axis. There is evident grouping of the spectra that can be accounted to the different $^{13}$C content. One exception is observed for a cell belonging to the 100% $^{13}$C glucose (#102). A closer look at this spectrum, shown in Figure A.3, last panel and Figure A.4, last panel, reveals a rather anomalous amide

II band shape, which could be the reason why this measurement point appears as an outlier. The cells corresponding to 80%, 90% and 100% show overlap in the grouping and thus high similarity. Four of the 90% cells are positioned further away from the rest of the set, which can be due to variation of the single cell glucose uptake. The loading plot of the PC1 variable (Figure A.5 a,b), shows large variation at 1660 cm$^{-1}$ and 1610 cm$^{-1}$, corresponding to the amide I absorption position in not labeled cells and 100% $^{13}$C glucose labeled cells, respectively. PC2 shows large variation at 1650 cm$^{-1}$ and 1541 cm$^{-1}$ matching to the absorption of amide I and amide II for non-labeled cells.

### 4.5.2 Metabolic heterogeneity

Single cell nanoFTIR spectroscopy was next applied to cells under carbon-limiting conditions.

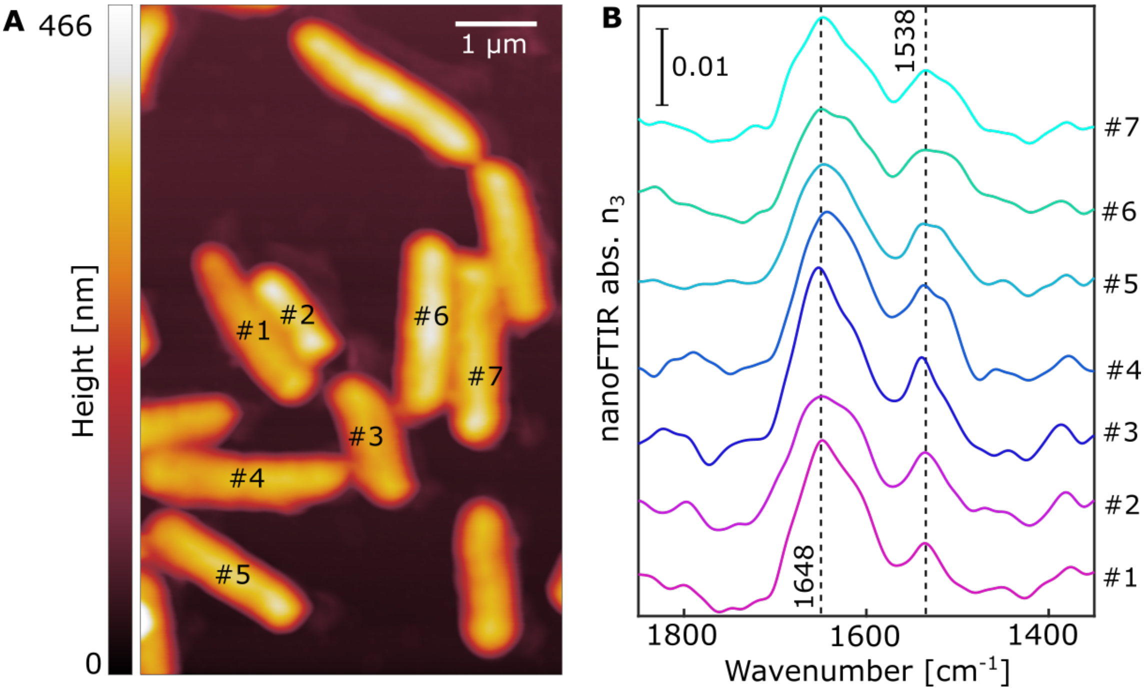

FIGURE 4.21: Detection of $^{13}$C glucose in *E. coli* cells under limited nutrients **A** AFM topography of *E. coli* exposed to low concentration (0.04g/L) of 100% $^{13}$C glucose. **B** nanoFTIR spectra on seven cells marked in (A).

As showed in the previous chapter, nanoFTIR spectroscopy is sensitive to the isotope content, thus monitoring the spectral shift in the amide I and amide II region gives direct information on the cellular metabolic activity. Seven of the cells shown in the AFM topography image (Figure 4.21 a) were investigated. The nanoFTIR spectra (Figure 4.21 b) reveal amide I and amide II absorption, centered around 1648 cm$^{-1}$ and 1538 cm$^{-1}$, respectively. Amide I peak at around 1650 cm-1 corresponds to 30% $^{13}$C, as evident from Figure 4.20, whereas rather broad peaks evolving to double peak observed in spectra # 2,#5 and #6 correspond to 40-50% $^{13}$C.

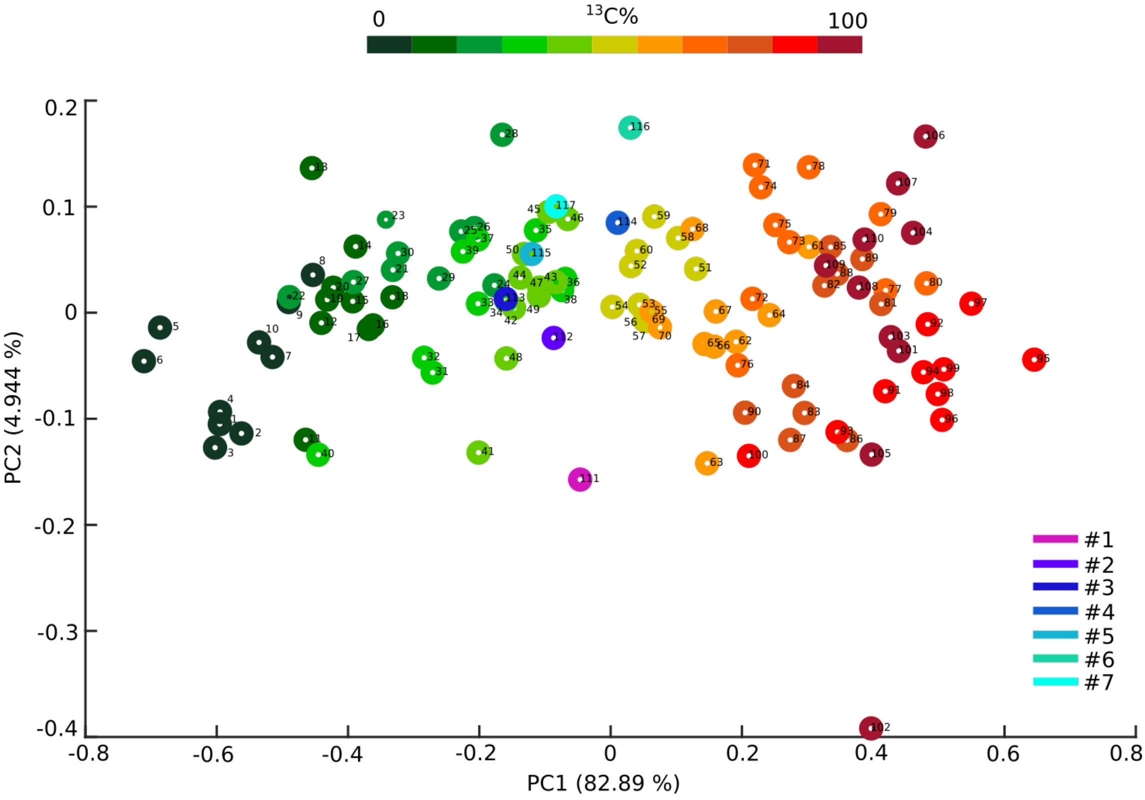

FIGURE 4.22: PCA analysis - expanded set
Seven spectra (shown in Figure 4.21), with an unknown amount of metabolized $^{13}$C labeled glucose were added to the PCA set of 110 cells (Figure 4.20). The variation of the data set along the first (PC1) and second (PC2) component representing 82.89% and 4.944% of the total variance.

Qualitative assignment of a specific spectrum to percentage of metabolized isotope-labeled glucose can be aided by applying PCA analysis. The seven spectra corresponding to samples grown under limited $^{13}$C glucose were added to the previous set of 110 cells and PCA analysis in the spectral region 1713 - 1501 $cm^{-1}$ was performed. In Figure 4.22 the first two components are visualized. The additional seven spectra are show relatively low variation along the first component and are located in the area corresponding to 30-50 % $^{13}C$. Cell #1, #2, #3, #5 and #7 are in the vicinity of 30-40 %, whereas #4 and #6 show higher $^{13}C$ content in the order of 50%. The loading plots of both variables PC1 and PC2 are very comparable to the ones from the set of 110 cells, as evident from Figure A.5 c,d.

## 4.6 Subcellular imaging and nanoscopy

NanoFTIR and sSNOM can be employed in investigation of complex biological specimens such as whole cells, however the limited penetration depth of IR nanospectroscopy and imaging prevents from investigating the cellular internal structure. An approach to circumvent this limitation is to use cell thin sections. A sample preparation method known from TEM was adapted to obtain *E. coli* and *C. rheinhardtii* sections suitable for morphological and spectroscopic study by AFM, sSNOM and nanoFTIR.

Part of this work is included in: ***Kanevche, K.***, *Burr, D., Hass, P., Nuernberg, D., Elsaesser, A., Heberle, J., Infrared nanoscopy and tomography of intracellular structures (2021) DOI:10.21203/rs.3.rs-753486/v1.* I contributed to sSNOM and nanoFTIR measurements, data evaluation, 3D reconstruction and visualization, interpretation and writing of the manuscript.

### 4.6.1 *Escherichia coli*

An overview AFM image showing several *E. coli* cells sliced in various orientations is presented in Figure 4.23 a. The horizontally oriented cells show typical length 1.5 µm while the diameter of the horizontally oriented cells is in the range of 600-800 nm and well in agreement with previously reported *E. coli* [207, 208]. The area surrounding the cells corresponds to the embedding resin. As *E. coli* is a prokaryotic organism, it does not contain membrane-bound organelles, hence the morphology observed is relatively homogeneous. Two cross-sectioned cells were selected for nanoFTIR spectroscopy (Figure 4.23 b, c). Several spectra were recorded on the cellular surface (locations marked on the topography inserts) and one spectrum on the surrounding resin with reference on TS Au. The resin spectrum (black curve) is dominated by peak at 1736 cm$^{-1}$, assigned to C=O stretching of succinic anhydride. The features in the spectral region around 1450 cm$^{-1}$ are assigned to C-H deformation of CH and $CH_2$ groups. Absorption from C-H deformation in $CH_3$ is observed at around 1350 $cm^{-1}$. Strong absorption at around 1740 $cm^{-1}$ is evident in each of the spectra measured on a cell area, hinting at resin penetration throughout the cell area. Absorption bands at 1659 $cm^{-1}$ and 1542 $cm^{-1}$, assigned to amide I and amide II originating from proteins, are observed in the spectra recorded on the cytoplasmic region. One spectrum was measured on the cell wall (Figure 4.23 c (blue curve)).The highest intensity absorption is observed at 1740 $cm^{-1}$, overlapping with the resin-characteristic band. Low intensity absorption in the amide I region likely originates from peptidoglycan in the wall typical for Gram-negative bacteria [209], [210].

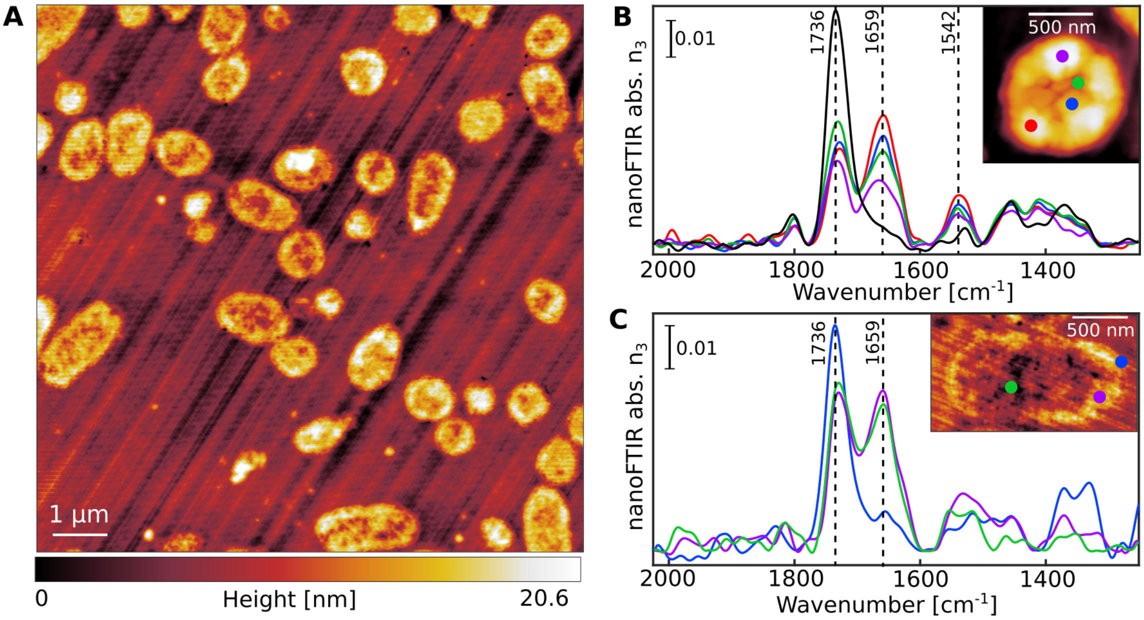

FIGURE 4.23: AFM imaging and nanoFTIR spectroscopy of *E. coli* thin sections **A** AFM topography showing an overview of *E.coli* thin sections. **B** nanoFTIR spectroscopy of a thin section (insert) vertically sliced. Four spectra were measured on the cellular surface (locations marked with circles in the insert image) and one (black curve) on the surrounding resin.**C** nanoFTIR spectra on three locations (circle marks in the insert AFM image) of a horizontally sliced cell. B and C adapted from [211].

Vibrational bands at around 1400 $cm^{-1}$ can be assigned to absorption from amide III. Additionally, the absorption features in the range at around 1400 $cm^{-1}$ and 1300 $cm^{-1}$ can be due to deformation of CH, $CH_2$ and CCO in complex sugar modes [212], stemming from peptidoglycan. However, overlap of several molecular vibrations originating from the resin and cellular components prevents more conclusive band assignment in this spectral region.

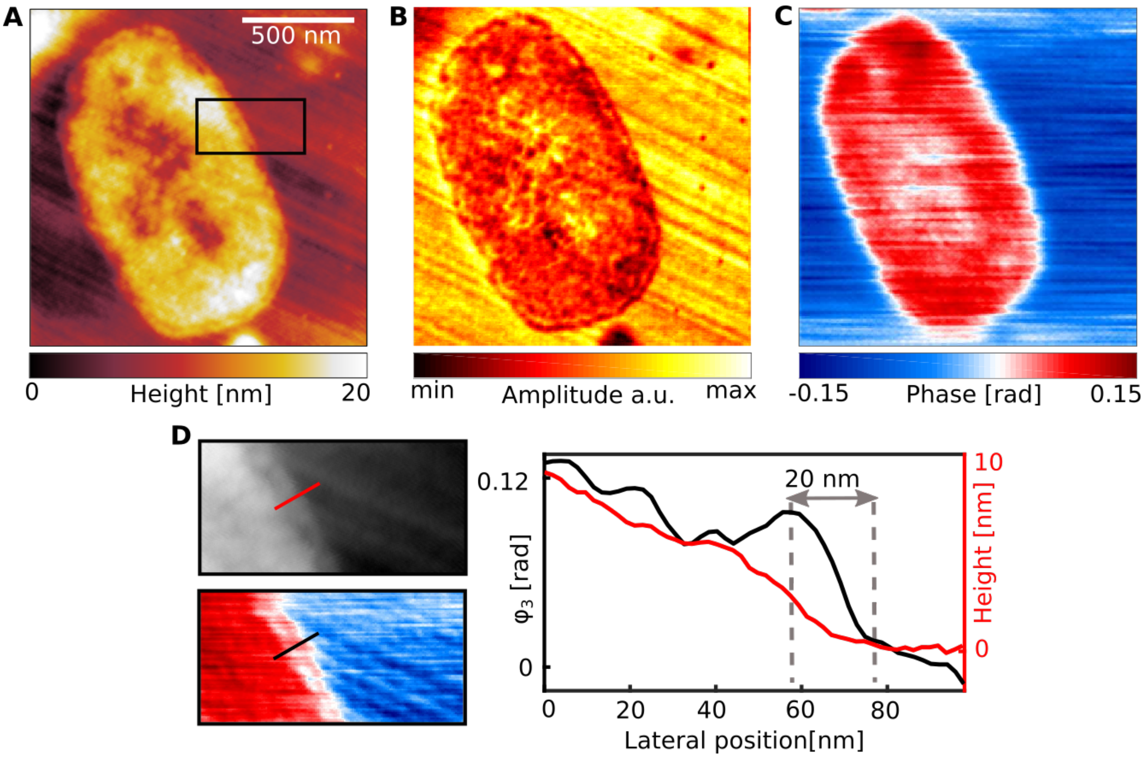

FIGURE 4.24: AFM and sSNOM imaging of *E. coli* thin sections
**A** AFM image of a single thin-section. **B** sSNOM amplitdue and **C** phase recorded at 1658 cm$^{-1}$. **D** Zoomed-in image of the region marked in (A). Phase line profile marked with black line in the image shows lateral resolution of 20 nm. Figure adapted from [211].

To inspect the local protein absorption distribution, sSNOM imaging at 1658 cm$^{-1}$ was performed. Topography of the selected cell slice is shown in Figure 4.24 a. Low sSNOM amplitude (Figure 4.24 b) is observed on the cell area and several patches in the central part with higher contrast. The diagonal stripes on the surrounding resin are knife marks resulting from the slicing procedure. The sSNOM phase representing the local protein absorption (Figure 4.24 c) shows high contrast throughout the cell area with elevated absorption on the upper end suggesting concentrated protein content. Weaker absorption is observed on the cell outer membrane and in the central part and no absorption on the resin surrounding the cell. This is in agreement with the nanoFTIR spectroscopy observations. Similarly to the AFM topography images, no well defined cellular compartments and membrane-bound organelles are observed in the sSNOM images.

### 4.6.2 *Chlammydomonas reinhardtii*

The morphology of *C. reinhardtii* thin sections was first investigated via AFM imaging. Figure 4.25 a shows an overview of resin-embedded cross sections with varying size reaching up to 8-9 µm in diameter, sectioned at different positions and orientations. Inter-cellular structures can be readily identified from the AFM topography of the largest section in the overview (Figure 4.25 b). Several typical *C. reinhardtii* features [213] include the pyrenoid surrounded by the stacked thylakoids, the nucleus and the plasma membrane.

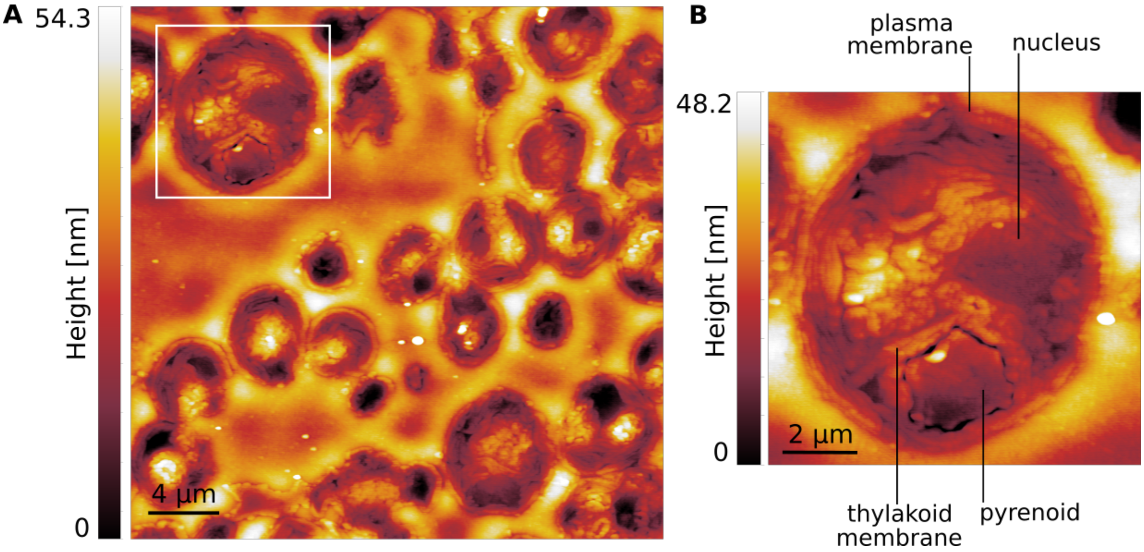

FIGURE 4.25: AFM imaging of *C.reinhardtii* thin sections
**A** Overview AFM image of thin *C. reinhardtii* slices. **B** AFM image of a single cell (zoomed in the region marked in (A)) slice revealing several organelles.

Next, nanoFTIR spectroscopy was performed on the thin section shown in Figure 4.26 a. Eight spectra were measured on the cellular area and one on the surrounding resin (Figure 4.26 b) . All spectra are referenced against bare TS Au substrate. Spectrum #1 was recorded on the pyrenoid and is dominated by peaks at 1655 cm$^{-1}$

and 1541 cm$^{-1}$ assigned to the protein-characteristic molecular vibrations associated with amide I and amide II, respectively. Indeed, previous studies have reported high concentration of proteins contained in the pyrenoid such as RuBisCO entailed in $CO_2$ fixation [214], [215].

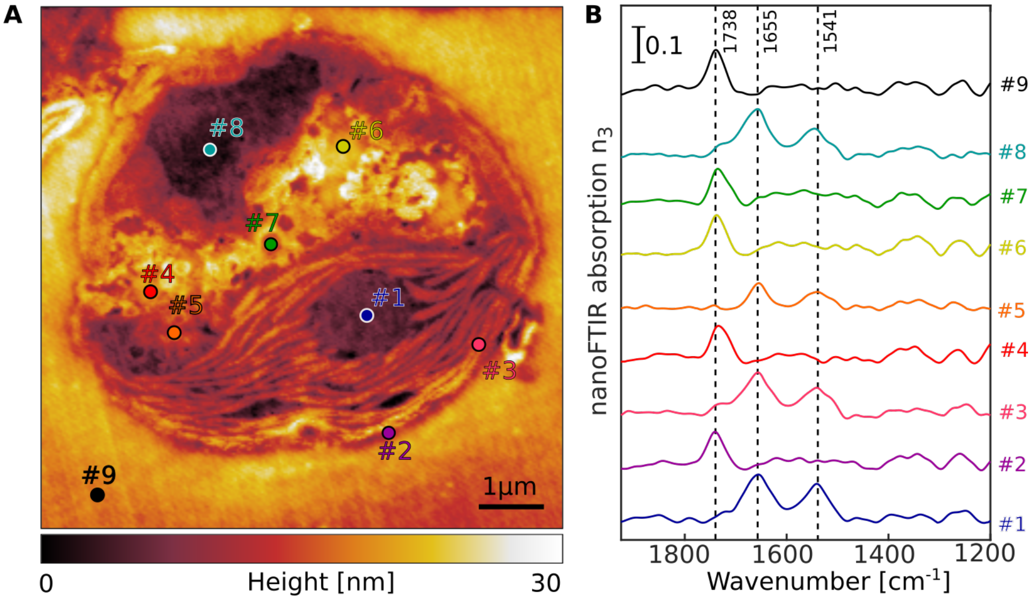

FIGURE 4.26: NanoFTIR spectroscopy of *C.reinhardtii* thin sections **A** AFM topography image of a thin section. **B** Eight nanoFTIR spectra recorded on various spots on the cell area (locations marked on the AFM image) and one measured on the surrounding resin. Figure adapted from [211].

Spectrum #2 was measured on the cellular membrane and shows peak at 1738 cm$^{-1}$. Contribution to this absorption can originate from C=O stretching vibrations in lipids or from succinic anhydride groups in the resin (previously discussed in Chapter 4.6.1 and in spectrum #9). Spectrum #3 probes the nanoFTIR absorption of the thylakoid. Protein-characteristic absorption features are observed at 1655 cm$^{-1}$ and 1541 cm$^{-1}$. The protein content in the thylakoid originates from the protein complexes Photosystem I (PSI) and Photosystem II (PSII), which are responsible for photosynthesis [216]. Chlorophyll, a cofactor in PSI and PSII, could contribute to the absorption in the range 1560-1520 cm$^{-1}$ via C=O and C=N vibrations of chlorin rings [217]. A minute peak is observed at around 1738 cm$^{-1}$ stemming from either C=O stretching from ester groups in chlorophyll or resin. However, previously reported IR spectra of extracted and purified chlorophyll show multiple distinct absorption peaks which were not conclusively observed in the nanoFTIR spectra [218]. The lack of distinct chlorophyll characteristic absorption features could be attributed to dissolving of this pigment in ethanol, used in a dehydration step in the resin-embedding process. During this step, there was a visible loss of green pigment observed. The spectra #4, #5, #6 and #7 were recorded in the inner cytoplasmic area. Interestingly, the spectra #4, #6 and #7 highly resemble the resin spectrum (#9), whereas in #5 mostly absorption from amide I and amide II is observed. The presence of resin in some of the organelles inside the cell hints at resin penetration in regions containing fluids prior to the dehydration step. NanoFTIR spectra of the central area in the nucleus is represented by spectrum #8. The highest intensity peak is observed at 1655 cm$^{-1}$, followed by the peak at 1541 cm$^{-1}$. Proteins located in the nucleus [219] contribute to these absorption features. Additionally, absorption from nucleobases, such as ring modes from purine and pyrimidine contribute to the absorption in this spectral range [220]. Absorption features in the 1400-1300 cm$^{-1}$ range are lower in intensity and result from the overlap of several molecular vibrations, of both cellular and resin origin. $CH_3$ deformation, $CH_2$ bending and C-O bending modes show absorption at around 1390 cm$^{-1}$ stemming from proteins (amide III) and carboxylic groups. Absorption at around 1350 cm$^{-1}$ can be assigned to C-H deformation.

To gain an overview of the absorption distribution throughout the cell area sSNOM imaging was performed. A cell cross-section with diameter of ∼ 7µm (Figure 4.27 a) was selected for imaging at 1655 cm$^{-1}$. The sSNOM amplitude (Figure 4.27 b) shows low reflectivity on the thylakoid membranes, whereas high contrast is observed in the nuclear area, the pyrenoid and a few organelles in the inner cytoplasmic region. The phase image (Figure 4.27 c) shows the strongest absorption on the pyrenoid and the central part of the nucleus. High contrast is also observed on the thylakoid membrane. Several areas in the cytoplasmic region are completely devoid of absorption, indicating that these structures are filled with resin.

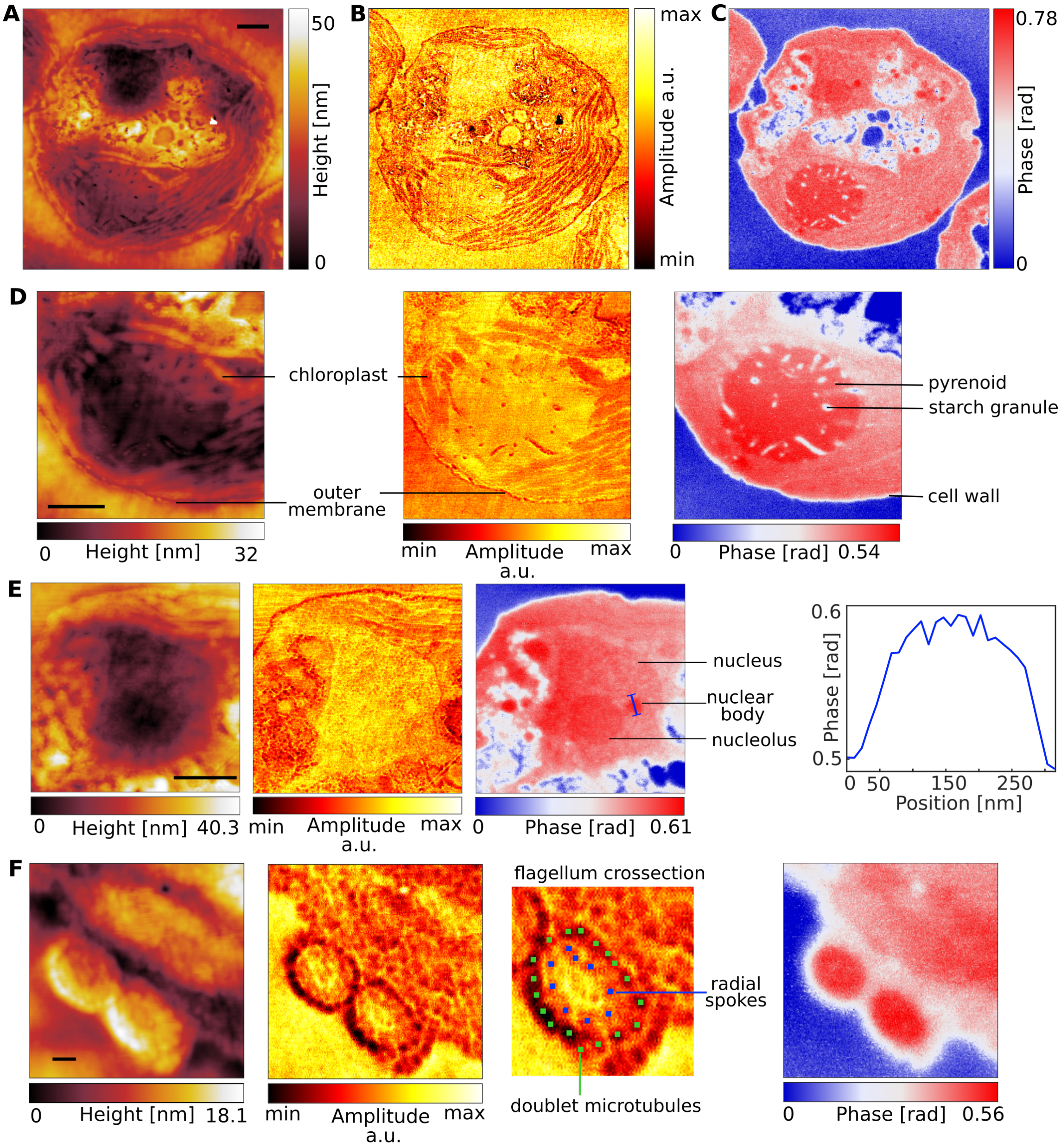

FIGURE 4.27: Subcellular AFM and sSNOM imaging of *C.reinhardtii*
**A** AFM, **B** sSNOM amplitude and **C** sSNOM phase image at 1655 cm$^{-1}$. **D** Zoomed-in AFM topography image of the pyrenoid region (leftmost panel) and corresponding sSNOM amplitude and phase. **E** AFM topography, sSNOM amplitude and phase image covering the nuclear area. Rightmost panel show the phase profile across a nuclear body, labeled in the phase image. **F** AFM topography, sSNOM amplitude and phase image of a flagellum cross-section. The sSNOM amplitude reveals the inner structure of the flagellum, consisting of doublet microtubles, radial spokes and in the central area, the inner sheath (slightly visible in the AFM topography). Scale bars in A-E correspond to 1 µm and in F, to 100 nm. Figure adapted from [211].

No absorption is observed on the surrounding resin. A zoom into the pyrenoid area (Figure 4.27 d) allows for distinguishing starch granules protruding the spherical body of the pyrenoid, especially visible in the phase image. The outer membrane is evident on the AFM image and as a low contrast feature on the amplitude image. In the phase image, an approximately 80 nm thick region of moderate absorption can be observed encapsulating the cell, which was assigned as the cell wall. A closer look in the nuclear area (Figure 4.27 e) reveals several details, visible in the phase image, which couldn't be resolved from the AFM or the amplitude image. The nucleolus, with a regular circular shape with diameter of $\sim$ 500 nm has increased absorption at 1655 cm$^{-1}$ and can therefore be distinguished from the nucleus. Another nuclear body not bound by a membrane could be resolved from the phase image. From its shape and size of $\sim$ 200 nm in diameter (phase profile shown in Figure 4.27 e ,rightmost panel). This nuclear body is most likely a Cajal body [221] characterized by high content of proteins and DNA material. The high spatial resolution of sSNOM allowed for imaging of the inner structure of *C. reinhardtii* flagellum (Figure 4.27 f). The nine pairs of the flagellum's doublet microtubules and the radial spokes are resolved on the sSNOM amplitude image (Figure 4.27 f, middle panels), characterized with a low contrast. The inner sheath is located in the center of the flagellum, and is visible as an area of lower height in the AFM topography image (Figure 4.27 f, leftmost panel). The flagellum area has rather homogeneous high absorption in the center and lower absorption on the outer region, evident from the phase image (rightmost panel).

Based on the nanoFTIR absorption spectra, sSNOM imaging was performed at few additional wavenumbers. The phase at 1738 cm$^{-1}$ (Figure 4.28 a) shows the highest contrast on the resin area and on several locations in the cytoplasmic region, matching well with the nanoFTIR spectra. Absorption at 1540 cm$^{-1}$ (Figure 4.28 b) has high resemblance with the absorption at 1655 cm$^{-1}$ with the highest contrast observed on the pyrenoid and the nuclear bodies, followed by homogeneous contrast in the thylakoid area. To large extent the observed absorption originates from amide

II mode in proteins. Imaging at 1238 cm$^{-1}$ shows overall weak absorption. Nonetheless, the thylakoid membranes are clearly visible. The nucleolus can be distinguished with slightly higher absorption at 1238 cm$^{-1}$ compared to the surrounding nucleus, possibly due to asymmetric stretch of phosphate groups native to DNA. Moderate contrast is observed in the central cytoplasmic area. The phase image at 1155 cm$^{-1}$ shows high absorption on the resin area and several areas in the cytoplasmic area. The cell wall, starch granules and thylakoid membranes with moderate contrast are clearly visualized. Absorption at this wavenumber is due to C-O-C stretch in esters and complex sugar modes [217, 210].

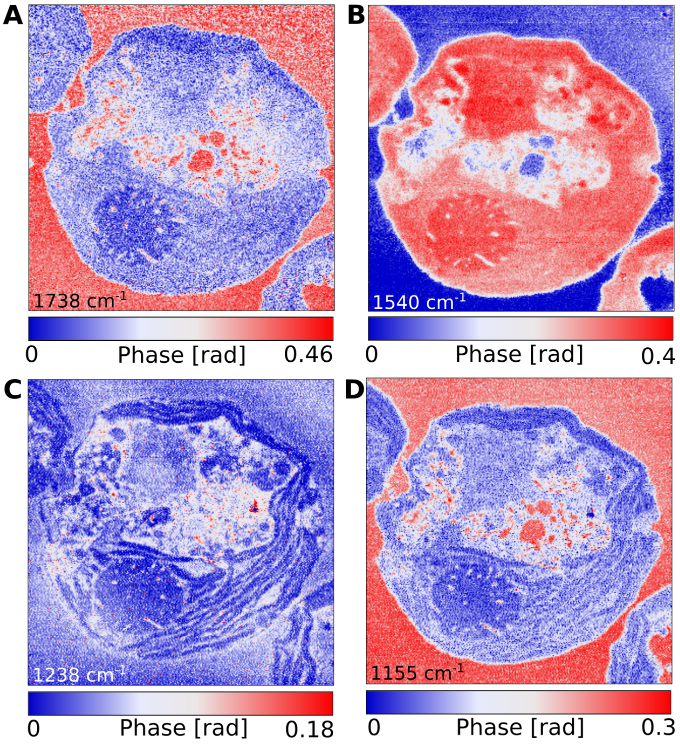

FIGURE 4.28: sSNOM phase imaging of *C.reinhardtii* based on the nanoFTIR absorption bands (Figure 4.26) **A** Phase image of a thin section at 1738 cm$^{-1}$, **B** at 1540 cm$^{-1}$, **C** at 1238 cm$^{-1}$ and **D** at 1155 cm$^{-1}$. Figure adapted from [211].

NanoFTIR was used to characterize the sub-cellular structures chemically by recording absorption spectra with bandwidth of more than 700 cm$^{-1}$ on one single point, while sSNOM imaging provided an overview of the absorption over many pixels at particular wavenumber. Natural extension is to record a full nanoFTIR spectrum on each pixel in an approach known as hyperspectral imaging [222]. A demonstration of this approach is shown in Appendix A.4, where an area of 6.5 µm x 6.5 µm was divided in 20 x 20 pixels, resulting in acquisition of 400 nanoFTIR spectra (Figure A.6). Achieving a lateral resolution of 30 nm would however require at least 50k pixels, which poses practical challenges due to the duration necessary to perform such an experiment.

#### 4.6.2.1 sSNOM tomography

Serial sectioning provided ten consecutive slices used for sSNOM tomography. Utilizing the top-view optics of the commercial sSNOM setup, a distinct cell was chosen. Sections of this same cell were located on each of the ten slices and used to perform sSNOM imaging at 1656 cm$^{-1}$. The local, predominantly protein absorption is represented by the sSNOM phase (Figure 4.29 a). Throughout the set of images gradual increment of the sell size is evident, as well as morphological changes of its organelles, especially noteworthy in the pyrenoid and nuclear area.

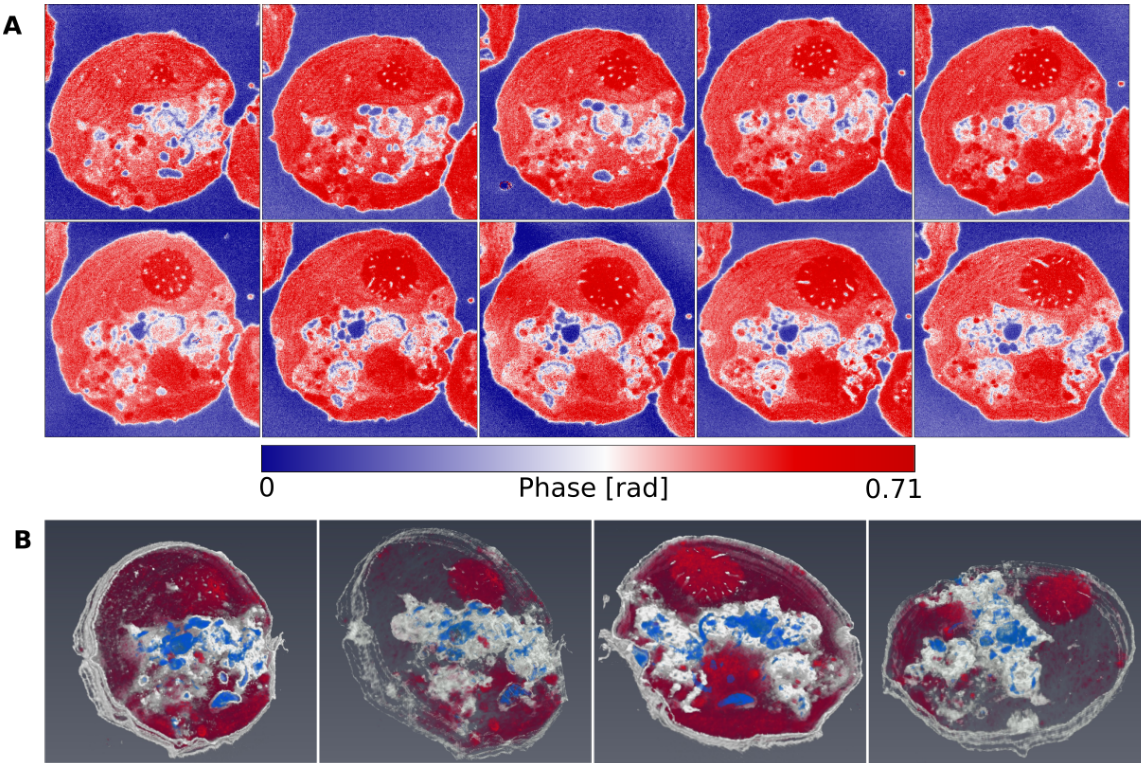

FIGURE 4.29: sSNOM phase tomography
**A** Phase images of ten consecutive slices showing the gradual increase in the overall size as well as the size and shape of the organelles. All were recorded at 1656 cm$^{-1}$. **B** Reconstruction of the individual phase images in (a), top - side view (1st panel), bottom-side view with lower color threshold (2nd panel), top view (3rd panel) and top view with low color threshold (4th panel). Each section is 100 nm thick, thus the sSNOM tomogram corresponds to thickness of 1 µm. Figure adapted from [211].

These images were overlaid and compiled in a 3D sSNOM tomogram (Figure 4.29 b) with depth equivalent to approximately 1 µm ($\sim$ 10% fo the entire *C. reinhardtii* cell). With this approach it was possible to extract information in z-direction from approximately 10 times the typical penetration depth of near-field imaging, while still maintaining lateral resolution of 20 nm. Each voxel corresponds approximately to 20 nm x 20 nm x 1 µm amounting to probed volume of 4x10$^{-19}$l.

## Chapter 5

# Conclusions

Vibrational techniques directly probe molecular vibrations and are thus sensitive to the chemical composition of matter [106]. Due to the intrinsic direct probing ability of IR and Raman spectroscopy, using chemically specific labels to detect molecules is not necessary. Especially noteworthy is that molecular identification in IR spectroscopy is not on the expense of sample damage due to the non destructive nature of IR radiation. The lacking high spatial resolution has been compensated by introducing near-field approaches, that finally led to chemical specificity on a nanometer level [21]. In this work sSNOM imaging and nano-spectroscopy were applied to a series of biological samples with increasing complexity, thus highlighting the versatility and broad applicability of these techniques in biophysics.

The membrane of *Halobacterium*, densely packed with the transmembrane protein *bacteriorhodopsin*, was used as a starting point to evaluate experimental conditions, parameters and limitations in the used sSNOM microscope and nanoFTIR spectrometer. Pioneering work done on this sample [171, 172] allowed a direct comparison and aided data interpretation. In Chapter 4.1, increase of the nanoFTIR absorption with higher demodulation order was observed. Measurements on multiple stacked PM layers showed that the absorption of amide I increases with sample thickness due to the increased number of molecular oscillations. Additionally, the sensitivity to the direction of molecular vibrations, evident by the lack of absorption in the amide II region, was confirmed. Line scan of PM with gradually increasing thickness revealed that the absorption increases up to thickness of approximately

100 nm at n=2. Interestingly, even for stacks amounting to few hundred of nm, the high ordering in the PM layers was preserved, evident from the low absorption of the amide I absorption. Imaging at the absorption maximum of amide I confirmed lateral resolution of sSNOM to be in the order of 30 nm. Imaging of stacked PM layers revealed penetration depth of around 100 nm.

Investigation of potential sSNOM signal enhancement by using disc antenna arrays with resonance in the midIR region was presented in Chapter 4.2. Near-field amplitude images of these plasmonic structures revealed dipole antenna modes. A sSNOM spectrum of PM deposited on the antenna reconstructed from several images showed absorption in the amide I range with contrast increased by factor of 2. To take full advantage of the principle of sSNOM coupled with localized surface plasmons it is necessary to specifically tailor plasmonic structures that could result in stronger coupling and signal enhancement, thus increasing the imaging sensitivity.

Artificially designed peptides and their ability to self assemble under external stimuli were investigated in Chapter 4.3. AFM imaging and nanoFTIR were performed in parallel to access the morphology and secondary structure of the peptides. Sensitivity of IR spectroscopy on the secondary structure was employed to deduce α-helical arrangement in all measured peptides, while their topography showed quite distinct large scale aggregate forms. For instance, high aspect ratio striated rod-like structures with thickness of up to 100 nm and length of several µm were observed for the originally designed (STAP1) at neutral pH, while acidic conditions hindered rod-like structures formation. The observed aggregates had flattened appearance with thickness in the range of 20-70 nm. Mutated version of STAP1, involving replacing leucine residues with the more hydrophobic fluorinated trifluorovaline (STAP2) at pH 7.1, surprisingly showed large area structures with thicknesses of 10-15 nm. Under pH of 3.4, no distinguishable shape of the peptide was observed, but rather ill-formed aggregates implying that acidic environment has counterproductive effect on high order self assembly. The second mutation (STAP3), obtained by substituting leucine with the more hydrophobic isoleucine, formed high aspect ratio rods in neutral conditions, while in acidic environment few nanometer-thin and large area structures were observed.

Large scale morphological changes in soft matter induced by light were observed in polymer brushes loaded with azobenzene-containing surfactant (Chapter 4.4). NanoFTIR spectroscopy proved to be an invaluable tool to investigate changes in the surface pattern and the chemical composition of these complex materials upon formation of surface relief gratings (SRGs). Aided by AFM imaging, it was possible to show that the electrostatic properties of the polymer brush and the surfactant influenced the SRG formation. For instance, the azobenzene surfactant was able to penetrate deep into the weak polyelectrolyte PMAA brush and upon illumination with interference pattern, resulted in polymer chain scission in the areas at high illumination intensity. In turn, PSPMK loaded with azo-nitro surfactant resulted in brushes formed within a limited volume of the polymer, defined by the penetration depth of the surfactant in the strong polyelectrolyte PSPMK. Ultimately, by increasing the illumination energy density, the brush could be rendered photo inactive, evident from the lack of the surfactant marker absorption bands in the nanoFTIR spectrum (Figure 4.16 f-g). Similar outcome was observed by implementing two and three-step illumination (Figure 4.16 f-g).

The concept of exposing given specimen to external stimuli and monitor the induced changes in order to learn about a particular bio-chemical property was employed in studying the cellular metabolic activity, on a single cell level. *E. coli* bacteria were exposed to $^{13}$C labeled glucose. Upon glucose uptake and metabolization, traces of $^{13}$C are present in the cell which manifests in shift of absorption bands of key chemical moieties, such as proteins, due to the mass difference between $^{12}$C and $^{13}$C. In Chapter 4.5 it is demonstrated that nanoFTIR spectroscopy is sensitive to stable isotope probing in *E. coli* by monitoring the amide I and amide II band positions. The cells were supplied with increasing $^{12}$C to $^{13}$C ratio in steps of 10%, spanning from not labeled to fully labeled glucose. PCA analysis of a large data set, including 110 nanoFTIR single cell spectra, showed grouping among measurement points corresponding to the same amount of $^{13}$C. Exposing *E. coli* to limited nutrients induced uncharted $^{13}$C content in single cells. Several nanoFTIR spectra were recorded on the starved cells and their amide I and amide II features were compared with the previously measured spectra. The data variability was visualized using the first two principal components, which covered the largest portion of data variability, obtained by PCA analysis. Thereby, it was possible to estimate the $^{13}$C content and with that the metabolic activity of single cells in nutrient-poor environment.

Whole cell imaging and spectroscopy performed with sSNOM and nanoFTIR does not fully give insight into the internal cellular structure due to penetration depth of the near-fields, typically in the order of 100 nm. Therefore cellular thin sections were used to directly investigate the sub-cellular structure. Thin section of the prokaryote *E. coli* showed no membrane bound organelles or well defined cellular compartments, as presented in Chapter 4.6. In contrast, in the eucaryote alga *C. rheinhardtii* the major cellular parts such as the plasma membrane and cell wall, pyrenoid, nucleus, thylakoid membrane were observed via AFM and sSNOM imaging. NanoFTIR spectra allowed for recording IR spectra on selected areas, thus directly probing the chemical composition of the cells' organelles. Several membrane-less nuclear bodies were resolved only in the sSNOM phase image from the contrast at 1655 cm$^{-1}$ (Figure 4.27 e), thus highlighting a major advantage over AFM topography imaging. Some of the cellular areas were clearer resolved in the sSNOM amplitude image, such as the thylakoid membrane and the inner structure of the flagella. Sequential thin sectioning allowed for sSNOM tomography. This was demonstrated by recording ten serial thin sections at 1656 cm$^{-1}$ each with thickness of 100 nm. Combining the sSNOM phase images results in a 3-dimensional absorption image (Figure 4.29) equivalent to about one tenth of the full volume of *C. rheinhardtii.*

The presented application of near-field based IR microscopy and spectroscopy could be expanded in various directions. For instance, recent advances reported sSNOM imaging of pruple membrane [223] and peptides [224] in liquid environment.

The investigation of the stimuli triggered aggregating peptides can especially benefit from experimentation performed in liquid and thus avoid artifacts due to sample preparation techniques such as spin coating. Another branch emerging from this work is based on the outlined possibility to monitor the metabolic activity on a single cell level, as well as thin section imaging with resolution of 20 nm. By merging both approaches, biochemical processes that are detectable by IR spectroscopy and are spatially localized inside cellular organisms could be directly investigated. These techniques could prove to be useful tolls in the medical field, involving imaging to detect diseased tissue and diagnostics. Hyperspectral imaging, providing a full spectrum on each pixel, coupled with machine learning algorithms [222] could provide unprecedented detail in cell imaging.

# Appendix A

# Supplementary Information

## A.1 ATR spectroscopy of citrate buffer

Stimuli-triggered aggregating peptides (STAP) were adjusted to pH 3.4 using a sodium citrate buffer [225]. In order to trace any contribution of the sodium citrate solution to the absorption features of STAP1, STAP2 and STAP3 nanoFTIR spectra, an ATR spectrum of the buffer was recorded. An absorption peak at 1713 cm$^{-1}$ is observed, originating from carbonyl stretch.

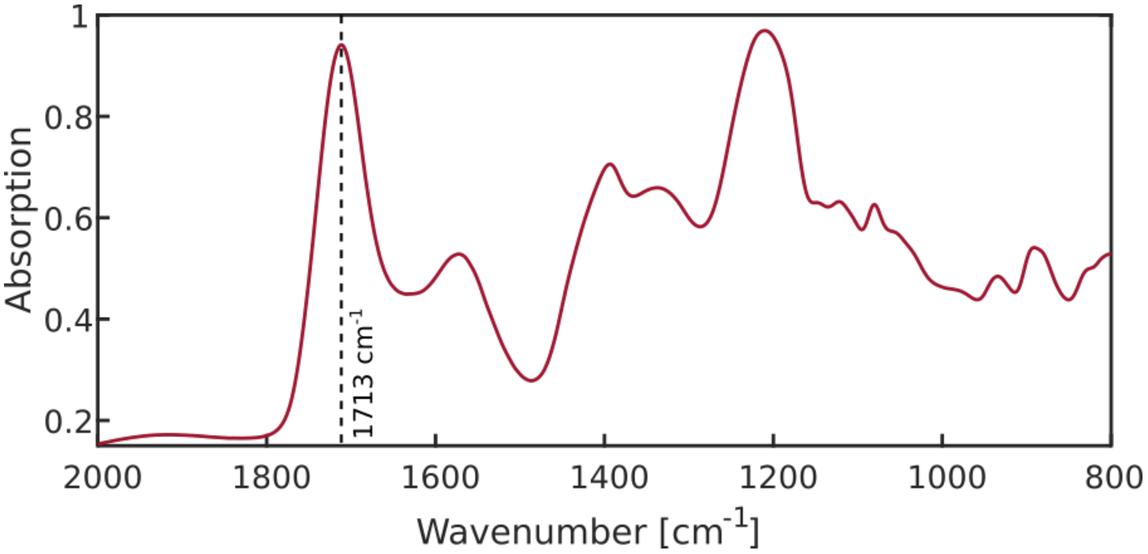

FIGURE A.1: ATR spectrum of sodium citrate buffer at pH 3.4.

## A.2 AFM topography of PMAA-azo complex

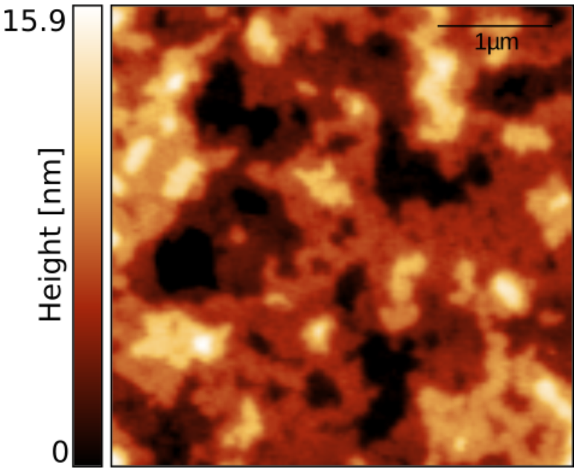

FIGURE A.2: AFM topography of PMAA-azobenzene complex.

PMAA polymer brush was treated with azobenezene-containing surfactant and thereby rendered light sensitive. Before light-illumination with interference pattern, the surface topography was investigated via AFM imaging. The topography on a randomly chosen 4 µm x 4 µm area reveals surface roughness in the order of 15 nm and no evident pattern, which is comparable with the topography of a 5 µx 5 µm area shown in Figure 4.13 a.

## A.3 Principal component analysis

To explore and visualize the correlation among spectra recorded on single cells exposed to the various percentages of isotope labeled glucose principle component analysis (PCA) was performed. PCA involves reducing the number of dimensions in large data sets by inferring new variables from the data set, defined as principle components (PCs), that describe the maximal variation among the data entries [206, 226]. A number of data entries, or measurements $n$ with $p$ number of variables define a $n \times p$ matrix $\mathbf{X}$. New variables are defined by the linear combinations of the matrix $\mathbf{X}$ given by $\mathbf{A} = \mathbf{Xa} = a_1 x_1 + a_2 + x_2 + ... + a_p x_p$, with the largest variance, where $a_1, ...a_p$ are constants. Maximizing the variance given in terms of the vector $\mathbf{a}$, its transpose $\mathbf{a}'$ and the covariance matrix $\mathbf{S}$ as $var(\mathbf{A}) = var(\mathbf{Xa}) = \mathbf{a}'\mathbf{Sa}$ [227] yields the equation $\mathbf{Sa} = \lambda\mathbf{a}$ [228], where $\lambda$ is Lagrange multiplier. Additionally, $\mathbf{a}$ represents the eigenvector and $\lambda$ the eigenvalue of the covariance matrix $\mathbf{S}$. The principal components are defined as $\mathbf{X}\mathbf{a}_k = \sum_{j=1}^{p} a_{jk}\mathbf{x}_j$. The output of PCA analysis is often visualized by a PC scores plot representing the values of the linear combinatoins $\mathbf{X}\mathbf{a}_k$ and PC loadings which contain the values of the eigenvectors $\mathbf{a}_k$.

### A.3.1 Single cell spectra used for PCA analysis

Ten spectra from each of the $^{13}$C/$^{12}$C labeled glucose ratios were used to demonstrate the ability of nano-spectroscopy to differentiate the isotope content.

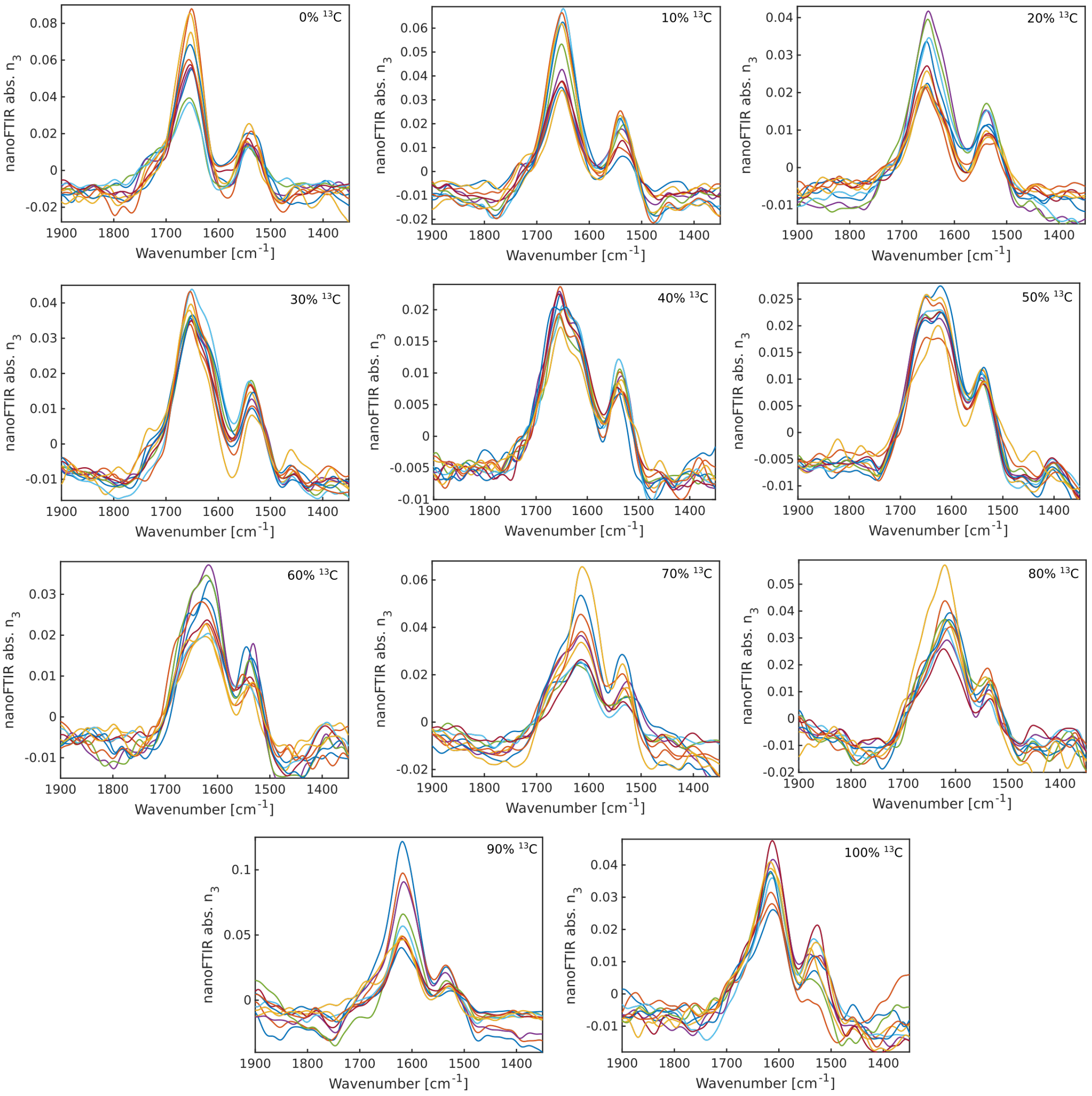

FIGURE A.3: nanoFTIR spectra of single cells used for PCA analysis

A total of 110 nanoFTIR spectra, each recorded on a single cell, are shown in Figure A.3. PCA analysis was carried out with a built-in function in Matlab R2016b using single value decomposition (SVD) algorithm. The data set was centered and each spectrum was vector normalized. The normalized spectra are shown in Figure A.4.

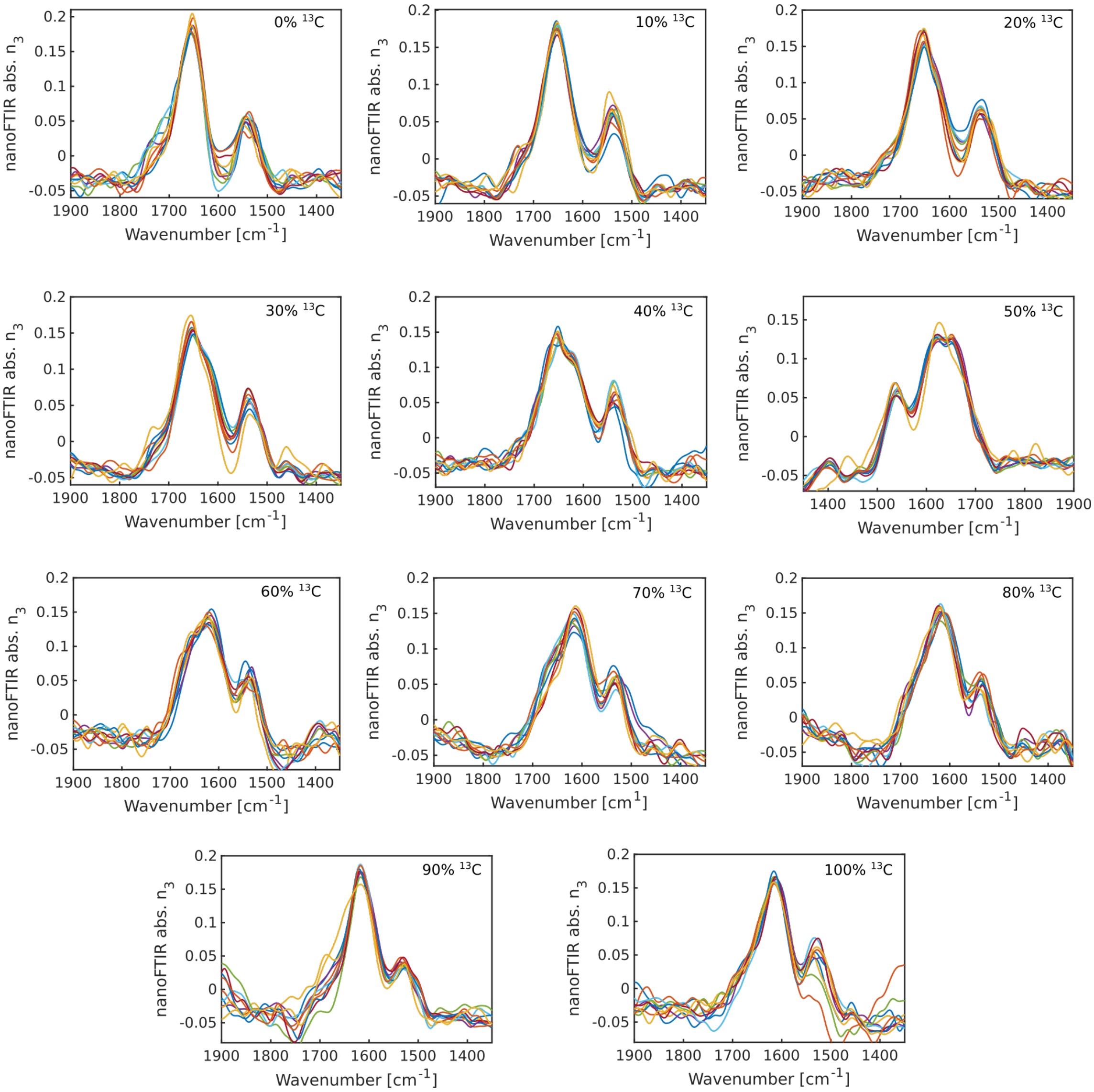

Figure A.4: Normalized nanoFTIR spectra of single cells used for PCA analysis

Loading plots of first and second principle component for this data set are shown in Figure A.5 a,b. The variance in percentage for the first 6 PCs is shown in Figure

SI.5, revealing the highest variance for PC1 of 84.81 % followed by PC2 covering 4.654 %.

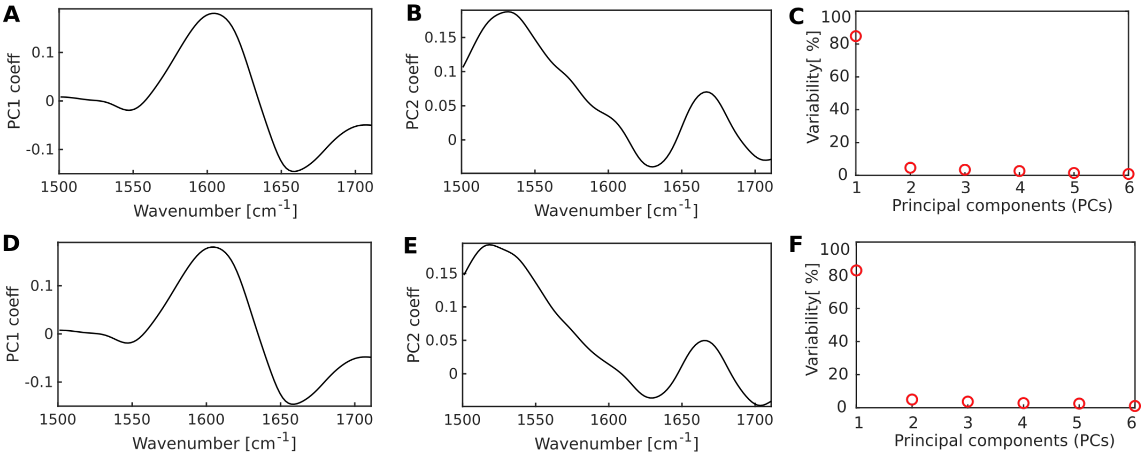

FIGURE A.5: Loading plots
**A** Loading plot visualizing the variation of the first principal component with respect to the wavenumber, corresponding to the data set of 110 cells shown in Figure A.4. **B** Loading plot of the second principal component. **C** Variability in percent of the first six principal components. **D** and **E** loading plots of PC1 and PC2, respectively, of the data set with additional seven spectra of *E. coli* exposed to limited nutrients. **F** Variability of the first six components of this extended data set.

Similarly, the loading plots of the first two PCs and the variance of the first six PCs for the data set including the additional seven spectra with unknown isotope content are shown in Figure A.5 d-f.

## A.4 Hyperspectral Imaging

In addition to recording a sSNOM image at given wavenumber or recording a nanoFTIR spectrum at given location on the sample, it is possible to record a nanoFTIR spectrum on each pixel, an approach known as hyperspectral imaging [222]. In the following, application of this approach to *C. reinhardtii* thin sections is demonstrated. A cell slice with diameter of approximately 6 µm, as evident from the AFM topography image (Figure A.6 a) was used. In order to reduce sample drift effects, be able to maintain the signal level by re.adjusting, the data recording was performed in four stages by splitting the area of interest in four parts, each corresponding to 3.25 x 3.25 µm. NanoFTIR spectra were recorded on 10 x 10 pixels on each quadrant, amounting to total of 100 spectra per quadrant (Figure A6.5 b). On each pixel, five co-additions were measured. Figure Figure A.6 c shows the nanoFTIR phase at selected wavenumbers for the whole image consisting of 400 pixels. The phase was referenced against a spectrum measured on a cell and resin free Au area.

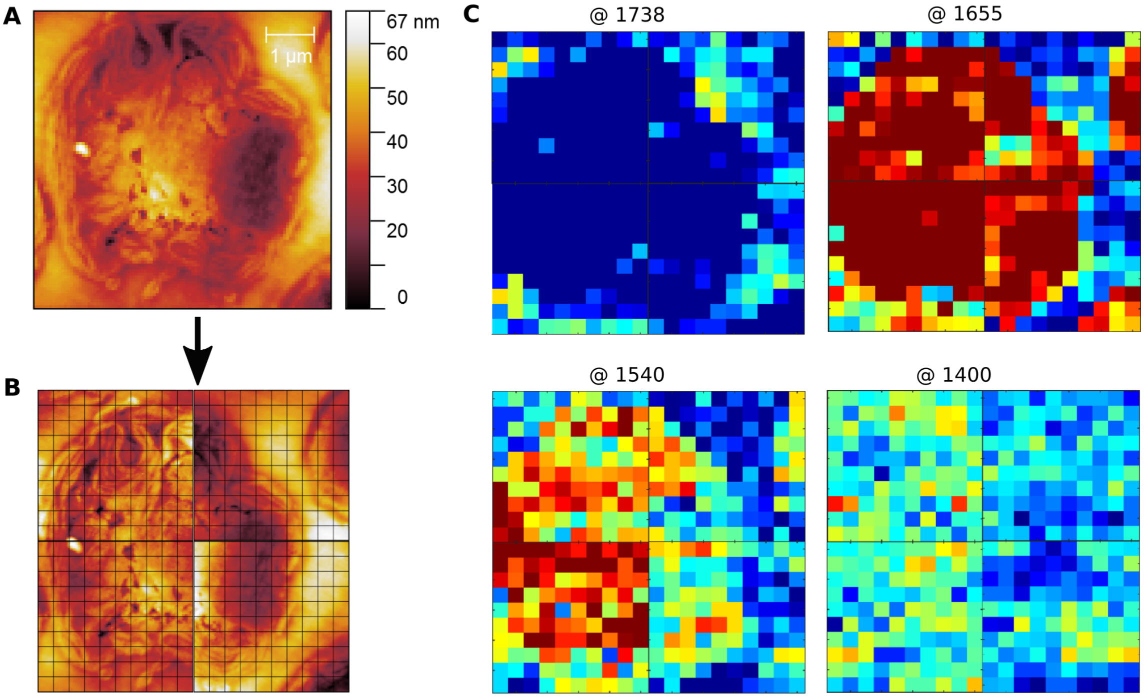

Figure A.6: Hyperspectral imaging
**A** AFM image of a *C. reinhardtii* and **B** the image divided in four quadrants. Each quadrant is sub-divided in 10 x 10 pixels. A full nanoFTIR spectrum was recorded on each pixel. **C** Exemplary images at four wavenumbers obtained from the hyperspectral data set.

The image at 1738 cm$^{-1}$ shows negative contrast on the cellular area and higher contrast on the surrounding resin area due to absorption of C=O vibrations of succinic anhydride. The near-field phase at 1655 cm$^{-1}$ is characterized by strong absorption across the whole cell area, with few pixels in the central part with lower absorption. At 1540 cm$^{-1}$ the absorption features resemble the previous image at 1655 cm$^{-1}$, however with overall weaker absorption. As discussed in Chapter 4.6, absorption in this spectral range is typical for amide I and amide II in proteins. At

1400 cm$^{-1}$, there are no discernible absorption patterns. Finer details of the subcellular structure can not be distinguished due to the low number of pixels. Sampling with resolution in the order of 30 nm, i.e pixel size of at least 30 nm wold require approximately 50 000 pixels. Practical challenges due to lengthy measurements such as sample drift, tip contamination and maintaining good signal-to-noise ratio prevent from performing hyperspectral imaging on such µm-large areas.

# Bibliography

1. Hooke, R. *Micrographia: or some physiological descriptions of minute bodies made by magnifying glasses, with observations and inquiries thereupon* (Courier Corporation, 2003).
2. Croft, W. J. *Under the microscope: a brief history of microscopy* (World Scientific, 2006).
3. Abbe, E. Beiträge zur Theorie des Mikroskops und der mikroskopischen Wahrnehmung. *Archiv für mikroskopische Anatomie* **9,** 413–468 (1873).
4. Airy, G. B. On the diffraction of an object-glass with circular aperture. *Transactions of the Cambridge Philosophical Society* **5,** 283 (1835).
5. Knoll, M. & Ruska, E. Das elektronenmikroskop. *Zeitschrift für physik* **78,** 318–339 (1932).
6. Broglie, L. d. XXXV. A tentative theory of light quanta. *The London, Edinburgh, and Dublin Philosophical Magazine and Journal of Science* **47,** 446–458 (1924).
7. Yip, K. M., Fischer, N., Paknia, E., Chari, A. & Stark, H. Atomic-resolution protein structure determination by cryo-EM. *Nature* **587,** 157–161 (2020).
8. Hell, S. W. *et al.* The 2015 super-resolution microscopy roadmap. *Journal of Physics D: Applied Physics* **48,** 443001 (2015).
9. Hell, S. W. & Wichmann, J. Breaking the diffraction resolution limit by stimulated emission: stimulated-emission-depletion fluorescence microscopy. *Optics letters* **19,** 780–782 (1994).

10. Müller, T., Schumann, C. & Kraegeloh, A. STED microscopy and its applications: new insights into cellular processes on the nanoscale. *ChemPhysChem* **13,** 1986–2000 (2012).

11. Rittweger, E., Han, K. Y., Irvine, S. E., Eggeling, C. & Hell, S. W. STED microscopy reveals crystal colour centres with nanometric resolution. *Nature Photonics* **3,** 144–147 (2009).

12. Barth, A. Infrared spectroscopy of proteins. *Biochimica et Biophysica Acta (BBA)-Bioenergetics* **1767,** 1073–1101 (2007).

13. Cheng, J. X. & Xie, X. S. Vibrational spectroscopic imaging of living systems: An emerging platform for biology and medicine. *Science* **350** (2015).

14. Harris, D. C. & Bertolucci, M. D. *Symmetry and spectroscopy: an introduction to vibrational and electronic spectroscopy* (Courier Corporation, 1989).

15. Kim, H., Bryant, G. W. & Stranick, S. J. Superresolution four-wave mixing microscopy. *Optics express* **20,** 6042–6051 (2012).

16. Stuart, B. H. *Infrared spectroscopy: fundamentals and applications* (John Wiley & Sons, 2004).

17. Faist, J. *et al.* Quantum cascade laser. *Science* **264,** 553–556 (1994).

18. Pilling, M. J. *et al.* High-throughput quantum cascade laser (QCL) spectral histopathology: a practical approach towards clinical translation. *Faraday discussions* **187,** 135–154 (2016).

19. Kuepper, C. *et al.* Quantum cascade laser-based infrared microscopy for label-free and automated cancer classification in tissue sections. *Scientific reports* **8,** 1–10 (2018).

20. Goertzen, N. *et al.* Quantum Cascade Laser–Based Infrared Imaging as a Label-Free and Automated Approach to Determine Mutations in Lung Adenocarcinoma. *The American Journal of Pathology* (2021).

21. Zayats, A. V. & Richards, D. *Nano-optics and near-field optical microscopy* (Artech House, 2009).
22. Pohl, D. W. & Courjon, D. *Near field optics* (Springer Science & Business Media, 1993).
23. Pohl, D. W. The Invention of an Optical Antenna—A Personal Reminiscence. *Applied Sciences* **8** (2018).
24. Neacsu, C. C., Steudle, G. A. & Raschke, M. B. Plasmonic light scattering from nanoscopic metal tips. *Applied Physics B* **80,** 295–300 (2005).
25. Atkin, J. M., Berweger, S., Jones, A. C. & Raschke, M. B. Nano-optical imaging and spectroscopy of order, phases, and domains in complex solids. *Advances in Physics* **61,** 745–842 (2012).
26. Stöckle, R. M., Suh, Y. D., Deckert, V. & Zenobi, R. Nanoscale chemical analysis by tip-enhanced Raman spectroscopy. *Chemical Physics Letters* **318,** 131–136 (2000).
27. Anderson, M. S. Locally enhanced Raman spectroscopy with an atomic force microscope. *Applied Physics Letters* **76,** 3130–3132 (2000).
28. Pettinger, B., Picardi, G., Schuster, R. & Ertl, G. Surface enhanced Raman spectroscopy: towards single molecule spectroscopy. *Electrochemistry* **68,** 942–949 (2000).
29. Hayazawa, N., Inouye, Y., Sekkat, Z. & Kawata, S. Metallized tip amplification of near-field Raman scattering. *Optics Communications* **183,** 333–336 (2000).
30. Lee, J., Crampton, K. T., Tallarida, N. & Apkarian, V. A. Visualizing vibrational normal modes of a single molecule with atomically confined light. *Nature* **568,** 78–82 (2019).
31. Zhang, R. *et al.* Chemical mapping of a single molecule by plasmon-enhanced Raman scattering. *Nature* **498,** 82–86 (2013).

32. Kurouski, D., Dazzi, A., Zenobi, R. & Centrone, A. Infrared and Raman chemical imaging and spectroscopy at the nanoscale. *Chemical Society Reviews* **49,** 3315–3347 (2020).
33. Pohl, D. W., Denk, W. & Lanz, M. Optical stethoscopy: Image recording with resolution $\lambda/20$. *Applied physics letters* **44,** 651–653 (1984).
34. Lewis, A., Isaacson, M., Harootunian, A. & Muray, A. Development of a 500 Å spatial resolution light microscope: I. light is efficiently transmitted through $\lambda/16$ diameter apertures. *Ultramicroscopy* **13,** 227–231 (1984).
35. Zenhausern, F., O'boyle, M. P. & Wickramasinghe, H. K. Apertureless near-field optical microscope. *Applied Physics Letters* **65,** 1623–1625 (1994).
36. Zenhausern, F., Martin, Y. & Wickramasinghe, H. K. Scanning interferometric apertureless microscopy: optical imaging at 10 angstrom resolution. *Science* **269,** 1083–1085 (1995).
37. Knoll, B. & Keilmann, F. Near-field probing of vibrational absorption for chemical microscopy. *Nature* **399,** 134–137 (1999).
38. Hillenbrand, R. & Keilmann, F. Complex optical constants on a subwavelength scale. *Physical Review Letters* **85,** 3029 (2000).
39. Mastel, S. *et al.* Understanding the image contrast of material boundaries in IR nanoscopy reaching 5 nm spatial resolution. *ACS Photonics* **5,** 3372–3378 (2018).
40. Amarie, S., Ganz, T. & Keilmann, F. Mid-infrared near-field spectroscopy. *Optics Express* **17** (2009).
41. Keilmann, F. & Amarie, S. Mid-infrared Frequency Comb Spanning an Octave Based on an Er Fiber Laser and Difference-Frequency Generation. *J Infrared Milli Teraherz Waves* **33,** 479–484 (2012).

42. Bechtel, H. A., Muller, E. A., Olmon, R. L., Martin, M. C. & Raschke, M. B. Ultrabroadband infrared nanospectroscopic imaging. *Proceedings of the National Academy of Sciences* **111,** 7191–7196 (2014).
43. Hermann, P. *et al.* Characterization of semiconductor materials using synchrotron radiation-based near-field infrared microscopy and nano-FTIR spectroscopy. *Optics express* **22,** 17948–17958 (2014).
44. Nan, C., Yue, W., Tao, L. & Yang, X. Fourier transform infrared nanospectroscopy: Mechanism and applications. *Applied Spectroscopy Reviews* **56,** 531–552 (2021).
45. Binnig, G. & Rohrer, H. Scanning tunneling microscopy. *Surface Science* **126,** 236 –244 (1983).
46. Binnig, G., Rohrer, H., Gerber, C. & Weibel, E. 7× 7 reconstruction on Si (111) resolved in real space. *Physical review letters* **50,** 120 (1983).
47. Binning, G. *pat.* (1986).
48. Binnig, G., Quate, C. F. & Gerber, C. Atomic Force Microscope. *Phys. Rev. Lett.* **56,** 930–933 (9 1986).
49. Giessibl, F. J. Atomic resolution of the silicon (111)-(7x7) surface by atomic force microscopy. *Science* **267,** 68–71 (1995).
50. Alessandrini, A. & Facci, P. AFM: a versatile tool in biophysics. *Measurement science and technology* **16,** R65 (2005).
51. Garcıa, R. & Perez, R. Dynamic atomic force microscopy methods. *Surface science reports* **47,** 197–301 (2002).
52. Lennard-Jones, J. E. Cohesion. *Proceedings of the Physical Society* **43,** 461–482 (1931).
53. Giessibl, F. J. Advances in atomic force microscopy. *Reviews of modern physics* **75,** 949 (2003).

54. Rotsch, C. & Radmacher, M. Mapping local electrostatic forces with the atomic force microscope. *Langmuir* **13,** 2825–2832 (1997).
55. Lantz, M. A. *et al.* Quantitative measurement of short-range chemical bonding forces. *Science* **291,** 2580–2583 (2001).
56. Saenz, J. J. *et al.* Observation of magnetic forces by the atomic force microscope. *Journal of applied physics* **62,** 4293–4295 (1987).
57. O'shea, S. J. & Welland, M. E. Atomic force microscopy at solid- liquid interfaces. *Langmuir* **14,** 4186–4197 (1998).
58. Giessibl, F. J. AFM's path to atomic resolution. *Materials Today* **8,** 32–41 (2005).
59. Jalili, N. & Laxminarayana, K. A review of atomic force microscopy imaging systems: application to molecular metrology and biological sciences. *Mechatronics* **14,** 907–945 (2004).
60. Zhong, Q., Inniss, D., Kjoller, K. & Elings, V. B. Fractured polymer/silica fiber surface studied by tapping mode atomic force microscopy. *Surface Science Letters* **290,** L688–L692 (1993).
61. Martin, Y., Williams, C. C. & Wickramasinghe, H. K. Atomic force microscope–force mapping and profiling on a sub 100-Å scale. *Journal of applied Physics* **61,** 4723–4729 (1987).
62. Drake, B. *et al.* Imaging crystals, polymers, and processes in water with the atomic force microscope. *Science* **243,** 1586–1589 (1989).
63. Shibata, M., Yamashita, H., Uchihashi, T., Kandori, H. & Ando, T. High-speed atomic force microscopy shows dynamic molecular processes in photoactivated bacteriorhodopsin. *Nature Nanotechnology* **5,** 208–212 (3 2010).
64. Kodera, N., Yamamoto, D., Ishikawa, R. & Ando, T. Video imaging of walking myosin V by high-speed atomic force microscopy. *Nature* **468,** 72–76 (7320 2010).

65. Sweers, K., van der Werf, K., Bennink, M. & Subramaniam, V. Nanomechanical properties of α-synuclein amyloid fibrils: a comparative study by nanoindentation, harmonic force microscopy, and Peakforce QNM. *Nanoscale Research Letters* **6** (1 2011).

66. Harke, B., Chacko, J. V., Haschke, H., Canale, C. & Diaspro, A. A novel nanoscopic tool by combining AFM with STED microscopy. *Optical Nanoscopy* **1** (2012).

67. Synge, E. H. A suggested method for extending microscopic resolution into the ultra-microscopic region. *The London, Edinburgh, and Dublin Philosophical Magazine and Journal of Science* **6,** 356–362 (1928).

68. Ash, E. A. & Nicholls, G. Super-resolution aperture scanning microscope. *Nature* **237,** 510–512 (1972).

69. Pohl, D. W. Optical near-field scanning microscope. *US Patent EP0112401A1* (1982).

70. Maxwell, J. C. II. A dynamical theory of the electromagnetic field. *Proceedings of the Royal Society of London,* 531–536 (1864).

71. Kawata, S., Ohtsu, M. & Irie, M. *Near-field optics and surface plasmon polaritons* (Springer Science & Business Media, 2001).

72. Hayazawa, N., Inouye, Y. & Kawata, S. Evanescent field excitation and measurement of dye fluorescence in a metallic probe near-field scanning optical microscope. *Journal of microscopy* **194,** 472–476 (1999).

73. Inouye, Y. & Kawata, S. Near-field scanning optical microscope with a metallic probe tip. *Optics letters* **19,** 159–161 (1994).

74. Deng, F., Du, C. & Luo, X. Characteristic analysis of evanescent wave moire fringes. *JOSA B* **25,** 443–447 (2008).

75. Dürig, U., Pohl, D. W. & Rohner, F. Near-field optical-scanning microscopy. *Journal of applied physics* **59,** 3318–3327 (1986).

76. Betzig, E., Trautman, J. K., Harris, T. D., Weiner, J. S. & Kostelak, R. L. Breaking the diffraction barrier: optical microscopy on a nanometric scale. *Science* **251,** 1468–1470 (1991).
77. Heinzelmann, H. & Pohl, D. W. Scanning near-field optical microscopy. *Applied Physics A* **59,** 89–101 (1994).
78. Hecht, B. *et al.* Scanning near-field optical microscopy with aperture probes: Fundamentals and applications. *The Journal of Chemical Physics* **112,** 7761–7774 (2000).
79. Bethe, H. A. Theory of diffraction by small holes. *Physical review* **66,** 163 (1944).
80. Novotny, L., Pohl, D. W. & Hecht, B. Scanning near-field optical probe with ultrasmall spot size. *Optics letters* **20,** 970–972 (1995).
81. Wickramasinghe, H. K. & Williams, C. Apertureless near field optical microscope. *US Patent US4947034A* (1989).
82. Kawata, S. & Inouye, Y. Scanning probe optical microscopy using a metallic probe tip. *Ultramicroscopy* **57,** 313–317 (1995).
83. Knoll, B. & Keilmann, F. Enhanced dielectric contrast in scattering-type scanning near-field optical microscopy. *Optics communications* **182,** 321–328 (2000).
84. Griffiths, D. J. *Introduction to electrodynamics* (American Association of Physics Teachers, 2005).
85. Keilmann, F. & Hillenbrand, R. Near-field microscopy by elastic light scattering from a tip. *Philosophical Transactions of the Royal Society of London. Series A: Mathematical, Physical and Engineering Sciences* **362,** 787–805 (2004).

86. Taubner, T., Hillenbrand, R. & Keilmann, F. Nanoscale polymer recognition by spectral signature in scattering infrared near-field microscopy. *Applied Physics Letters* **85,** 5064–5066 (2004).
87. Guo, X., Bertling, K. & Rakić, A. D. Optical constants from scattering-type scanning near-field optical microscope. *Applied Physics Letters* **118,** 041103 (2021).
88. Landau, L. D. *et al. Electrodynamics of continuous media* (elsevier, 2013).
89. Govyadinov, A. A., Amenabar, I., Huth, F., Carney, P. S. & Hillenbrand, R. Quantitative measurement of local infrared absorption and dielectric function with tip-enhanced near-field microscopy. *The journal of physical chemistry letters* **4,** 1526–1531 (2013).
90. Cvitkovic, A., Ocelic, N. & Hillenbrand, R. Analytical model for quantitative prediction of material contrasts in scattering-type near-field optical microscopy. *Optics express* **15,** 8550–8565 (2007).
91. Hauer, B., Engelhardt, A. P. & Taubner, T. Quasi-analytical model for scattering infrared near-field microscopy on layered systems. *Optics express* **20,** 13173–13188 (2012).
92. Raschke, M. B. & Lienau, C. Apertureless near-field optical microscopy: Tip–sample coupling in elastic light scattering. *Applied Physics Letters* **83,** 5089–5091 (2003).
93. Renger, J., Grafström, S., Eng, L. M. & Hillenbrand, R. Resonant light scattering by near-field-induced phonon polaritons. *Physical Review B* **71,** 075410 (2005).
94. Aizpurua, J., Taubner, T., de Abajo, F. J. G., Brehm, M. & Hillenbrand, R. Substrate-enhanced infrared near-field spectroscopy. *Optics Express* **16,** 1529–1545 (2008).

95. Mastel, S., Govyadinov, A. A., de Oliveira, T. V. A. G., Amenabar, I. & Hillenbrand, R. Nanoscale-resolved chemical identification of thin organic films using infrared near-field spectroscopy and standard Fourier transform infrared references. *Applied Physics Letters* **106,** 023113 (2015).

96. Mester, L., Govyadinov, A. A., Chen, S., Goikoetxea, M. & Hillenbrand, R. Subsurface chemical nanoidentification by nano-FTIR spectroscopy. *Nature communications* **11,** 1–10 (2020).

97. Wurtz, G., Bachelot, R. & Royer, P. A reflection-mode apertureless scanning near-field optical microscope developed from a commercial scanning probe microscope. *Review of Scientific Instruments* **69,** 1735–1743 (1998).

98. Wurtz, G., Bachelot, R. & Royer, P. Imaging a GaAlAs laser diode in operation using apertureless scanning near-field optical microscopy. *The European Physical Journal-Applied Physics* **5,** 269–275 (1999).

99. Ocelic, N., Huber, A. & Hillenbrand, R. Pseudoheterodyne detection for background-free near-field spectroscopy. *Applied Physics Letters* **89,** 101124 (2006).

100. Hillenbrand, R., Taubner, T. & Keilmann, F. Phonon-enhanced light–matter interaction at the nanometre scale. *Nature* **418,** 159–162 (2002).

101. Moreno, C., Alda, J., Kinzel, E. & Boreman, G. Phase imaging and detection in pseudo-heterodyne scattering scanning near-field optical microscopy measurements. *Applied optics* **56,** 1037–1045 (2017).

102. Keilmann, F. FIR microscopy. *Infrared Physics & Technology* **36,** 217–224 (1995).

103. Hunsche, S., Koch, M., Brener, I. & Nuss, M. C. THz near-field imaging. *Optics communications* **150,** 22–26 (1998).

104. Huber, A. J., Keilmann, F., Wittborn, J., Aizpurua, J. & Hillenbrand, R. Terahertz near-field nanoscopy of mobile carriers in single semiconductor nanodevices. *Nano letters* **8,** 3766–3770 (2008).
105. Cooley, J. W. & Turkey, J. W. The re-discovery of the fast Fourier transform algorithm. *Mathematics of Computation* **19** (1965).
106. Chalmers, J. M. & Griffiths, P. R. *Handbook of Vibrational Spectroscopy* (John Wiley & Sons Ltd., 2002).
107. Siebert, F. & Hildebrandt, P. *Vibrational spectroscopy in life science* (John Wiley & Sons, 2008).
108. Wilson, E. B., Decius, J. C. & Cross, P. C. *Molecular vibrations: the theory of infrared and Raman vibrational spectra* (Courier Corporation, 1980).
109. Atkins, P., De Paula, J. & Friedman, R. *Quanta, matter, and change: a molecular approach to physical chemistry* (Oxford University Press, USA, 2009).
110. Heller, E. J. The semiclassical way to molecular spectroscopy. *Accounts of Chemical Research* **14,** 368–375 (1981).
111. Dahl, J. P. & Springborg, M. The Morse oscillator in position space, momentum space, and phase space. *The Journal of chemical physics* **88,** 4535–4547 (1988).
112. Sathyanarayana, D. N. *Vibrational Spectroscopy: Theory and Applications* ISBN: 9788122415179 (New Age International (P) Limited, 2015).
113. Skoog, D. A., Holler, F. J. & Crouch, S. R. *Principles of instrumental analysis* (Cengage learning, 2017).
114. Griffiths, P. R. Fourier transform infrared spectrometry. *Science* **222,** 297–302 (1983).
115. Griffiths, P. R., De Haseth, J. A. & Winefordner, J. D. *Fourier Transform Infrared Spectrometry* ISBN: 9780470106297 (Wiley, 2007).
116. Harrick, N. J. *Internal reflection spectroscopy* (1967).

117. Milosevic, M. On the nature of the evanescent wave. *Applied spectroscopy* **67,** 126–131 (2013).

118. Huth, F. *et al.* Nano-FTIR Absorption Spectroscopy of Molecular Fingerprints at 20 nm Spatial Resolution. *Nano Letters* **12,** 3973–3978 (2012).

119. Arkin, I. T. Isotope-edited IR spectroscopy for the study of membrane proteins. *Current opinion in chemical biology* **10,** 394–401 (2006).

120. Lagunov, O., Drenchev, N., Chakarova, K., Panayotov, D. & Hadjiivanov, K. Isotopic Labelling in Vibrational Spectroscopy: A Technique to Decipher the Structure of Surface Species. *Topics in Catalysis* **60,** 1486–1495 (2017).

121. Hartstein, A., Kirtley, J. R. & Tsang, J. C. Enhancement of the infrared absorption from molecular monolayers with thin metal overlayers. *Physical Review Letters* **45,** 201 (1980).

122. Osawa, M., Ataka, K., Yoshii, K. & Nishikawa, Y. Surface-enhanced infrared spectroscopy: the origin of the absorption enhancement and band selection rule in the infrared spectra of molecules adsorbed on fine metal particles. *Applied spectroscopy* **47,** 1497–1502 (1993).

123. Schlücker, S. Surface-Enhanced raman spectroscopy: Concepts and chemical applications. *Angewandte Chemie International Edition* **53,** 4756–4795 (2014).

124. Knoll, W. Interfaces and thin films as seen by bound electromagnetic waves. *Annual review of physical chemistry* **49,** 569–638 (1998).

125. Fischer, U. C. & Pohl, D. W. Observation of single-particle plasmons by near-field optical microscopy. *Physical review letters* **62,** 458 (1989).

126. Novotny, L., Hecht, B. & Pohl, D. W. Interference of locally excited surface plasmons. *Journal of Applied Physics* **81,** 1798–1806 (1997).

127. Neubrech, F. *et al.* Resonant plasmonic and vibrational coupling in a tailored nanoantenna for infrared detection. *Physical review letters* **101,** 157403 (2008).

128. García-Etxarri, A., Romero, I., de Abajo, F. J. G., Hillenbrand, R. & Aizpurua, J. Influence of the tip in near-field imaging of nanoparticle plasmonic modes: Weak and strong coupling regimes. *Physical Review B* **79,** 125439 (2009).

129. Schnell, M. *et al.* Controlling the near-field oscillations of loaded plasmonic nanoantennas. *Nature Photonics* **3,** 287–291 (2009).

130. Kelly, K. L., Coronado, E., Zhao, L. L & Schatz, G. C. *The optical properties of metal nanoparticles: the influence of size, shape, and dielectric environment* 2003.

131. Mie, G. Beiträge zur Optik trüber Medien, speziell kolloidaler Metallösungen. *Annalen der physik* **330,** 377–445 (1908).

132. Yee, K. Numerical solution of initial boundary value problems involving Maxwell's equations in isotropic media. *IEEE Transactions on antennas and propagation* **14,** 302–307 (1966).

133. Kawata, S., Ohtsu, M. & Irie, M. *Near-field optics and surface plasmon polaritons* 49–69 (Springer Science & Business Media, 2001).

134. Neuman, T. *et al.* Mapping the near fields of plasmonic nanoantennas by scattering-type scanning near-field optical microscopy. *Laser & Photonics Reviews* **9,** 637–649 (2015).

135. Hoffmann, J. M. *et al.* Low-cost infrared resonant structures for surface-enhanced infrared absorption spectroscopy in the fingerprint region from 3 to 13 $\mu$m. *The Journal of Physical Chemistry C* **117,** 11311–11316 (2013).

136. Hoffmann, J. M., Janssen, H., Chigrin, D. N. & Taubner, T. Enhanced infrared spectroscopy using small-gap antennas prepared with two-step evaporation nanosphere lithography. *Optics express* **22,** 14425–14432 (2014).

137. Jain, P. K., Huang, W. & El-Sayed, M. A. On the universal scaling behavior of the distance decay of plasmon coupling in metal nanoparticle pairs: a plasmon ruler equation. *Nano Letters* **7,** 2080–2088 (2007).

138. Jain, P. K., Huang, X., El-Sayed, I. H. & El-Sayed, M. A. Noble metals on the nanoscale: optical and photothermal properties and some applications in imaging, sensing, biology, and medicine. *Accounts of chemical research* **41,** 1578–1586 (2008).

139. Alonso-Gonzalez, P. *et al.* Real-space mapping of Fano interference in plasmonic metamolecules. *Nano letters* **11,** 3922–3926 (2011).

140. Luk'yanchuk, B. *et al.* The Fano resonance in plasmonic nanostructures and metamaterials. *Nature materials* **9,** 707–715 (2010).

141. Hoffmann, J. M., Hauer, B. & Taubner, T. Antenna-enhanced infrared near-field nanospectroscopy of a polymer. *Applied Physics Letters* **101,** 193105 (2012).

142. O'Callahan, B. T., Hentschel, M., Raschke, M. B., El-Khoury, P. Z. & Lea, S. A. Ultrasensitive Tip-and Antenna-Enhanced Infrared Nanoscopy of Protein Complexes. *The Journal of Physical Chemistry C* **123,** 17505–17509 (2019).

143. Adato, R., Aksu, S. & Altug, H. Engineering mid-infrared nanoantennas for surface enhanced infrared absorption spectroscopy. *Materials today* **18,** 436–446 (2015).

144. Mueller, N. S. *et al.* Surface-Enhanced Raman Scattering and Surface-Enhanced Infrared Absorption by Plasmon Polaritons in Three-Dimensional Nanoparticle Supercrystals. *ACS nano* **15,** 5523–5533 (2021).

145. Nečas, D. & Klapetek, P. Gwyddion: an open-source software for SPM data analysis. *Open Physics* **10,** 181–188 (2012).

146. Pfitzner, E. *Surface and Tip-Enhanced Infrared Spectroscopy in Life Science: Approaching the Single-Molecule Limit* PhD thesis (Freie Universität Berlin, Department of Physics, 2018).

147. Mihaljevic, J., Hafner, C. & Meixner, A. J. Simulation of a metallic SNOM tip illuminated by a parabolic mirror. *Optics express* **21,** 25926–25943 (2013).

148. Gambetta, A., Ramponi, R. & Marangoni, M. Mid-infrared optical combs from a compact amplified Er-doped fiber oscillator. *Optics letters* **33,** 2671–2673 (2008).

149. Smith, B. C. *Fundamentals of Fourier transformed infrared spectroscopy* (CRC Press, Taylor & Francis Group, 2011).

150. Hegner, M., Wagner, P. & Semenza, G. Ultralarge atomically flat template-stripped Au surfaces for scanning probe microscopy. *Surface Science* **291,** 39–46 (1-2 1993).

151. Wägli, P., Homsy, A. & de Rooij, N. F. Norland optical adhesive (NOA81) microchannels with adjustable wetting behavior and high chemical resistance against a range of mid-infrared-transparent organic solvents. *Sensors and Actuators B: Chemical* **156,** 994–1001 (2011).

152. Pfitzner, E., Seki, H., Schlesinger, R., Ataka, K. & Heberle, J. Disc antenna enhanced infrared spectroscopy: From self-assembled monolayers to membrane proteins. *ACS sensors* **3,** 984–991 (2018).

153. Osterhelt, D. & Stoeckenius, W. Rhodopsin-like Protein from the Purple Membrane of *Halobacterium halobium. Nature New Biology* **233** (10 1971).

154. Osterhelt, D. & Stoeckenius, W. Functions of a New Photoreceptor Membrane. *Proceedings of the National Academy of Sciences of the United States of America* **70,** 2853–2857 (10 1973).

155. Henderson, R., Baldwin, J. M. & Ceska, T. A. Model for the Structure of Bacteriorhodopsin Based on High-resolution Electron Cryo-microscopy. *Journal of Molecular Biology* **213,** 899–929 (1990).

156. Lozier, R., Bogomolni, R. & Stoeckenius, W. Bacteriorhodopsin: A light-driven proton pump in *halobacterium halobium. Biophysical Journal* **15** (1975).

157. Lanyi, J. K. Bacteriorhodopsin. *Annu. Rev. Physiol.* **66,** 665–688 (2004).

158. Müller, D & Engel, A. Atomic force microscopy and spectroscopy of native membrane proteins. *Nature Protocols,* 2191–2197 (2007).

159. Zhang, S., Holmes, T., Lockshin, C. & Rich, A. Spontaneous assembly of a self-complementary oligopeptide to form a stable macroscopic membrane. *Proceedings of the National Academy of Sciences of the United States of America,* 3334–3338 (1993).

160. Falenski, J. A., M, G. U. I. & Koksch, B. Multiple glycosylation of de novo designed $\alpha$ -helical coiled coil peptides. *Bioorganic & Medicinal Chemistry,* 3703–3706 (2010).

161. Zacco, E. *et al.* A Self-Assembling Peptide Scaffold for the Multivalent Presentation of Antigens. *Biomacromolecules,* 2188–2197 (2015).

162. Fernandes, A. R. d. L. *Investigation of supramolecular assemblies based on de novo coiled coil peptidic scaffolds* PhD thesis (Freie Universität Berlin, Department of Biology, Chemistry and Pharmacy, 2019).

163. Milner, S. T. Polymer Brushes. *Science* **251,** 905–914 (1991).

164. Ballauff, M. & Borisov, O. Polyelectrolyte Brushes. *Current Opinion in Colloid and Interface Science* **11,** 316–323 (2007).

165. Chen, W., Cordero, R., Tran, H. & Ober, C. K. 50th Anniversary Perspective: Polymer Brushes: Novel Surfaces for Future Materials. *Macromolecules* **50,** 4089–4113 (2017).

166. Prucker, O. & Rühe, J. Polymer Layers through Self-Assembled Monolayers of Initiators. *Langmuir* **14,** 6893–6898 (1998).

167. Kobayashi, M., Terada, M. & Takahara, A. Reversible adhesive-free nanoscale adhesion utilizing oppositely charged polyelectrolyte brushes. *Soft Matter* **7,** 5717–5722 (2011).

168. Kopyshev, A., Lomadze, N., Feldmann, D., Genzer, J. & Santer, S. Making polymer brush photosensitive with azobenzene containing surfactants. *Polymer* **79,** 65–72 (2015).

169. Kopyshev, A. *et al.* Light-Induced Structuring of Photosensitive Polymer Brushes. *Applied Polymer Materials* **1,** 3017–3026 (2019).

170. Schuh, C., Lomadze, N., Rühe, J., Kopyshev, A. & Santer, S. Photomechanical Degrafting of Azo-Functionalized Poly(methacrylic acid) (PMAA) Brushes. *The Journal of Physical Chemistry B* **115,** 10431–10438 (2011).

171. Amenabar, I. *et al.* Structural analysis and mapping of individual protein complexes by infrared nanospectroscopy. *Nature communications* **4,** 1–9 (2013).

172. Berweger, S. *et al.* Nano-chemical infrared imaging of membrane proteins in lipid bilayers. *Journal of the American Chemical Society* **135,** 18292–18295 (2013).

173. Singh, B. R. *Infrared analysis of peptides and proteins* (ACS Publications, 2000).

174. Müller, D. J., Schabert, F. A., Büldt, G & Engel, A. Imaging purple membranes in aqueous solutions at sub-nanometer resolution by atomic force microscopy. *Biophysical journal* **68,** 1681–1686 (1995).

175. Krutokhvostov, R. *et al.* Enhanced resolution in subsurface near-field optical microscopy. *Optics express* **20,** 593–600 (2012).

176. Govyadinov, A. A. *et al.* Recovery of permittivity and depth from near-field data as a step toward infrared nanotomography. *Acs Nano* **8,** 6911–6921 (2014).

177. Rothschild, K. J. & Clark, N. A. Polarized infrared spectroscopy of oriented purple membrane. *Biophysical journal* **25,** 473–487 (1979).

178. Lewin, M. *et al.* Imaging of phase change materials below a capping layer using correlative infrared near-field microscopy and electron microscopy. *Applied Physics Letters* **107,** 151902 (2015).

179. Jung, L. *et al.* Exploring the detection limits of infrared near-field microscopy regarding small buried structures and pushing them by exploiting superlens-related effects. *Optics express* **24,** 4431–4441 (2016).

180. Ho, K. *et al.* Nanoscale subsurface morphologies in block copolymer thin films revealed by combined near-field infrared microscopy and mechanical mapping. *ACS Applied Polymer Materials* **1,** 933–938 (2019).

181. Govyadinov, A. A. *et al.* Recovery of permittivity and depth from near-field data as a step toward infrared nanotomography. *Acs Nano* **8,** 6911–6921 (2014).

182. Muller, E. A. *et al.* Nanoimaging and control of molecular vibrations through electromagnetically induced scattering reaching the strong coupling regime. *ACS photonics* **5,** 3594–3600 (2018).

183. Barth, A. & Zscherp, C. What vibrations tell about proteins. *Quarterly reviews of biophysics* **35,** 369–430 (2002).

184. Nevskaya, N. A. & Chirgadze, Y. N. Infrared spectra and resonance interactions of amide-I and II vibrations of $\alpha$-helix. *Biopolymers: Original Research on Biomolecules* **15,** 637–648 (1976).

185. Ruggeri, F. S. *et al.* Infrared nanospectroscopy characterization of oligomeric and fibrillar aggregates during amyloid formation. *Nature communications* **6,** 1–9 (2015).

186. Gribbon, C. *et al.* MagicWand: A single, designed peptide that assembles to stable, ordered $\alpha$-helical fibers. *Biochemistry* **47,** 10365–10371 (2008).

187. Zhou, N. E., Kay, C. M. & Hodges, R. S. Synthetic model proteins. Positional effects of interchain hydrophobic interactions on stability of two-stranded alpha-helical coiled-coils. *Journal of Biological Chemistry* **267,** 2664–2670 (1992).

188. Lin, Y. C., Repollet-Pedrosa, M. H., Ferrie, J. J., Petersson, E. J. & Fakhraai, Z. Potential artifacts in sample preparation methods used for imaging amyloid oligomers and protofibrils due to surface-mediated fibril formation. *The Journal of Physical Chemistry B* **121,** 2534–2542 (2017).

189. Tajiri, T., Morita, S. & Ozaki, Y. Hydration mechanism on a poly (methacrylic acid) film studied by in situ attenuated total reflection infrared spectroscopy. *Polymer* **50,** 5765–5770 (2009).

190. Buffeteau, T., Lagugné Labarthet, F., Pézolet, M. & Sourisseau, C. Photoinduced orientation of azobenzene chromophores in amorphous polymers as studied by real-time visible and FTIR spectroscopies. *Macromolecules* **31,** 7312–7320 (1998).

191. Lomadze, N., Kopyshev, A., Rühe, J. & Santer, S. Light-Induced Chain Scission in Photosensitive Polymer Brushes. *Macromolecules* **44,** 7372–7377 (2011).

192. Milekhin, A. *et al.* Infrared spectroscopy of bonded silicon wafers. *Semiconductors* **40,** 1304–1313 (2006).

193. Kopani, M, Mikula, M, Takahashi, M, Rusnák, J & Pinčík, E. FT IR spectroscopy of silicon oxide layers prepared with perchloric acid. *Applied surface science* **269,** 106–109 (2013).

194. Santer, S. Remote control of soft nano-objects by light using azobenzene containing surfactants. *Journal of Physics D: Applied Physics* **51,** 013002 (2017).

195. Rau, H. *Photoisomerization of azobenzenes* 119–141 (CRC Press: Boca Raton, FL, 1990).

196. Toshchevikov, V., Saphiannikova, M. & Heinrich, G. Light-induced deformation of azobenzene elastomers: a regular cubic network model. *The Journal of Physical Chemistry B* **116,** 913–924 (2012).

197. Toshchevikov, V., Ilnytskyi, J. & Saphiannikova, M. Photoisomerization kinetics and mechanical stress in azobenzene-containing materials. *The journal of physical chemistry letters* **8,** 1094–1098 (2017).

198. Lomadze, N., Kopyshev, A., Ru'he, J. & Santer, S. Light-induced chain scission in photosensitive polymer brushes. *Macromolecules* **44,** 7372–7377 (2011).

199. Israels, R., Leermakers, F. A. M. & Fleer, G. J. On the theory of grafted weak polyacids. *Macromolecules* **27,** 3087–3093 (1994).

200. Yang, Z., Tarabara, V. V. & Bruening, M. L. Adsorption of anionic or cationic surfactants in polyanionic brushes and its effect on brush swelling and fouling resistance during emulsion filtration. *Langmuir* **31,** 11790–11799 (2015).

201. Zhulina, E. B., Birshtein, T. M. & Borisov, O. V. Theory of ionizable polymer brushes. *Macromolecules* **28,** 1491–1499 (1995).

202. Muhamadali, H., Chisanga, M., Subaihi, A. & Goodacre, R. Combining Raman and FT-IR spectroscopy with quantitative isotopic labeling for differentiation of E. coli cells at community and single cell levels. *Analytical chemistry* **87,** 4578–4586 (2015).

203. Lima, C., Muhamadali, H., Xu, Y., Kansiz, M. & Goodacre, R. Imaging isotopically labeled bacteria at the single-cell level using high-resolution optical infrared photothermal spectroscopy. *Analytical chemistry* **93,** 3082–3088 (2021).

204. Muhamadali, H., Chisanga, M., Subaihi, A. & Goodacre, R. Combining Raman and FT-IR spectroscopy with quantitative isotopic labeling for differentiation of E. coli cells at community and single cell levels. *Analytical chemistry* **87,** 4578–4586 (2015).

205. Lima, C., Muhamadali, H., Xu, Y., Kansiz, M. & Goodacre, R. Imaging isotopically labeled bacteria at the single-cell level using high-resolution optical infrared photothermal spectroscopy. *Analytical chemistry* **93,** 3082–3088 (2021).

206. Pearson, K. LIII. On lines and planes of closest fit to systems of points in space. *The London, Edinburgh, and Dublin philosophical magazine and journal of science* **2,** 559–572 (1901).

207. Bolshakova, A. V. *et al.* Comparative studies of bacteria with an atomic force microscopy operating in different modes. *Ultramicroscopy* **86,** 121–128 (2001).

208. Braga, P. C. & Ricci, D. Atomic force microscopy: application to investigation of Escherichia coli morphology before and after exposure to cefodizime. *Antimicrobial agents and chemotherapy* **42,** 18–22 (1998).

209. Huang, K. C., Mukhopadhyay, R., Wen, B., Gitai, Z. & Wingreen, N. S. Cell shape and cell-wall organization in Gram-negative bacteria. *Proceedings of the National Academy of Sciences* **105,** 19282–19287 (2008).

210. Naumann, D., Barnickel, G., Bradaczek, H., Labischinski, H. & Giesbrecht, P. Infrared spectroscopy, a tool for probing bacterial peptidoglycan: potentialities of infrared spectroscopy for cell wall analytical studies and rejection of models based on crystalline chitin. *European journal of biochemistry* **125,** 505–515 (1982).

211. Kanevche, K. *et al.* Infrared Nanoscopy and Tomography of Intracellular Structures. *Preprint DOI:10.21203/rs.3.rs-753486/v1* (2021).

212. Wiercigroch, E. *et al.* Raman and infrared spectroscopy of carbohydrates: A review. *Spectrochimica Acta Part A: Molecular and Biomolecular Spectroscopy* **185,** 317–335 (2017).

213. Salomé, P. A. & Merchant, S. S. A series of fortunate events: Introducing Chlamydomonas as a reference organism. *The Plant Cell* **31,** 1682–1707 (2019).

214. Kuchitsu, K., Tsuzuki, M. & Miyachi, S. Characterization of the pyrenoid isolated from unicellular green alga Chlamydomonas reinhardtii: Particulate form of RuBisCO protein. *Protoplasma* **144,** 17–24 (1988).

215. Kuchitsu, K., Tsuzuki, M. & Miyachi, S. Polypeptide composition and enzyme activities of the pyrenoid and its regulation by $CO_2$ concentration in unicellular green algae. *Canadian Journal of Botany* **69,** 1062–1069 (1991).

216. Grossman, A. R. Chlamydomonas reinhardtii and photosynthesis: genetics to genomics. *Current opinion in plant biology* **3,** 132–137 (2000).

217. Weigl, J. W. & Livingston, R. Infrared Spectra of Chlorophyll and Related Compounds1. *Journal of the American Chemical Society* **75,** 2173–2176 (1953).

218. Katz, J. J., Dougherty, R. C. & Boucher, L. J. in *The chlorophylls* 185–251 (Elsevier, 1966).

219. Winck, F. V., Riaño-Pachón, D. M., Sommer, F., Rupprecht, J. & Mueller-Roeber, B. The nuclear proteome of the green alga Chlamydomonas reinhardtii. *Proteomics* **12,** 95–100 (2012).

220. Han, Y., Han, L., Yao, Y., Li, Y. & Liu, X. Key factors in FTIR spectroscopic analysis of DNA: the sampling technique, pretreatment temperature and sample concentration. *Analytical Methods* **10,** 2436–2443 (2018).

221. Cuevas-Velazquez, C. L. & Dinneny, J. R. Organization out of disorder: liquid–liquid phase separation in plants. *Current opinion in plant biology* **45,** 68–74 (2018).

222. Amenabar, I. *et al.* Hyperspectral infrared nanoimaging of organic samples based on Fourier transform infrared nanospectroscopy. *Nature communications* **8,** 1–10 (2017).

223. Pfitzner, E. & Heberle, J. Infrared scattering-type scanning near-field optical microscopy of biomembranes in water. *The Journal of Physical Chemistry Letters* **11,** 8183–8188 (2020).

224. O'Callahan, B. T. *et al.* In liquid infrared scattering scanning near-field optical microscopy for chemical and biological nanoimaging. *Nano letters* **20,** 4497–4504 (2020).

225. Dawson, R. M. C., Elliott, D. C., Elliott, W. H. & Jones, K. M. *Data for biochemical research* (Clarendon Press, 2002).

226. Hotelling, H. Analysis of a complex of statistical variables into principal components. *Journal of educational psychology* **24,** 417 (1933).

227. Riley, K. F., Hobson, M. P. & Bence, S. J. *Mathematical methods for physics and engineering* 1999.

228. Jolliffe, I. T. & Cadima, J. Principal component analysis: a review and recent developments. *Philosophical Transactions of the Royal Society A: Mathematical, Physical and Engineering Sciences* **374,** 20150202 (2016).

# ACKNOWLEDGMENTS

First and foremost, I would like to thank Prof. Dr. Joachim Heberle for the opportunity to be part of his research group. I am especially thankful for his invaluable advise, guidance and support throughout the endeavor to complete my doctorate, as well as for providing an atmosphere for freedom of thought and expression. I would further like to thank the whole AG Heberle and AG Schlesinger for many unforgettable moments, contributing to the overall great experience I had during my PhD time. Special thanks goes to Dr. Emanuel Pfitzner for great collaboration, advice, constructive discussions and incredible support in the lab. I would like to express my appreciation for the support by AG Schlesinger and their generously providing samples. I am also very thankful for the fruitful collaboration with Prof. Svetlana Santer and the co-workers Dr. Nino Lomadze and Dr. Alexey Kopyshev from Universität Potsdam; Prof. Beate Koksch and Dr. Ana Rita de Lima Fernandez from the Chemistry department at Freie Universität Berlin. Many thanks go to Dr. Andreas Elsaessar and David Burr from the Physics Department at Freie Universität for exceptionally close collaboration, as well as to Dr. Dennis Nürnberg for kindly providing algae samples. I thank Dr. Emanuel Pfitzner, David Burr, Dr. Yusuke Sakiyama, Dr. Jacek Kozuch and Jan Skowranek for proofreading parts of this thesis. Additionally, I appreciate the support provided by Dr. Jacek Kozuch in translating the Abstract to German.

Finally, I would like to wholeheartedly thank Jan Skowranek for always supporting me, giving me motivation to pursue my goals and for his unconditional love and care.

# DECLARATION OF AUTHORSHIP

Name: Kanevche

First name: Katerina

I declare to the Freie Universität Berlin that I have completed the submitted dissertation independently and without the use of sources and aids other than those indicated. The present thesis is free of plagiarism. I have marked as such all statements that are taken literally or in content from other writings. This dissertation has not been submitted in the same or similar form in any previous doctoral procedure. I agree to have my thesis examined by a plagiarism examination software

Date:

Signature: